sustainability

MDPI

Review

A Comprehensive Review on Green Synthesis and Characterization of Plant-Based Nanoparticles for Water Treatment Applications: Adsorption and Photodegradation of Organic and Inorganic Pollutants

Marouane El Alouani [1,2,*], Hamid Saufi [1], Badr Aouan [1], Rajaa Bassam [3], Mariem Ben Tourtit [1], Amal Bassam [3], Wafaa Ahmina [1], Younes Rachdi [1,3], Said Belaaouad [3] and Saliha Alehyen [1]

[1] Laboratory of Physics and Chemistry of Inorganic and Organic Materials, LPCMIO, Materials Science Research Center, Ecole Normale Supérieure, Mohammed V University of Rabat, Rabat 10000, Morocco; saufihamid@yahoo.fr (H.S.); badr.aouan@gmail.com (B.A.); mariem.bentourtit@um5r.ac.ma (M.B.T.); wafaa.ahmina@gmail.com (W.A.); rachdi.smc@gmail.com (Y.R.); alehyensali@yahoo.fr (S.A.)
[2] Little Prince High School-Saint Joseph Foundation, Istanbul 34887, Turkey
[3] Laboratory of Physical Chemistry of Materials LCPM, Faculty of Sciences Ben M'Sik, Hassan II University of Casablanca, Bd Cdt Driss El Harti, P.O. Box 7955, Mohammedia 28800, Morocco; bassam.rajaa@gmail.com (R.B.); sbelaaouad@yahoo.fr (S.B.)
* Correspondence: ma.elalouani@gmail.com; Tel.: +90-506-166-85-57

Abstract

Growing concerns about environmental pollution and the sustainability of conventional nanomaterial synthesis have accelerated interest in plant-based routes for nanoparticle production. This review provides an in-depth analysis of more than 290 peer-reviewed research and review articles published between 2010 and 2025, extracted from the Web of Science and Scopus databases, on the green synthesis of metallic and metal oxide nanoparticles using plant extracts, with particular emphasis on their characterization and application in water treatment. Plant-derived phytochemicals serve as natural reducing and stabilizing agents, enabling nanoparticle formation without hazardous reagents. Key physicochemical characterization techniques, including UV–Visible spectroscopy, X-ray diffraction, Fourier Transform Infrared spectroscopy, scanning and transmission electron microscopy, and energy-dispersive X-ray analysis, are evaluated for their roles in confirming nanoparticle structure, morphology, surface chemistry, and optical behavior. The review focuses on water purification applications, highlighting adsorption and photocatalytic degradation as the most extensively investigated removal pathways. Particular attention is given to widely studied material classes such as silver, zinc oxide, titanium dioxide, and iron-based nanoparticles, which demonstrate effective removal of heavy metals, synthetic dyes, pesticides, and pharmaceutical residues. Current limitations related to synthesis reproducibility, mechanistic understanding, stability, and scalability are critically discussed. The review concludes by identifying priority research directions, including standardized synthesis protocols, deeper chemical analysis of plant extracts, and the integration of green nanoparticles into immobilized and membrane-based systems to advance their practical implementation in sustainable water treatment technologies.

Keywords: nanoparticles; plant extracts; salt solutions; characterization; water treatment

Check for updates

Academic Editor: Andrea G. Capodaglio

Received: 22 January 2026
Revised: 24 February 2026
Accepted: 24 February 2026
Published: 11 March 2026

Copyright: © 2026 by the authors. Licensee MDPI, Basel, Switzerland. This article is an open access article distributed under the terms and conditions of the Creative Commons Attribution (CC BY) license.

1. Introduction

Nanotechnology, or nanoscience, is a field of research that enables the development of materials and/or groups of natural origin with dimensions between 1 and 100 nanometers (nm), known as nanomaterials or nanoparticles. Prof. Dr. Norio Taniguchi coined the term "nanotechnology" in 1974 [1]. Nanoparticles have a wide range of properties, including chemical, biological, optical, mechanical, and thermal, which means they have many potential applications and have attracted considerable interest across fields such as catalysis, optics, energy science, biomedicine, medicine, electronics, and the environment [2,3]. The chemical and physical techniques used to synthesize nanoparticles are based on chemical elements such as platinum, gold, and others [4]. These materials do not represent an ecological or cost-effective process.

Nanomaterials have attracted considerable attention as photocatalysts due to their reduced dimensions, high surface-to-volume ratio, and tunable electronic structures, which enable efficient light absorption and accelerated redox reactions for environmental remediation. Semiconductor nanostructures in particular have been widely investigated for wastewater treatment, where they promote the degradation of organic pollutants by enhancing charge separation and reactive species generation [5]. Recent studies have demonstrated that engineered composite systems can significantly improve photocatalytic performance. For instance, the enhanced piezo-photocatalytic sewage treatment efficiency of TPU/g-C_3N_4 composite nanofiber films has been demonstrated through their improved mechanical stability and light-driven catalytic activity [6]. Similarly, advanced heterostructured catalysts such as $ZnFe_2O_4$/BiOBr/MXene S-scheme composites demonstrate enhanced photocatalytic performance due to efficient interfacial charge transfer and increased redox potential, thereby facilitating the wastewater purification efficiently [7]. Although these advanced synthetic photocatalysts provide remarkable performance, their preparation often involves complex fabrication steps and non-renewable components, which has stimulated growing interest in developing sustainable alternatives. To address the harmful effects of chemical-based nanomaterials on the ecosystem, several researchers have proposed a "green and ecological" synthesis strategy and technique called nanobiotechnology to develop nanomaterials based on biological agents such as plants, *algae*, *fungi*, *yeast*, and *bacteria* [8–12]. At the same time, ecological research on plant species such as *Caragana korshinskii* highlights the intrinsic ability of plants to modify mineral composition and soil characteristics in natural environments. Taken together, these results emphasize the promise of a plant-based approach, reinforcing the growing interest in environmentally synthesized nanomaterials as cost-effective, sustainable, and eco-friendly alternatives for wastewater remediation [13].

Nanobiotechnology, or green nanotechnology, is a field that uses plant-based materials to minimize and reduce the adverse effects of other chemical methods for manufacturing and applying chemical-based nanomaterials [14]. Many studies have revealed that sustainable synthesis techniques can allow the highly efficient generation of nanoparticles with the required properties. Green synthesis using plant parts, such as resins, flowers, or fruits, has proven to be extremely promising, as plant extracts can reduce metal ions to form nanoparticles, which can be analyzed and confirmed using various spectroscopic methods, such as XRD, UV–Vis, FTIR, SEM, and EDS [15,16]. Several factors, including plant and salt concentrations, temperature, and pH, influence the synthesis of nanoparticles from plant extracts. Salt concentration is critical to the nanoparticles' size and production speed. pH plays a crucial role in controlling the morphology, structure, and shape of the nanoparticles obtained. Temperature plays a very efficient role in accelerating nanoparticle synthesis [17]. Numerous studies have shown that green synthesis methods effectively produce nanoparticles with desirable properties [18–20]. Microbial-mediated synthesis has

shown great promise because microorganisms can reduce metal ions and form nanoparticles. Furthermore, fungal- and algal-mediated synthesis has emerged as a viable alternative, offering sustainable and scalable methods for nanoparticle production [21]. Nanomaterials derived from plant extracts and saline solutions have attracted researchers' attention due to their remarkable properties, particularly thermal stability, wastewater treatment performance via adsorption, excellent conductivity, and notable anti-inflammatory, antibacterial, antioxidant, antifungal, and antiviral activities [22,23].

Green-synthesized nanoparticles have attracted growing attention for water purification due to their high surface area, abundant reactive sites, and ability to interact with various pollutants [24]. Their thermal stability, surface reactivity, and catalytic behavior make them suitable for removing heavy metals, dyes, pharmaceuticals, and other organic contaminants through adsorption and photocatalytic degradation [25]. In recent years, an increasing number of studies have demonstrated the effectiveness of plant-based nanoparticles for removing hazardous dyes, including methylene blue, rhodamine B, methyl orange, and azo dyes, as well as antibiotics and persistent organic pollutants. Adsorption remains one of the most widely used water treatment techniques due to its simplicity, low cost, and high efficiency [26]. Green-synthesized nanomaterials exhibit strong adsorption capacities because of their rich functional groups, tunable surface chemistry, and high affinity for both organic and inorganic pollutants [27]. For instance, plant-mediated metal nanoparticles and nanocomposites have demonstrated significant efficiency in adsorbing dyes and heavy metals from aqueous systems [28]. Eltaweil et al. reported that graphene oxide–cellulose acetate beads loaded with green nanoparticles exhibited excellent adsorption of methylene blue while maintaining good recyclability [29].

In parallel, photocatalysis has become an essential advanced oxidation process for degrading highly persistent pollutants [30]. Nanoparticles synthesized from plant extracts often exhibit enhanced photocatalytic activity due to their narrow band gaps, high electron mobility, and surface defects that promote charge separation [31]. Mariselvam et al. demonstrated the capacity of plant-based silver nanoparticles to degrade azo dyes under UV irradiation, with *Cocos nucifera*-derived AgNPs showing particularly high performance [32]. Similarly, Makofane et al. synthesized $CuFe_2O_4$ and Ag–$CuFe_2O_4$ nanoparticles using *M. burkeana* extract and showed their strong photocatalytic potential for degrading dyes and antibiotics [33]. Langa et al. reported that TiO_2 nanoparticles synthesized from *Sutherlandia frutescens* extract efficiently degraded Congo red dye and the antibiotics ciprofloxacin and sulfamethoxazole, confirming their applicability in treating mixed contaminant systems [34]. Green nanomaterials have also been used beyond water treatment, including soil purification and air pollution mitigation [35,36], highlighting their broad environmental relevance.

Despite these promising findings, the potential of green-synthesized nanoparticles in water treatment remains far from fully exploited. Variability in plant composition, limited understanding of reaction mechanisms, and challenges in scaling up production continue to constrain their widespread adoption. Nevertheless, their environmental friendliness, low cost, and strong adsorption and photocatalytic performance underscore their significance as next-generation materials for sustainable water purification.

The present review provides a comprehensive overview of plant-based nanoparticle synthesis from 2010 to 2025, with particular emphasis on their characterization and applications in water treatment. It examines the key parameters influencing green synthesis, evaluates structural and morphological features revealed through primary characterization methods, and analyzes their performance in adsorption and photocatalytic degradation of organic and inorganic pollutants. By consolidating recent advances and identifying existing gaps, this review aims to guide future research toward optimizing the design of green nanomaterials for effective and eco-friendly wastewater remediation.

2. Bibliometric Investigation of Scientific Trends

2.1. Database Sources and Statistical Processes

The bibliometric analysis was conducted using the Web of Science and Scopus databases, selected for their broad coverage of peer-reviewed journals in materials science, chemistry, nanotechnology, and environmental sciences. The literature search was conducted in December 2025 and covered publications indexed from January 2010 through December 2025.

The search was performed in the title, abstract, and author keyword fields using the following Boolean query:

("plant-based nanoparticles" OR "plant-mediated nanoparticles" OR "phyto-mediated nanoparticles" OR "green synthesized nanoparticles" OR "plant extract nanoparticles") AND ("nanoparticle synthesis" OR "green synthesis" OR "biosynthesis").

The initial query returned 18,439 records. To ensure scientific relevance and reproducibility, a stepwise screening procedure was applied. First, document types were limited to research articles and review papers, excluding conference proceedings, book chapters, editorials, and short communications. This step retained 18,297 records.

Second, subject-area filtering was applied to retain studies classified under materials science, chemistry, chemical engineering, environmental science, and nanotechnology, thereby excluding publications focused exclusively on biomedical, agricultural, or pharmaceutical applications without material or ecological relevance. After this screening, 18,102 records remained and were used for the bibliometric analysis.

Annual publication output was analyzed to evaluate temporal trends. Keyword co-occurrence analysis was performed using author-provided keywords. Before analysis, keywords were standardized by unifying singular and plural forms, harmonizing spelling variants, and merging closely related terms. Visualization, clustering, and density mapping were carried out using VOSviewer (version 1.6.20). Temporal overlay mapping was applied to identify emerging research directions.

Figure 1a illustrates the annual publication trend, showing limited activity before 2013, steady growth after 2015, and a pronounced increase from 2020 onward. This pattern reflects the rapid expansion of research on green nanomaterials driven by sustainability-oriented policies and environmental remediation needs.

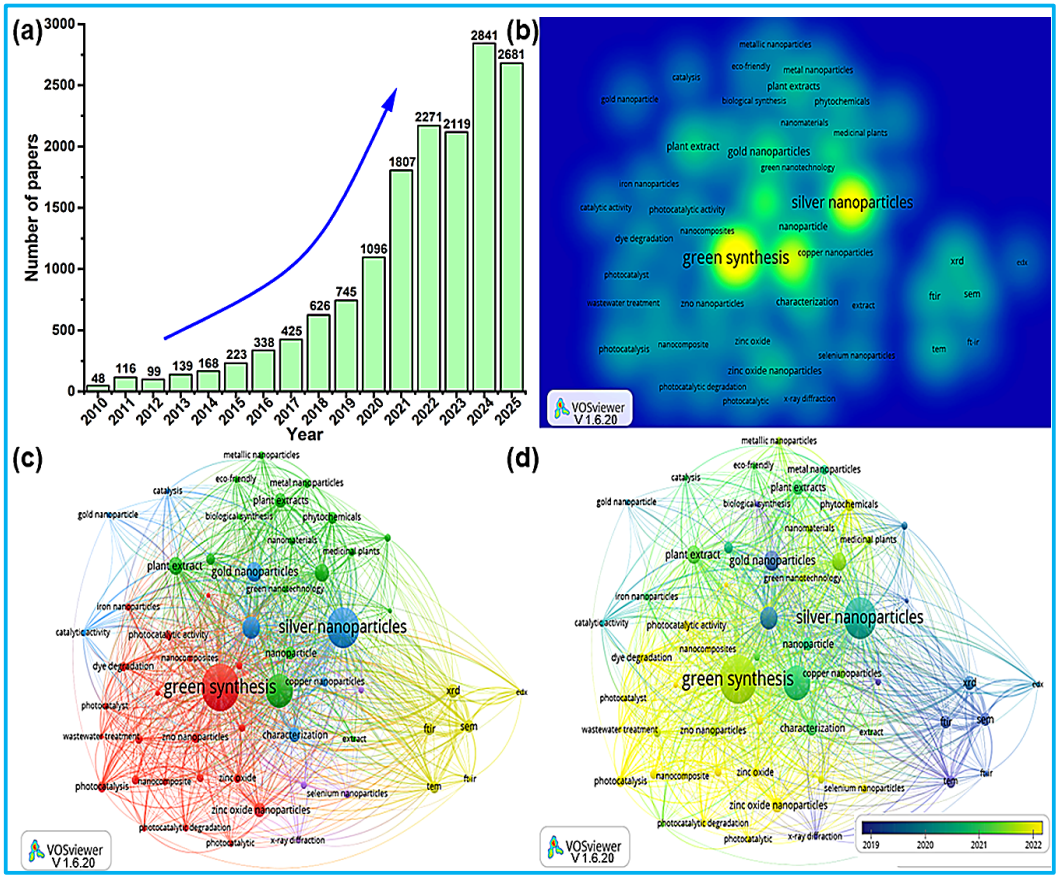


Figure 1. (**a**) The number of papers published on plant-based nanoparticles from 2010 to 2025, based on the ScienceDirect database. (**b**) Keyword co-occurrence frequency density distribution. (**c**) Keyword clustering network graph. (**d**) Research hotspots indicated by co-occurring keywords in recent years.

2.2. Keywords' Analysis

From the final dataset of **18,102 publications**, a total of **26,864 author keywords** were extracted. Frequency analysis shows that "**green synthesis**", "**nanoparticles**, "**silver nanoparticles**", and "**plant extracts**" are the most frequent terms, confirming that plant-mediated routes for metallic nanoparticle production dominate the literature.

Keywords directly associated with environmental applications are also well represented. The consistent appearance of terms such as "**adsorption**", "**photocatalysis**", "**water treatment**", "**pollutant removal**", and "**photodegradation**" underscores the growing role of plant-based nanoparticles in water purification technologies.

Cluster analysis (**3**) identifies three major thematic groups.

- **Cluster I** centers on synthesis-related concepts, including plant metabolites, reduction mechanisms, reaction conditions, and precursor salts, reflecting efforts to understand and control nanoparticle formation.
- **Cluster II** revolves around applications and includes keywords related to adsorption processes, photocatalytic degradation, wastewater treatment, and dye removal, with a focus on environmental remediation as a key research direction.
- **Cluster III** focuses on material properties and performance descriptors, such as particle size, surface chemistry, stability, crystallinity, and functionalization, indicating growing attention to structure–property–performance relationships.

Temporal overlay analysis (Figure 1d) shows a clear evolution in research priorities. Early studies focused primarily on demonstrating green synthesis routes and basic char-

acterization. More recent publications increasingly emphasize adsorption mechanisms, photocatalytic pathways, material optimization, and scalability, reflecting a transition toward application-driven and mechanism-based research.

In summary, the bibliometric analysis demonstrates a clear shift in the literature on plant-based nanoparticles from early synthesis-focused investigations toward application-oriented studies, with water treatment emerging as a dominant research direction. The complete bibliometric dataset of 18,102 records was used to identify publication trends, thematic clusters, and evolving research priorities at a global level. Guided by these outcomes, the manuscript then transitions to a focused technical synthesis by selecting 296 representative studies from clusters directly related to adsorption and photocatalytic degradation processes in water treatment. These studies were chosen based on clearly reported green synthesis routes, essential physicochemical characterization, and quantitative performance evaluation. They form the basis of the comparative tables and in-depth discussions presented in the subsequent sections. This structured progression from large-scale bibliometric mapping to targeted technical analysis ensures methodological transparency and provides a coherent framework for linking research trends with structure–property–performance relationships in plant-based nanomaterials for water remediation.

3. Green Synthesis of Plant-Based Nanoparticles

The technique of biological synthesis using plants or their parts, such as seeds, leaves, peels, roots, flowers, fruits, and stems, has been applied to extract plant extracts containing functional groups such as hydroxyl, amino, amine, and carboxyl groups from the derived biomolecules, enabling the reduction of metal salt precursors and the stabilization of nanoparticles [37]. The biosynthesis of nanoparticles using plant tissue extracts has been reported in several works across various plant varieties and plant parts to extract the desired-quality active ingredient in the presence of a metal salt solution (Figure 2). The nanoparticle synthesis process involves several stages. The first step is the preparation of plant tissue extracts from selected plants using two methods, aqueous extraction or alcoholic extraction. The second step is to create new nanoparticles by combining the plant extract with a metal salt solution. Their properties as biosynthetic nanoparticles, such as particle shape and size, are controlled by the type of plant extract, its concentration, pH, temperature, the concentration of the metal salt used, and contact time.

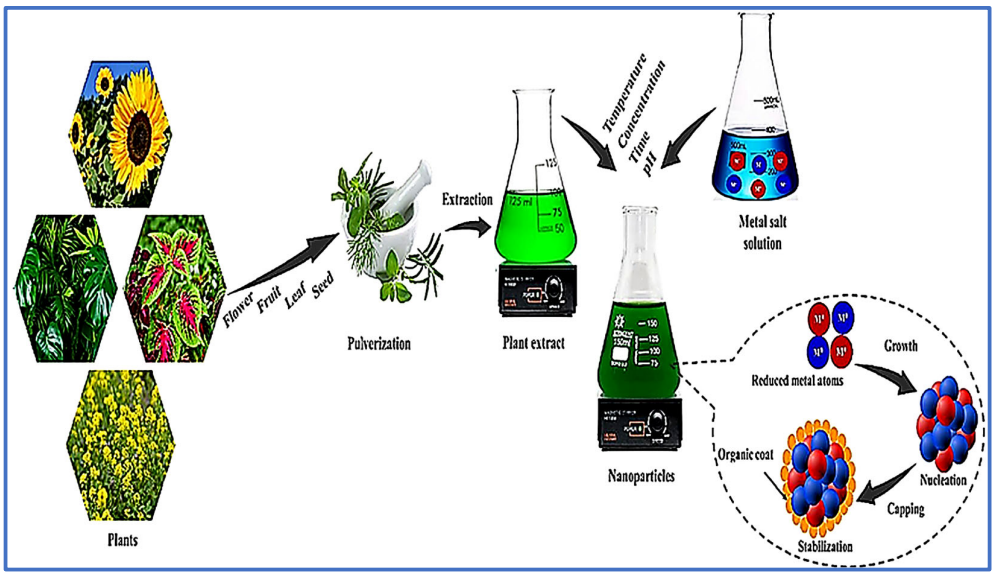


Figure 2. Schematic of the representation of nanoparticle synthesis using natural plant extracts and metal salt solution.

Based on literature surveys in the last few years, ecological synthesis has demonstrated environmentally friendly approaches to fabricating metal nanoparticles (NPs) such as silver nanoparticles (AgNPs), palladium nanoparticles (PdNPs), platinum nanoparticles (PtNPs), copper nanoparticles (CuNPs), nickel nanoparticles (NiNPs), selenium nanoparticles (SeNPs), iron nanoparticles (FeNPs), zinc nanoparticles (ZnNPs), gold nanoparticles (AuNPs), and titanium nanoparticles (TiNPs) using biological systems such as plant parts like leaves, roots, seeds, and fruits, as illustrated in Table 1. The main requirements for the green synthesis of iron nanoparticles of various sizes and shapes are plant extracts and iron solutions by the fusion method. This is the most straightforward and least expensive procedure for reducing and stabilizing iron ions by biomolecules from plant extracts. Iron-based nanoparticles can be derived from various plants, such as Phoenix dactylifera, *Prunus avium* stems, *tea*, and *Trigonella foenum-graecum*, and applied in environmental and biological applications.

Various plant extracts contain distinct profiles of biomolecules, including polyphenols, flavonoids, terpenoids, alkaloids, proteins, and other phytochemical compounds, which act as reducing agents, capping agents, and stabilizers during nanoparticle synthesis. These compounds differ in their chemical structure, concentration, and functional groups depending on the plant species, the part used, and the extraction conditions. As these biomolecules interact differently with metal ions, they influence the rates of reduction, nucleation, and nanoparticle growth, thereby altering particle size, shape, surface chemistry, and stability. For example, extracts rich in flavonoids and phenols may favor specific shapes, such as triangular or polyhedral nanoparticles, while others mainly produce spherical shapes [38]. Differences in extract composition also affect nanoparticle formation yield and kinetics. These structural and surface differences between nanoparticles are essential for catalytic performance. Smaller nanoparticles with a narrower particle size distribution generally offer a larger specific surface area and more active sites, thereby improving catalytic activity. In addition, molecules from the plant extract that coat the nanoparticles' surfaces can alter the nanoparticles' electronic properties and influence how reactants adsorb and interact with the catalyst surface, thereby affecting the activity, selectivity, and stability of catalytic processes. Furthermore, the stability conferred by certain specific coating agents can determine the catalyst's reusability and durability under reaction conditions [39].

Radini and associates reported on the biosynthesis of iron nanoparticles from iron precursors by the seed extract of the plant *Trigonella foenum-graecum*. They noted that using this plant substance is considered a green process that does not use harmful chemicals. The reduction of iron ions and their transformation into iron nanoparticles is mainly due to the water-soluble organic compounds present in this plant material, such as polyphenols, flavonoids, saponins, vitamins, amino acids, purines, and pyrimidines. The formation of FeNPs with sizes between 7 and 14 nm and a centered cubic structure is influenced by several factors, including time (5 min), temperature (30 °C), and pH (not specified). Consequently, the seed extract of the plant referred to above is a perfect source for the biosynthesis of iron nanoparticles with high antimicrobial activity and degradation of organic pollutants [40].

The pH of the synthesis medium is a well-established parameter that significantly influences several aspects of nanoparticle formation and properties. pH affects nucleation and growth kinetics by controlling the hydrolysis and precipitation behavior of metal precursors: at higher pH values, the increased availability of OH^- facilitates faster hydrolysis, promoting rapid nucleation and often resulting in smaller nuclei, while at lower pH values, the reduced hydrolysis rate slows nucleation and encourages the growth of larger particles. This phenomenon has been observed, for example, in SnO_2 systems, where acidic condi-

tions produce smaller particles due to the competitive effects of protonation/deprotonation on polymer stabilization and precursor chemistry [41]. Iron nanoparticles were synthesized using *Prunus avium* stem extract, containing terpenoids, polyphenols, proteins, flavonoids, biologicals, and other reducing agents. Fe nanoparticles can be produced by mixing 50 mL of plant extract with 50 mL of 0.1 M iron (III) chloride solution using a magnetic stirrer at room temperature, maintaining a pH of 11 until a black mixture forms. The resulting mixture was centrifuged, washed with ethanol and distilled water, and dried in an oven at 25 °C until it became a powder. Confirmation of Fe-nanoparticle formation was performed using UV–Vis, FT-IR, XRD, SEM, and Zeta-sizer particle size analyses. The formation of FeNPs was confirmed at 268 nm using UV–Vis methods. The Zeta-sizer particle size analysis confirmed the formation of 91.28 nm-sized Fe nanoparticles. These FeNPs showed high photocatalytic activity for the degradation of the cationic dye methylene blue, achieving 67.34% methylene blue removal at the 150th minute [42].

Silver nanoparticles (AgNPs) have been synthesized by several plant extracts like *Citrus lemon*, fresh and adult *Citrus limon*, *Citrus unshiu* fruit, and *Citrus reticulata blanco* by reducing aqueous silver ions. Alkhulaif et al. reported the biosynthesis of silver nanoparticles using *Citrus lemon* peel, owing to its high content of bioactive compounds and its various antibacterial and cytotoxic properties. In this work, silver nanoparticles were prepared by reacting an aqueous (1 mM) silver nitrate ($AgNO_3$) solution with 5 mL of Citrus *limon* peel extract (10 mL). The characterization data indicated the formation of predominantly spherical AgNPs with slight agglomeration and an average size of 59.74 nm. The authors concluded that AgNPs exhibit excellent antibacterial and cytotoxic activity against the human breast cancer and human colon carcinoma cell lines [43].

Sachin et al. used lychee peels collected from the local market in Delhi, India. They used *lychee* peel extract as a stabilizer and reductant. The characterization data showed the formation of spherical CuNPs with diameters < 10 nm. These synthesized CuNPs were applicable for degrading Congo red dye from wastewater and for their antibacterial properties [44]. Using extracts of *Nauclea latifolia* fruits and zinc nitrate hexahydrate, ZnNPs were prepared via a green route, as confirmed by analytical techniques. UV–Vis, XRD, TEM, and BET analysis methods indicated the formation of a broad peak at 373 nm and a hexagonal wurtzite structure with an average crystallite size of 14.40 nm, a particle size between 12.54 nm and 17.35 nm, and a specific surface area of 277.420 m^2/g, respectively [45]. Mali et al. employed *Celastrus paniculatus Willd*. Leaf as a synthetic agent, as it is rich in biological molecules such as flavonoids and other phenolic molecules, which are analyzed by the FTIR technique. A total of 5 mL of *Celastrus paniculatus* Willd. Leaf extract and 50 mL copper sulfate solution (5 mM) are mixed until a green color is obtained (pH = 7.0) due to the formation of CuNPs. Characterization by various methods demonstrated the formation of spherical particles ranging from 2 to 10 nm in size. The produced CuNPs demonstrated excellent catalytic activity for the decomposition of cationic dyes, such as methylene blue, in aqueous media, as well as good antifungal activity [46]. Likewise, *cocoa pod* fruit extract was applied to synthesize 20–50 nm CuNPs nanoparticles with irregular spherical morphologies. In the fruit extract, the presence of reducing agents, such as phenolic compounds and proteins, was responsible for nanoparticle synthesis. The ideal conditions for CuNPs synthesis using *cocoa pod* fruit extract were established as a volume ratio of 3.5/1.5 for $Cu(NO_2)_2$ solution and fruit extract, pH 7.5, temperature 75 °C, stirring speed 300 rpm, and synthesis time 180 min. The elaborated bio-nanoparticles demonstrated exemplary performance in the degradation of volatile compounds, including toluene, benzene, xylene (BTEX), and ethylbenzene [47]. More recently, A.S. Eltaweil et al. reported that an aqueous extract of *Cissus Atriplex halimus* leaf extract was used to synthesize platinum nanoparticles (PtNPs) from platinum chloride solution. The synthesis

was carried out at 95 °C and pH 9.5 for 60 min to obtain irregularly shaped aggregates of 1–2 nm and spherical structures. The microstructural and structural properties of PtNPs were analyzed using FT-IR, XRD, SAED, HRTEM, UV–Visible, XPS, zeta potential, SEM, and EDX techniques. The data analysis of the application of PtNPs in biological applications showed high antibacterial and antioxidant activities [48].

Palladium nanoparticles have been synthesized using various plant extracts, such as *Curcuma longa* root extract, via the reduction of $PdCl_2$ anhydrous. The eco-friendly method for preparing PdNPs from *turmeric* extract was evaluated for its antifungal, antioxidant, antibacterial, and anticancer activities [49]. Gold nanoparticles were formed by mixing the concentration of *Artocarpus odoratissimus* bark extract between 0.002 and 0.012 g/mL with 30 mL of 0.5 mM $HAuCl_4$ solution and reaction temperature (ambient temperature, 45 °C, and 75 °C) for evaluation of optical filter and catalytic degradation properties [50]. In another study, AuNPs were synthesized using *Citrus aurantium* skin extract, which acts as a reducing and stabilizing agent, and 20 mL $HAuCl_4$ (10 mM). The AuNPs synthesized and confirmed by TEM, EDX, UV-vis, FTIR, and XRD were quasi-spherical with an optimal size of 10–20 nm. Notably, these AuNPs demonstrated maximum anti-gastric carcinoma properties [51]. A study by Saka et al. explored the use of *Caricaceae* (papaya) shells for the eco-friendly synthesis of TiNP. By optimizing synthesis parameters at pH 11 and 85 °C for 5 h, the authors successfully generated TiNPs with a semispherical structure and an average diameter of 15 nm. Nanoparticles made from *Caricaceae* (papaya) shell showed potent antifungal effects against a range of fungal pathogens such as *Sclerotinia sclerotiorum, Fusarium spp.*, and *Rosellinia necatrix* [52]. Another work employed *Acorus calamus* leaf extract as a bioreducing and stabilizing agent to produce TiNPs. This process produced TiNPs with an average size of 15–40 nm, as confirmed by physicochemical characterization techniques. TiNPs exhibited notable photocatalytic activity, particularly in the decomposition of the dye Rhodamine B. In addition, TiNPs showed remarkable photocatalytic activity. In addition, TiNPs demonstrated excellent antimicrobial activity [53]. The data of works indicated the presence of various biomolecules such as alkaloids, amino acids, phenolics, proteins, amino acids, aldehydes, saponins, polysaccharides, and vitamins in plant extracts, and the effects of parameters such as solution pH, reaction time, treatment temperature, plant extract concentration, and metal ion concentration play an essential role in the reduction of salt solution metals and the formation of different sizes and shapes of green nanoparticles.

Several physicochemical techniques, including XRD, FTIR, SEM, TEM, EDX, and UV-Vis spectroscopy, were used to characterize the biosynthesized nanoparticles and assess their structure, morphology, size, composition, and optical properties.

Table 1. Green synthesis of green nanoparticles using various plant extracts.

Plant Species	Parts of Plants	Nanoparticles	Experimental Conditions	Shape and Size	Applications	Ref.
Prunus avium	Plant stems	Fe	pH = 11; 25 °C; 20 min;	91.28 nm	Cationic dye removal	[42]
Tea	Leaf		80 °C; 180 min	30–100 nm	Removal of Pb (II) and rifampicin	[54]
Trigonella foenum-graecum	Seed		30 °C; 5 min	7–14 nm	Photocatalytic methyl orange dye degradation and antibacterial applications	[40]
Citrus unshiu	Peel	Ag	60 °C; 2 h	Spherical 23 nm	Antibacterial and cytotoxic activity	[55]
Citrus reticulata Blanco	Peel		60 °C; 20 min	Spherical 10–35 nm	Photodegradation of malachite green dye	[56]
Mangifera indica	Seed	Zn	30 °C; 20 min	Cylindrical 40–70 nm	Activities and antioxidants	[57]
Rumex Nervosus Vahl	Leaf		80 °C; 90 min	43.44 nm, 69.82 nm, 84.86 nm	Antibacterial activity	[58]
Lychee	Peel		70 °C; 3 h	Hexagonal 2.18 nm	Anti-bacterial properties and CR dye removal	[44]
Nauclea latifolia	Fruits		60 °C	hexagonal wurtzite 14.40 nm	Methyl green dye adsorption	[45]
Celastrus paniculatus Willd.	Leaf	Cu	pH = 7.0; 60 °C	Spherical 2−10 nm	Photocatalytic and antifungal properties	[46]
Parthenium hysterophorus	Whole plant		15 min; 80 °C	Monoclinic 59.99 nm	Degradation of the rifampicin antibiotic	[59]
Cocoa pods	Fruits		pH (8.5–9.5) (70–80 °C), 60, 120, 180, and 210 min	Spherical 20–50 nm	Activity in the deep oxidation of aromatic hydrocarbons	[47]
Atriplex halimus	Leaf	Pt	pH = 9.6; 95 °C, 60 min	Spherical 1–3 nm	Antimicrobial, antioxidant, and catalytic applications	[48]
Cichorium intybus	Leaf		pH = 9; 90 °C; 120 min	-	Phytochemical, antioxidant, and antimicrobial properties	[60]
Nymphaea tetragona	Flower		25 °C; 30 min	2.82 nm and 1.95 nm	Skin lightening, anti-aging effects	[61]

Table 1. *Cont.*

Plant Species	Parts of Plants	Nanoparticles	Experimental Conditions	Shape and Size	Applications	Ref.
Origanum vulgare L.	Aerial parts	Pd	90 °C; 120 min	Spherical 2.2 nm	Oxidation catalyst towards aliphatic and aromatic alcohols.	[62]
Acacia ehrenbergiana	Leaf		2 h	-	-	[63]
Punica granatum	Peel	Pd	pH = 3; 37 °C; 24 h;	Face-centered cubic crystalline structure, 22 nm	Reduction of 4-nitrophenol	[64]
Scutellaria barbata	Plant	Au	60 °C; 30 min	Spherical 50 nm	Chemo-photothermal anticancer therapy	[65]
Artocarpus odoratissimus	Peel		Room temperature, 45 °C, and 75 °C	12–25 nm	Optical filter and catalytic degradation	[50]
Nicotiana plumbaginifolia	Leaf		Room temperature; 50 min	Spherical 18 nm	Anticancer properties against cervical cancer	[66]
Citrus aurantium	Peel		pH = 11; 60 °C; 60 min.	Quasi-spherical 20–50 nm	Treatment of gastric carcinoma	[51]
Moringa oleifera	Leaf and bark	Se	pH = 10; 60 °C; 60 min.	Spherical 17.2 nm and 20.1 nm	Targeting α-amylase and α-glucosidase enzymes in diabetes management	[67]
Ceropegia bulbosa	Roxb.		37 °C; 24 h	Spherical	Cytotoxicity, antimicrobial, mosquitocidal, and photocatalytic activities	[68]
Vaccinium arctostaphylos (L.)	Fruit		Room temperature; 24 h	Spherical; 50 nm	Anti-bacterial activities	[69]
Ocimum basilicum	Leaf	Ti	70 °C; 12 h	-	Photocatalytic degradation of amoxicillin residues	[70]
Caricaceae (Papaya)	Shell		pH = 11; 85 °C; 5 h	Semispherical as well as monoclinic, not spherical 15 nm	Antifungal application	[52]
Impatiens rothii Hook.f.	Leaf		80 °C; 3 h	11–25 nm	Removal of Methylene Blue Dye	[71]
Acorus calamus	Leaf		pH 7; Room temperature; 50 °C.	15–40 nm	Evaluating Its Photocatalytic and In Vitro Antimicrobial Activity	[53]

4. Physicochemical Properties of Plant-Based Nanoparticles

Various attributes, such as efficacy, safety, biodistribution, and behavior, can influence the physicochemical characteristics of plant-based nanoparticles. Characterization of plant-based nanoparticles was essential for assessing their functional properties, using a range of qualitative and quantitative analytical techniques. These methods can determine nanoparticle topography, shape, purity, distribution, and composition.

4.1. Crystalline Properties

XRD is commonly used to evaluate crystalline orientation, structure, atomic spacing, grain size, and deformation in plant-based nanoparticles. For example, the natural structure of aluminum oxide nanoparticles formed from *Phoenix dactylifera* seeds (Al_2O_3-NPs) was evaluated using XRD [72]. The X-ray source was Cu Kα (λ = 1.54056 Å) at 76 keV, and 2θ ranged from 10° to 100°. Diffraction peaks detected at 2θ = 32.00, 37.31, 48.17, 53.49, 63.70, 66.88, 79.02, and 90.51° were indexed to the (012), (104), (110), (113), (018), (214), (300), and (119) planes, respectively, revealing a rhombohedral lattice structure with an R3c space group. The average crystal size, determined from the highest peak at 2θ = 32.50° using the Scherrer equation, was approximately 32 ± 2.57 nm. The presence of additional minor diffraction peaks suggests the possible presence of secondary phases or residual impurities in Al_2O_3-NPs. In addition, the XRD pattern of iron oxide nanoparticles synthesized using the *Ajuga bracteosa* plant (Fe_3O_4-NPs) indicated characteristic diffraction peaks at 30.55, 35.45, 43.25, 53.61, 57.27, 63.1, and 74.20°, corresponding to the (200), (311), (400), (422), (511), (440), and (533) crystal planes of magnetite, respectively, as illustrated in Figure 3 [73]. The diffraction pattern is consistent with a cubic structure, while the average crystallite size was estimated at approximately 42 nm.

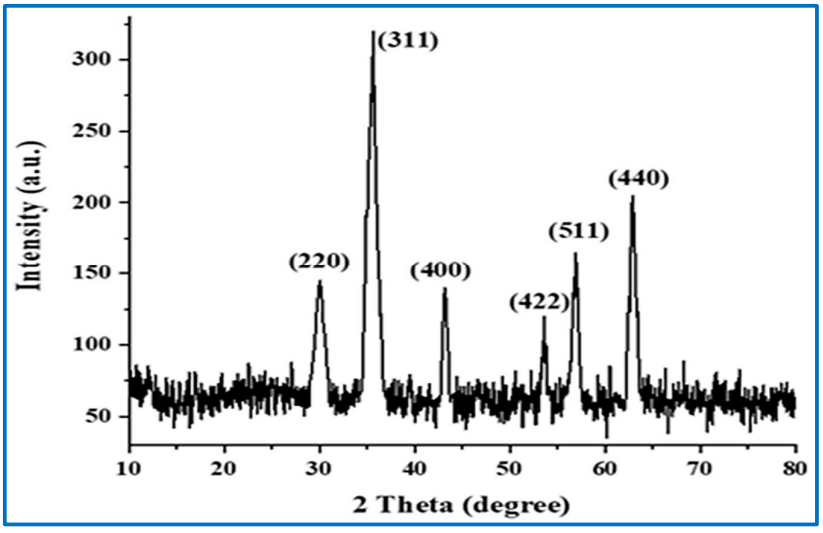


Figure 3. XRD spectrum of magnetite [73].

Eid et al. reported the green preparation of copper nanoparticles (CuO-NPs) using new *Portulaca oleracea* [74]. The XRD findings indicated the presence of eleven Bragg diffraction peaks at 33.1, 35.8, 38.9, 49.2, 53.7, 58.4, 61.7, 66.5, 68.2, 72.5, and 75.3°, which were attributed to the (110), (−111), (111), (−202), (020), (202), (−113), (−311), (220), (311), and (−222) crystalline planes, respectively. These data indicate that the CuO-NPs have a face-centered cubic crystal structure, with an average crystallite size of approximately 21 nm, calculated using the Debye–Scherrer equation.

In another study, Raj Jaishi et al. extracted zinc oxide nanoparticles from *Alnus nepalensis* D. Don (ZnONPs) and examined the ZnONPs crystallinity using a wavelength of 1.540 Å

at 30 kV to determine the crystalline structure, phases, and purity of the ZnONPs [75]. The patterns display the presence of strong and sharp diffraction peaks at 2θ values of 34.47°, 31.61°, 36.28°, 47.33°, 56.47°, 62.85°, and 67.90°, which correspond to the crystal planes (100), (002), (101), (102), (110), (103), and (112), respectively. The average crystallite size of the ZnO NPs was determined using the Debye-Scherrer formula, yielding a value of 15.31 nm. The work of Al Masoudi et al. investigated the synthesis and characterization of *Juniperus* vinifera leaf-based titanium dioxide nanoparticles (TiO_2NPs) [76]. According to the XRD results, the peaks observed at 2θ = 27.1, 35.7, 40.8, 43.9, 53.9, 56.0, 63.9, 68.8, and 69.8° were indexed to (110), (101), (111), (210), (211), (220), (310), (301), and (112) planes, respectively. The sharpness of the diffraction peaks confirmed the crystalline structure and the high purity of the TiO_2NPs, with an average crystalline size of approximately 10 nm.

Muhaymin et al. reported the synthesis and structure analysis of magnesium oxide nanoparticles extracted from *Hyphaene thebaica* (MgONPs) using XRD [77]. The diffraction peaks at 36.94, 42.86, 62.30, 74.70, and 78.62° were attributed to hkl planes (111), (200), (220), (311), and (222) planes, respectively, confirming a cubic MgO phase. The calculated lattice constant was 4.213 Å, and the average crystallite size was approximately 30 nm. The calculated lattice stress (2.35×10^4) and dislocation density (1.11×10^{15} lines/m^2) indicated a high dislocation density and a small crystal size, suggesting low crystallinity.

Nevertheless, Gingasu et al. applied XRD analysis to determine the size and crystallinity of cobalt ferrite magnetic nanoparticles ($CoFe_2O_4$-NPs) synthesized from eucalyptus leaf extract [78]. The measurements were performed with Cu Kα radiation (λ = 1.5406 Å) at 40 kV and 30 mA. A heat treatment was performed at 800 °C to improve the crystallinity of $CoFe_2O_4$-NPs ($CoFe_2O_4$-NPs-800), as presented in Figure 4. XRD analysis showed diffraction peaks corresponding to the (111), (220), (311), (222), (400), (331), (422), (511), (440), (531), (620), (533), (622), and (444) planes, consistent with a face-centered cubic spinel structure of $CoFe_2O_4$-NPs. After heat treatment at 800 °C ($CoFe_2O_4$-NPs-800), the diffraction peaks became sharper and narrower, reflecting an enhancement in crystallinity. The lattice parameters of $CoFe_2O_4$-NPs and $CoFe_2O_4$-NPs-800 were 8.3114 Å and 8.38364 Å, respectively, and the average crystal sizes of $CoFe_2O_4$-NPs and $CoFe_2O_4$-NPs-800, calculated using the Scherrer method, were 3 nm and 20 nm, respectively. A better crystallinity was noticed from the narrow and sharp peaks of $CoFe_2O_4$-NPs-800.

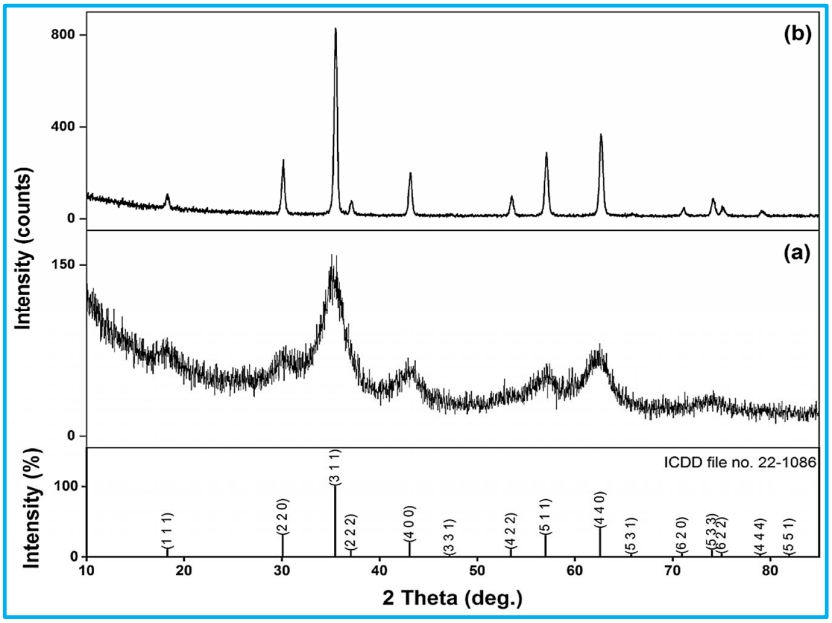


Figure 4. XRD patterns of (**a**) $CoFe_2O_4$NPs and (**b**) $CoFe_2O_4$NPs-800 [78].

While X-ray diffraction provides details of the crystal structure, understanding the chemical bonds and surface functional groups of nanoparticles requires spectroscopic analysis, such as FTIR.

4.2. Functional Properties

FTIR identifies the biomolecules and functional groups involved in the stabilization and reduction of nanoparticles. Peaks corresponding to -COOH, -OH, and other organic fragments indicate encapsulation by plant metabolites. In particular, Khan et al. analyzed *Spirodela polyrhiza*-based copper oxide nanoparticles (CuONPs) using the FT-IR method [79]. According to the findings, CuONPs exhibit several bands, including the symmetric and asymmetric alkane bands at 1096 cm^{-1} and 1038 cm^{-1}, respectively; the stretching vibration of O-H at 3291 cm^{-1} and 2965 cm^{-1}, respectively, which is attributed to phenols and alcohols; and the presence of C-O ester at 1640 cm^{-1}. The zinc oxide nanoparticles extracted from *green algae* (ZnONPs) were examined via FTIR to identify the functional groups and the phases present [80]. Figure 5 compares the FTIR spectra of ZnONPs synthesized by zinc nitrate and zinc acetate as precursors and *green algae* extract as a reducing agent. The results revealed that the FTIR spectrum exhibits strong bands of O-H phenolic or alcoholic compounds clearly at 3400 cm^{-1} and 3300 cm^{-1}, respectively, while the bands located at 3000 cm^{-1} and 3050 cm^{-1} represent the stretching vibrations of the C-H bond alkane group. The carbonyl stretching of proteins was observed between 1600 and 1550 cm^{-1}, matching the amide I and II stretching vibration bands, while the band at 500 cm^{-1} was attributed to ZnO, confirming the formation of ZnONPs. The bending vibration of C-H and C-N between 950 and 1000 cm^{-1} was related to the substances extracted from *green algae* (aliphatic and aromatic amines). Furthermore, the FTIR spectra of ZnONPs showed the involvement of functional groups from proteins, carbonyls, amino acid residues, and hydroxyls extracted from green *algae* in the reduction and encapsulation process of ZnONPs.

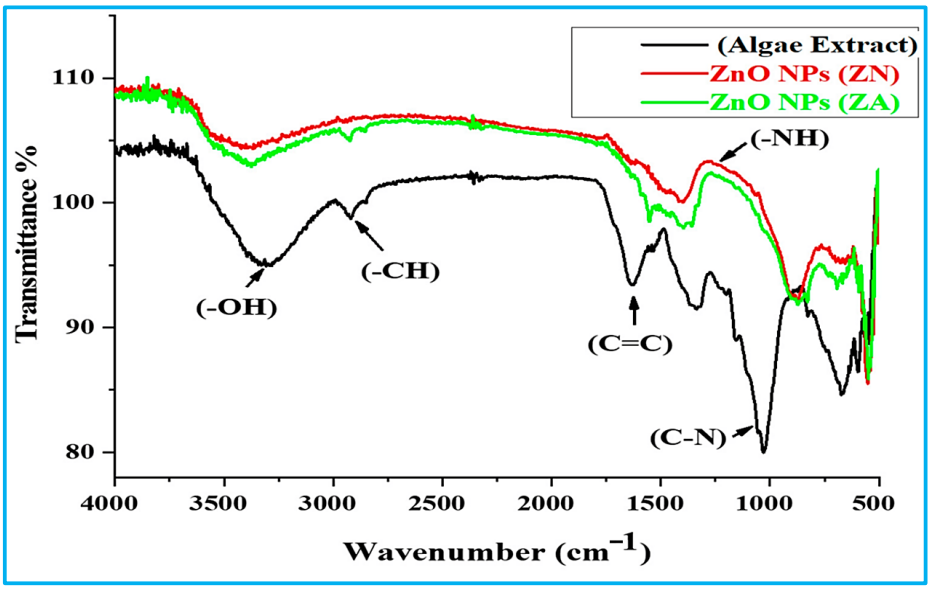


Figure 5. FTIR spectra of ZnONPs synthesized using zinc nitrate, zinc acetate, and *algae* extract [80].

In another study, FTIR analysis was used to identify the functional groups of *Leucas aspera* leaf-based titanium dioxide nanoparticles (TiO_2NPs) synthesized via a green method [81]. The bands at 3099.68 and 2989.65 cm^{-1} correspond to C-H stretching vibrations of the alkane group. The bending vibrations of C-H were achieved at 814.42 and 980.877 cm^{-1}, while the bands at 2786.65 and 2805 cm^{-1} resemble the symmetrical stretching vibrations of CH_2, and the stretching vibration of CH_3 was identified at 1367.39 cm^{-1}.

The asymmetrical stretching vibration of C-H was reached at 2952.97 cm^{-1}. The vibrations observed in the FTIR spectrum indicate the different functional groups involved in the formation of TiO_2NPs.

Babiker et al. reported the analysis of aluminum oxide nanoparticles extracted from *mint* leaves (Al_2O_3NPs) using FTIR spectroscopy [82]. The bands at 1978 cm^{-1} and 2032 cm^{-1} characterize alkene groups' C=C and aromatic ring vibrations (terpenoid and flavonoid). The stretching and symmetric bending vibrations of alkenes and Al-O-H were distinguished at 2160, 1030, and 991 cm^{-1}, respectively. It was evident that the structure of Al_2O_3NPs was formed from the bands located at 655 cm^{-1} and 550 cm^{-1} attributed to Al-O-Al and Al-O vibrations, respectively. The FTIR results confirmed the high purity and stability of Al_2O_3NPs. The functional groups of *Abrus precatorius*-based magnesium oxide nanoparticles (MgONPs) were investigated by FTIR analysis [83]. The bands at 3416 cm^{-1} and 3279 cm^{-1} corresponded to the stretching vibrations of phenolic and alcoholic O-H groups, respectively. The stretching vibrations of alkyl halide groups and proteins were manifested by the C-Cl, C-Br, and C-N at the bands 573, 661, and 1065 cm^{-1}, respectively. The band at 2824 cm^{-1} indicates the presence of stretching vibrations of C-H, while the vibration of C=C was located at 2042 cm^{-1}, and the band at 2367 cm^{-1} was compatible with the stretching vibration of C=C. The vibration of C=O was perceived at 1610 and 1391 cm^{-1}. The FTIR spectrum of MgONPs confirms the presence of significant functional groups, including alkynes, alkyls, phenols, alcohols, and amides, indicating the stability of MgONPs.

The study by Kushwaha et al. analyzes the FTIR spectrum of cobalt ferrite magnetic nanoparticles ($CoFe_2O_4$NPs) synthesized from *Hibiscus rosa-sinensis* flowers and leaves [84]. It was indicated that the bands at 462.92 cm^{-1} and 579.64 cm^{-1} correspond to Co-O and Fe-O vibrations, respectively, indicating the formation of metal oxide bonds in $CoFe_2O_4$NPs. The bending vibration of C-O was assigned to 1382.96 cm^{-1}, and the band at 1531.48 cm^{-1} was attributed to the bending vibration of C-H. The bands at 902.48 cm^{-1} represent the stretching vibration of alkoxy C-O from epoxy, carboxyl, and carbonyl groups containing oxygen atoms. The symmetric and asymmetric stretching vibration bands of the alkoxy-COOH carboxylic group were situated at 1693.50 cm^{-1} and 1762.93 cm^{-1}, respectively. The FTIR results indicate the successful formation of $CoFe_2O_4$NPs. Nevertheless, the silver oxide nanoparticles extracted from *Plectranthus amboinicus* and *Solanum trilobatum* (AgONPs) were characterized by FTIR spectroscopy, as shown in Figure 6 [85].

The stretching vibrations of O-H groups were identified at the bands 2923.51, 2395.18, and 3440 cm^{-1}. The bands at 1378 cm^{-1} and 1762 cm^{-1} correspond to the asymmetric and stretching vibrations of SO_2 and C=O, respectively. The bending vibration of the N-H group was found at 1620 cm^{-1}. The bands at 417.22, 477.13, 660, 825, and 3400 cm^{-1} were ascribed to bending and stretching vibrations of S-S, Ag-S, S-O, and Ag-O, respectively, demonstrating the formation of AgONPs. The FTIR analysis confirms the stability of AgONPs.

In addition to surface chemistry, particle size distribution and morphology are significant factors in determining nanoparticle properties, which can be visualized using a scanning electron microscope.

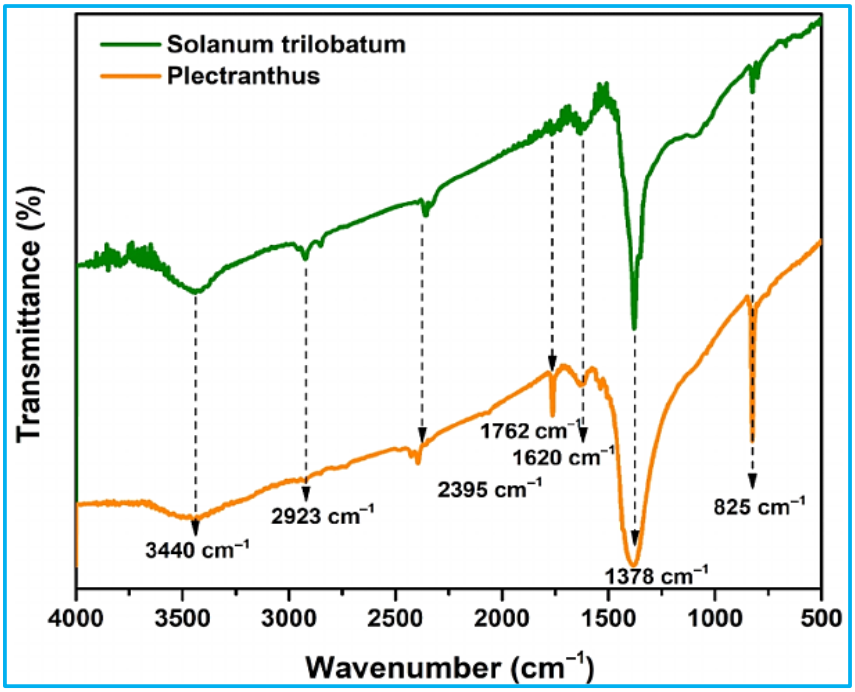


Figure 6. FTIR patterns of AgONPs extracted from *Plectranthus amboinicus* and *Solanum trilobatum* [85].

4.3. Morphological Properties

4.3.1. SEM Analysis

SEM provides high-resolution images of the nanoparticles' surfaces, revealing their size, aggregation patterns, and shapes. It enables the assessment of their uniformity and form, whether irregular, rod-shaped, or spherical. For instance, Shabir et al. synthesized two types of nickel oxide nanoparticles ($NiONPs_{(aqueous)}$ and $NiONPs_{(ethanolic)}$) extracted from *Acacia nilotica* leaves and examined them using SEM [86]. Figure 7 shows the SEM images of $NiONPs_{(aqueous)}$ and $NiONPs_{(ethanolic)}$. It was revealed that the $NiONPs_{(aqueous)}$ were an agglomerated composite particle; this lack of disintegration was due to the significant surface tension and high surface energy of the NiONPs. The size of NiONPs was 16 nm. The fine structure of the $NiONPs_{(ethanolic)}$ consists of well-crystallized, monodispersed tetragonal-shaped composites with an average size of 28 nm. Additionally, Shi-Yan Cheah et al. investigated the surface morphology of chromium oxide nanoparticles derived from dried *pomegranate* husk (Cr_2O_3NPs) using SEM [87]. A high purity was observed, signifying that the Cr_2O_3NPs were not completely disaggregated and exhibited a spherical shape with an average size of 100 nm.

The SEM analysis of *basil* seed-based lead oxide nanoparticles (PbONPs) was performed to characterize their surface morphology and particle size [88]. The PbONPs synthesized were agglomerated, pure, and spherical, with a diameter of 29.4 nm and a homogeneous surface. The work of Castillo-Saenz et al. studied the surface morphology of cerium oxide nanoparticles (CeO_2NPs) extracted from *Lycium cooperi* [89]. The SEM images presented in Figure 8 show the spherical shape and the homogeneous, porous surface of CeO_2NPs. In addition, the green synthesis of manganese dioxide nanoparticles (MnONPs) extracted from *Punica granatum* leaves was examined by SEM microscopy [90]. The diameter size of MnONPs ranged between 40 and 80 nm, with an irregular structure, and was loosely agglomerated. This agglomeration was attributed to electrostatic attraction forces.

Kolahalam et al. report the extraction of cobalt oxide nanoparticles (Co_3O_4NPs) from the *Lawsonia inermis* bark and leaves via a green synthesis approach [91]. SEM analysis was used to determine the surface morphology of Co_3O_4NPs (Figure 9). The

surface was found to be homogeneous, indicating weak nanoparticle agglomeration, and the nanoparticles appeared spherical at the nanoscale, with an average size of 98.05 nm. The morphological and topographical characteristics of *Ficus carica*-based calcium oxide nanoparticles (CaONPs) were considered using SEM microscopy [92]. The surface of CaONPs showed that some particles were spherical, while others were irregular and heterogeneous, with agglomerates present. The diameter of these nanoparticles was around 84.87 nm.

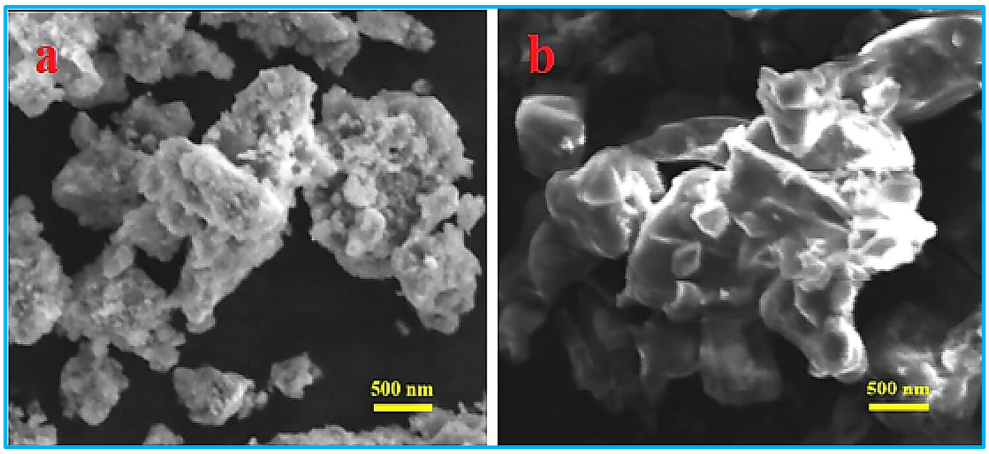


Figure 7. SEM images of (**a**) NiONPs-ethanolic and (**b**) NiONPs-aqueous [86].

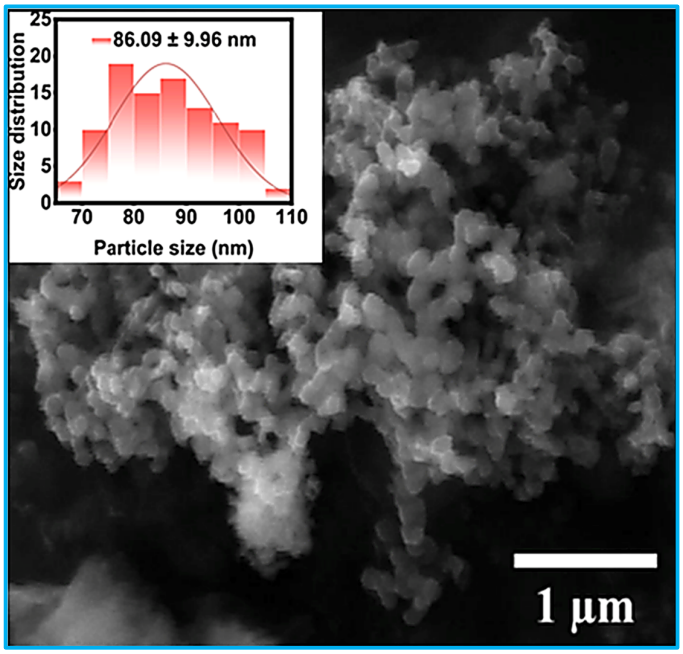


Figure 8. SEM micrographs of CeO_2NPs [89].

pH variations also strongly influence the particle size distribution and morphology. For instance, in the synthesis of silver nanoparticles, pH alters the rate of aggregation and dissolution, with higher pH values generally producing smaller particles with narrower distributions and better colloidal stability due to reduced aggregation [93]. Furthermore, pH-induced changes in surface charge directly govern colloidal stability via electrostatic repulsion between particles; according to classical DLVO theory, as the zeta potential moves away from the isoelectric point with increasing or decreasing pH, particles carry larger net charges that enhance repulsive forces and suppress aggregation [94].

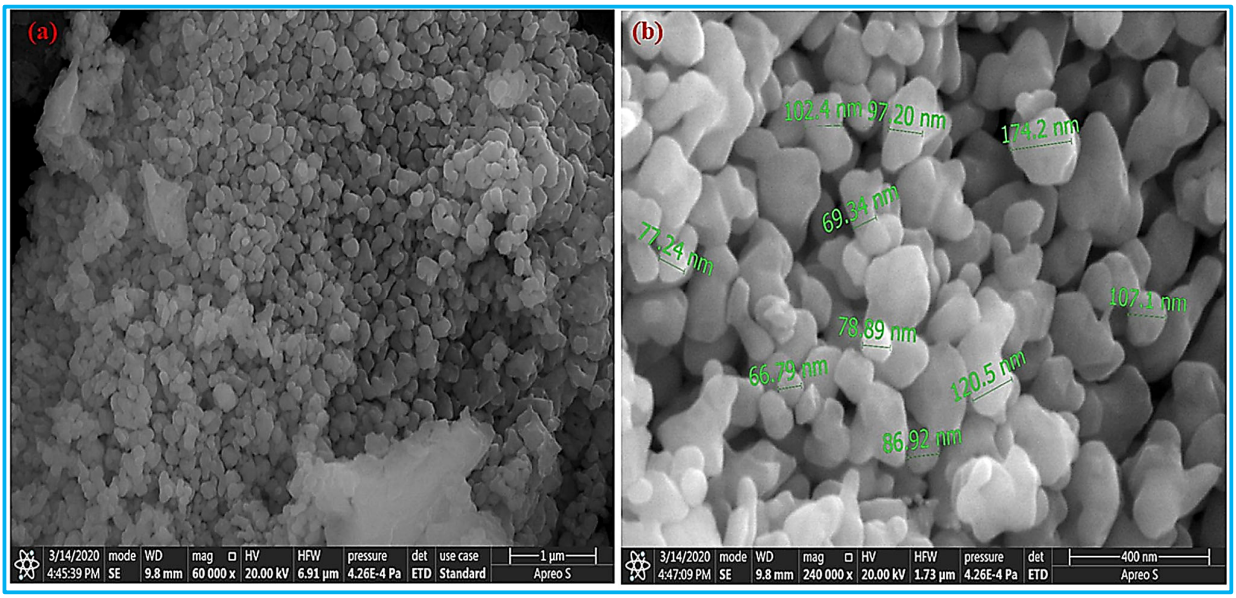


Figure 9. SEM images of Co_3O_4NPs at (**a**) 1 µm and (**b**) 400 nm [91].

Alongside morphology, verifying elemental composition is crucial; this can be achieved using EDX analysis.

4.3.2. EDX Analysis

EDX identifies the elemental composition of nanoparticles, confirming the presence of target metals and other constituents, often directly on SEM images. For example, the chemical composition of vanadium oxide nanoparticles (V_2O_5NPs) synthesized from the extract of *Punica granatum* was determined by EDX analysis [95]. Figure 10 shows the EDX spectrum of V_2O_5NPs. Strong signals for vanadium and oxygen atoms were observed in V_2O_5NPs. The results suggest a high vanadium content in the V_2O_5NPs, with a calculated percentage of 73.3%, while oxygen accounts for 26.7%, reflecting the high purity of the V_2O_5NPs.

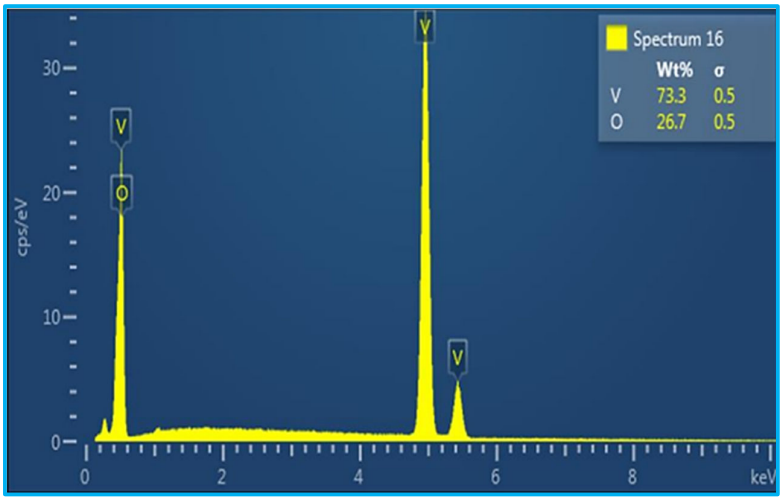


Figure 10. EDX spectrum of V_2O_5NPs [95].

The study conducted by Parvathiraja et al. involves the synthesis of zirconium oxide nanoparticles (ZrO_2NPs) using the extract of *Murraya koenigii* [96]. EDX was used to determine the composition of ZrO_2NPs. The EDX spectrum showed absorption peaks for zirconium ions (Zr^{4+}) and oxygen ions ($O_2{}^-$) at 69.24% and 27.2%, respectively, indicating

the formation of ZrO_2NPs. A peak for carbon atoms was also detected at 3.56%, which can be attributed to plant biometabolite emission.

To understand the nature of the elements present in the MoO3NPs nanoparticles synthesized via green synthesis using Terminalia arjuna tree bark extract, EDX analysis of the MoO_3NPs was conducted [97]. These analysis results showed that the central element in the MoO_3NPs was molybdenum, with a weight percentage of 84.43%, followed by oxygen atoms at 15.57%, indicating the high purity of the MoO_3NPs. In another study, the surface compositions of tin oxide nanoparticles (SnO_2NPs) formed from *cotton boll* peel extract were evaluated by EDX at 200, 500, and 800 °C, as shown in Figure 11 [98]. The EDX results exposed a slight variation in the weight percentage of the SnO_2NPs elements as a function of temperature. At 200 °C, it was observed that the atomic composition of SnO_2NPs contained 86.59% of tin atoms and 13.41% of oxygen (Figure 11a), suggesting that this sample was free of impurities. At 500 °C, absorption peaks for oxygen and tin atoms were detected with weight percentages of 12.40% and 87.60% (Figure 11b), respectively, confirming the presence of SnO_2NPs in this sample with multiple crystals and no impurities. Strong signals for the tin element were also noted at 89.87% and 10.13% oxygen at 800 °C (Figure 11c), demonstrating the high purity of SnO_2NPs.

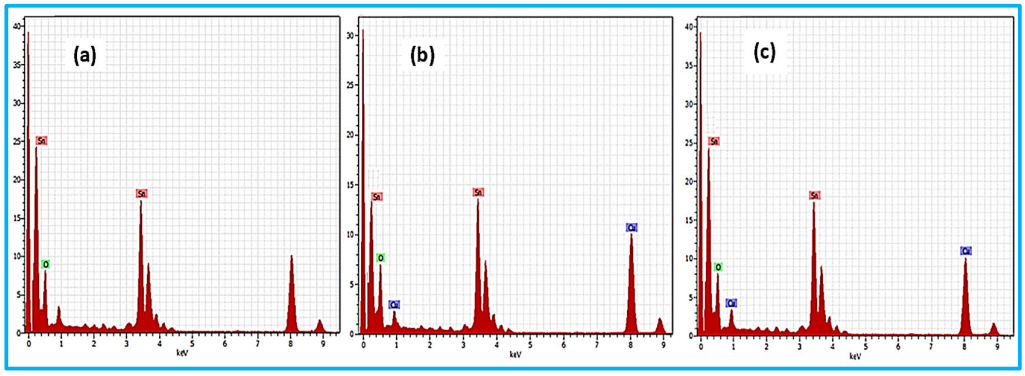


Figure 11. EDX spectra of SnO_2NPs synthesized at diverse temperatures: (**a**) 200 °C, (**b**) 500 °C, (**c**) 800 °C [98].

Duraisamy et al. reported the racemic structures of silicon dioxide nanoparticles (SiO_2NPs) synthesized from *Azadirachta indica* by EDX analysis [99]. The EDX spectrum showed prominent peaks with high intensities, attributed to silica and oxygen, providing strong evidence for the formation of high-purity SiO_2NPs and the absence of impurities. Olive tree bark extract was used to synthesize zinc ferrite nanoparticles loaded with zinc oxide ($ZnFe_2O_4$NPs) via a green method [100]. The surface chemical composition of $ZnFe_2O_4$NPs was studied using EDX analysis, as shown in Figure 12. The results confirmed a uniform distribution of the elements constituting $ZnFe_2O_4$NPs, including iron, zinc, and oxygen, indicating the purity of $ZnFe_2O_4$NPs.

To achieve even finer structural details and observe internal characteristics, a transmission electron microscope (TEM) is used, enabling a more in-depth examination of particle size and crystal lattice fringes.

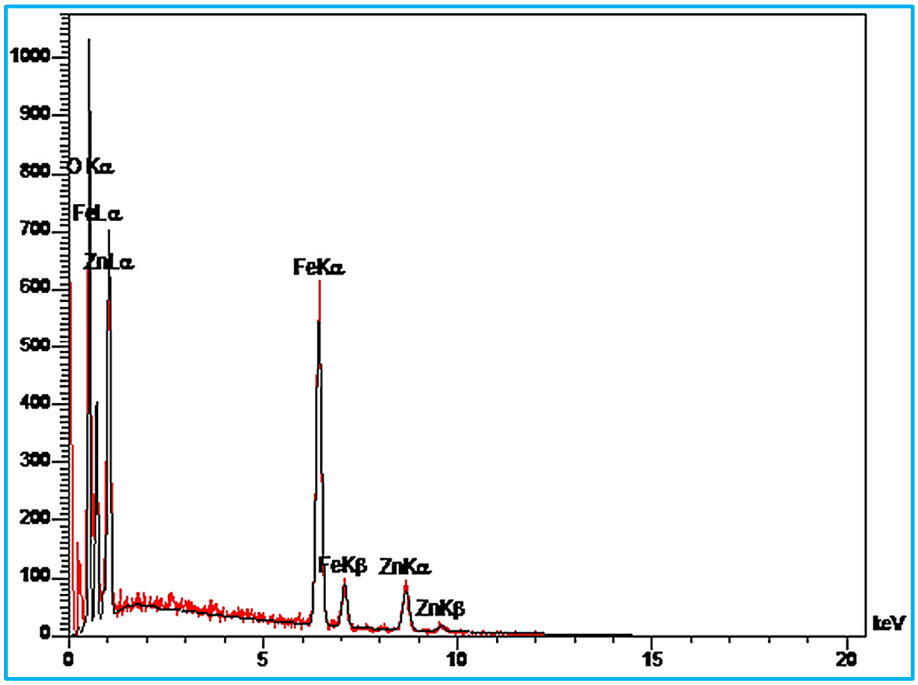


Figure 12. EDX spectrum of $ZnFe_2O_4$NPs [100].

4.3.3. TEM Analysis

TEM provides high-magnification images that can be used to determine particle size, shape, and internal structure. It can also measure diffraction patterns to confirm crystallinity at the nanometer scale. The sizes and shapes of the plant-derived antimony oxide nanoparticles (Sb_2O_3NPs) extracted from *Chenopodium album* leaves were analyzed using TEM microscopy [101]. The analysis findings showed that the Sb_2O_3NPs consist of an ensemble of reflective rings, exhibiting a polycrystalline structure. The particle size of Sb_2O_3NPs was approximately 40 nm, with a spherical shape. Prakash Moorthy et al. conducted TEM analysis using electron beams to visualize the microstructure, size, and shape of bismuth oxide nanoparticles (CP-BiONPs) synthesized from *Murraya koenigii* extracts [102]. Figure 13 shows the TEM images of CP-BiONPs. It was revealed that the CP-BiONPs have a well-defined nanostructure, indicating an organized distribution. At the same time, the particle size was around 20 nm, with a good crystalline structure, resulting in high productivity.

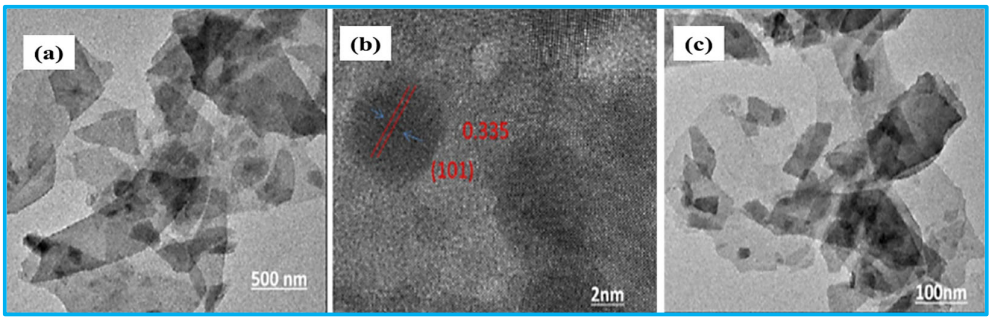


Figure 13. TEM images of CP-BiONPs at (**a**) 500 nm, (**b**) 2 nm, and (**c**) 100 nm [102].

Therefore, TEM images visually depict the morphology and structure of ZnO-SnO_2 NPs synthesized from *banana* peel extract [103]. The ZnO-SnO_2 NPs exhibit a nearly spherical shape with existing agglomerates of ZnO and SnO_2 particles. The average size of these nanoparticles was 7.28 nm. Iqra et al. used the extract of the *Indica azadirachta*

leaves to synthesize green tungsten oxide nanoparticles mixed with tantalum (Ta-WO_3NPs) using concentrations ranging from 1 to 5% [104]. The crystal morphology, size, and shape of Ta-WO_3NPs particles obtained via green synthesis were studied using TEM microscopy, as shown in Figure 14.

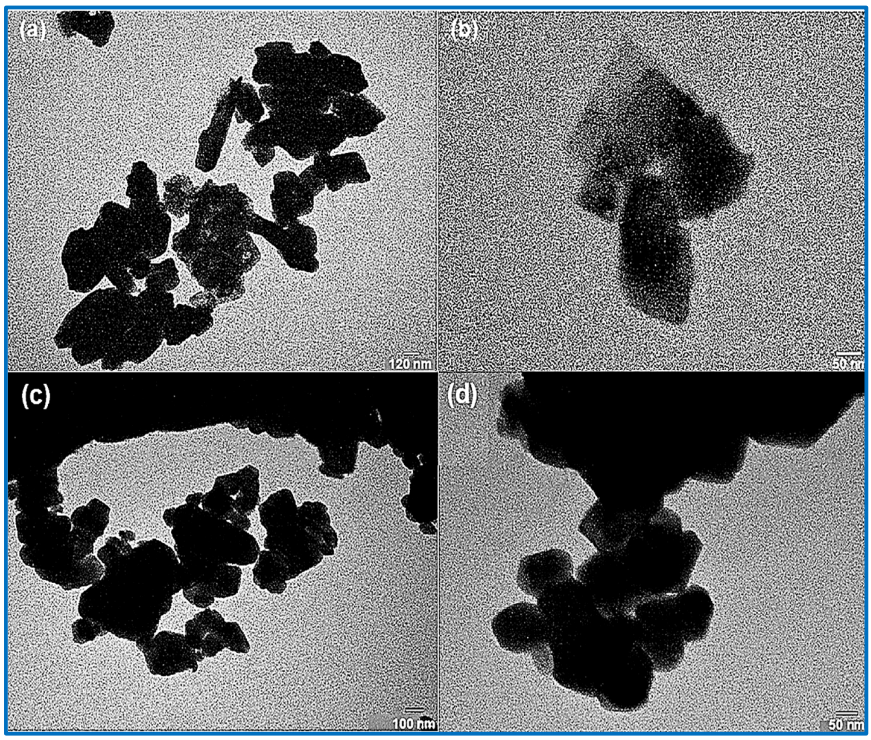


Figure 14. TEM images of WO_3NPs at (**a**) 120 nm, (**b**) 50 nm, and Ta-WO_3NPs at (**c**) 100 nm and (**d**) 50 nm [104].

WO_3NPs form highly agglomerated rod-shaped aggregates due to particle stacking and interparticle interactions (Figure 14a,b), which result in irregular morphology and non-uniform particle size distribution. Conversely, more homogeneous, primarily spherical Ta-WO_3NPs with less agglomeration form when 3% tantalum is added (Figure 14c,d). The average particle size of Ta-WO_3NPs was determined to be 31.6 nm. The addition of Ta promotes controlled nucleation and growth, thereby improving structural homogeneity and particle dispersion, as evidenced by greater uniformity and reduced agglomeration. Overall, Ta-WO_3NPs exhibit greater morphological uniformity, higher product purity, and better crystallinity than WO_3NPs, indicating that Ta ions were successfully incorporated into the WO_3 lattice.

To gain additional insights into the morphology and size of lithium cobalt oxide nanoparticles ($LiCoO_2$NPs) extracted from *aloe vera* [105], TEM studies were conducted on $LiCoO_2$NPs heated at 800 °C (Figure 15). The $LiCoO_2$NPs consist of aggregates with nearly spherical shapes and some particles exhibiting polyhedral shapes. The average size of $LiCoO_2$NPs was estimated to be 87.34 nm.

The plant *Oldenlandia umbellata* L. was used for the green synthesis of cerium oxide nanoparticles loaded with nanoscale cerium oxide (CeO_2-OsO_4NPs) [106]. The shape and structure of the CeO_2-OsO_4NPs nanoparticles were examined using TEM microscopy, as presented in Figure 16. The TEM image shows a compact distribution of spherical nanoparticles with sizes ranging from 22 to 24 nm. It was designated that the CeO_2-OsO_4NPs aggregate was homogeneous with single-directional crystalline structures. The regular distribution of spherical nanoparticles and the correspondence between the average particle size and the crystal sizes confirm the good dispersion of CeO_2-OsO_4NPs without agglomeration.

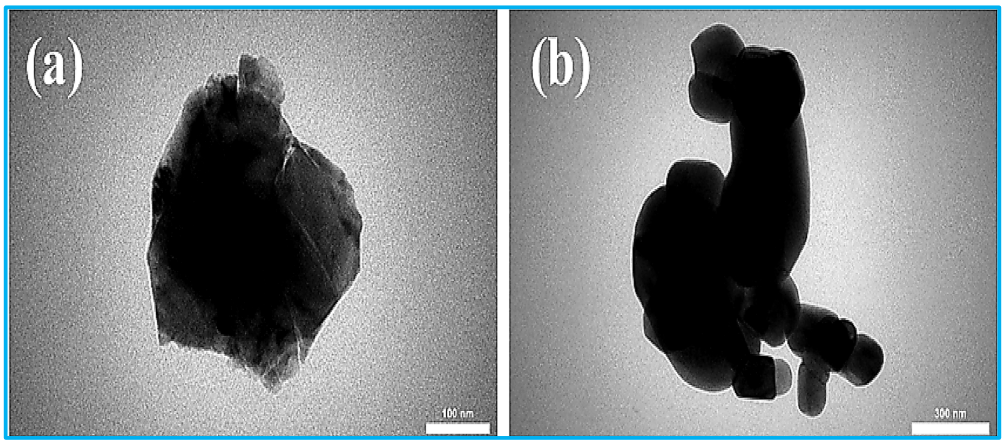


Figure 15. TEM images of $LiCoO_2$NPs at (**a**) 100 nm and (**b**) 300 nm [105].

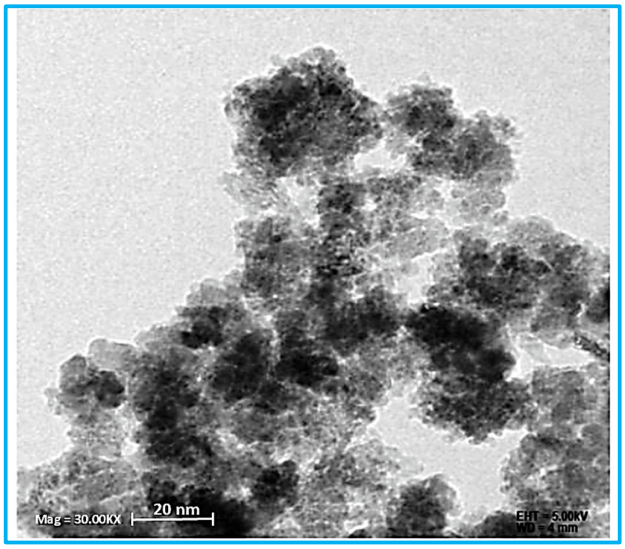


Figure 16. TEM images of CeO_2-OsO_4 NPs [106].

Acosta et al. synthesized ZnO nanoparticles using *Ambrosia ambrosioides* leaf and root extract. To determine the structure, size, and shape of the AA_S_ZnO, corresponding to the ZnO nanoparticles obtained with the leaf extract (AA = Ambrosia ambrosioides and S = Sheet), and AA_R_ZnO for the nanoparticles obtained with a root extract of Ambrosia ambrosioides (R = Root) [107].

TEM/SAED analysis was conducted and presented in Figure 17. The TEM images indicated that the elaborated ZnO nanoparticles exhibit different sizes and morphologies depending on the plant part applied for synthesis. The AA_R_ZnO nanoparticles indicated a mixture of irregular and crystalline shapes (Figure 17a), with particle sizes smaller than 10 nm and extending up to 56 nm (Figure 17a,b). On the other hand, the AA_S_ZnO nanoparticles showed mostly quasi-spherical shapes (Figure 17d) and sizes ranging from 10 nm to 51 nm (Figure 17d,e).

A comparative study of the microstructure by SEM and TEM (Figure 18) of silver nanoparticles (AgNPs) synthesized using various plants like *Arctium lappa* fruit (Al-AgNPs), *Solanum melongena* leaves (Sm-AgNPs), and *Taraxacum mongolicum* leaves (Tm-AgNPs), was assessed by Tian et al. The results indicated that the nanoparticles were predominantly spherical, with average diameters of about 20.18 nm (Al-AgNPs), 21.00 nm (Sm-AgNPs), and 40.08 nm (Tm-AgNPs), suggesting extract-dependent growth behavior. These variations can be attributed to differences in phytochemical composition, particularly the concentrations and types of flavonoids and polyphenols, as well as the other reducing and

capping agents present in each extract, which control nucleation, stabilization, and particle growth [108].

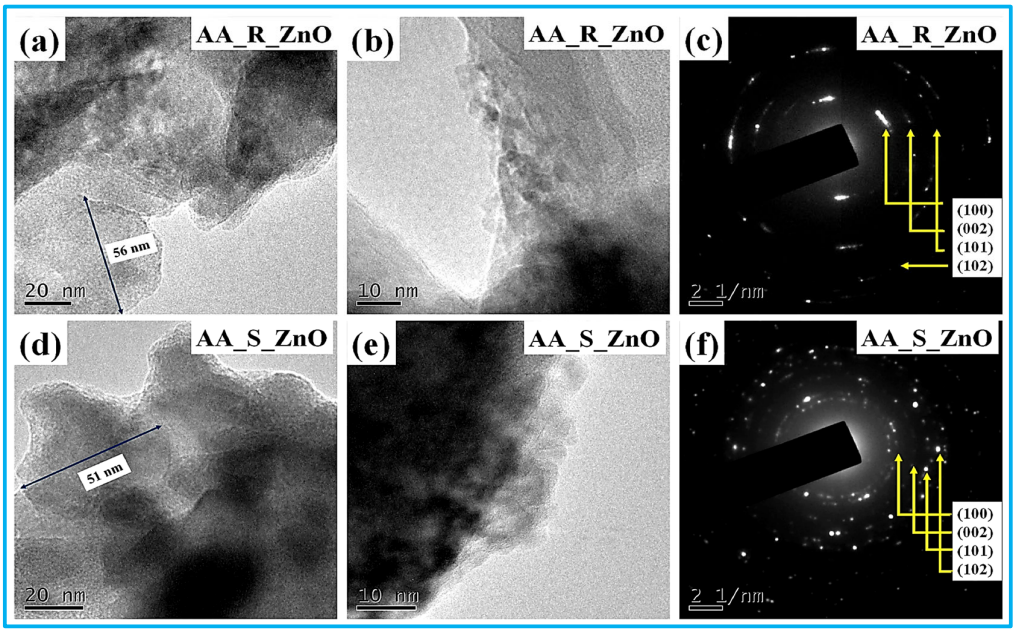


Figure 17. TEM morphology study of ZnO nanoparticles synthesized with Ambrosia ambrosioides extracts. (**a**,**b**) Morphology of AA_R_ZnO nanoparticles, (**c**) SAED of AA_R_ZnO, (**d**,**e**) Morphology of AA_S_ZnO nanoparticles, and (**f**) SAED of AA_S_ZnO [107].

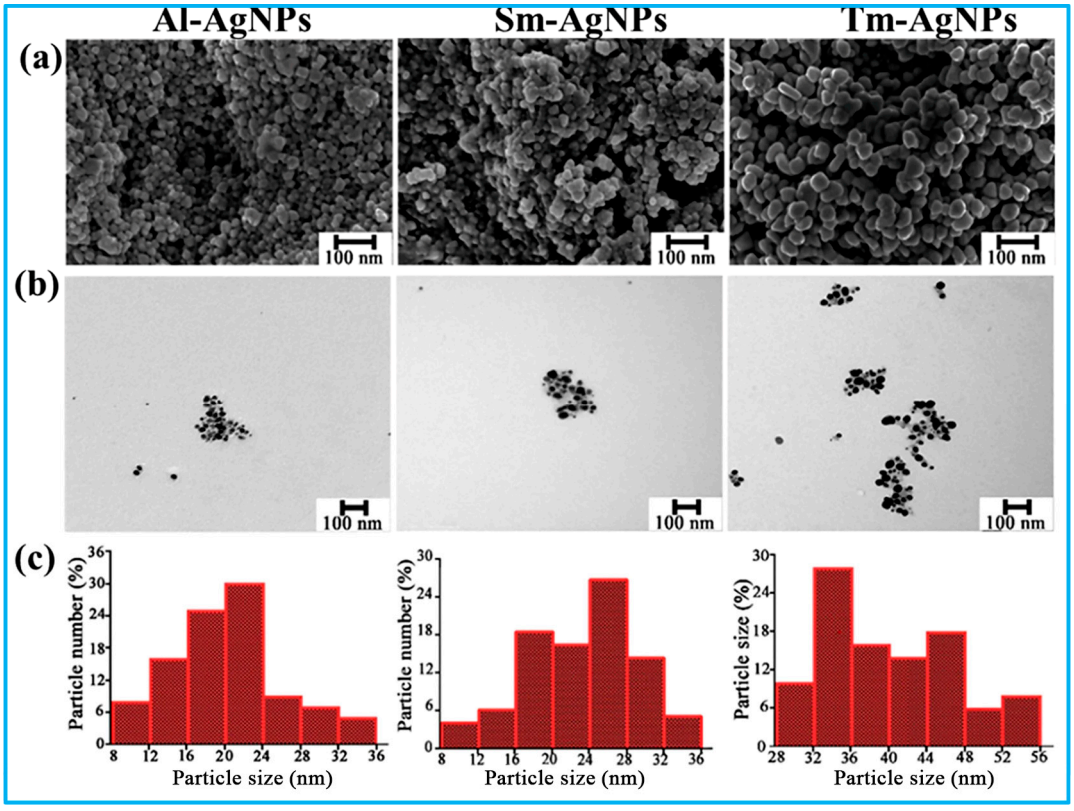


Figure 18. Morphology and size of Al-AgNPs, Sm-AgNPs, and Tm-AgNPs, scale bar = 100 nm. (**a**) SEM image (**b**) TEM image. (**c**) Size distribution of AgNPs [108].

Moreover, understanding optical properties and surface plasmon resonance is essential, which can be studied using UV-Vis spectroscopy.

4.4. Optical Properties

UV-Vis spectroscopy assesses optical properties, including absorption peaks associated with surface plasmon resonance, confirming nanoparticle formation and providing insights into size-dependent optical behavior. The UV-visible spectroscopy of barium oxide nanoparticles (BaONPs) was used to investigate their optical properties [109]. The UV-Vis absorption spectrum of BaONPs was observed over the wavelength range 200–800 nm. The BaONPs were generated using the *Spirogyra hyalina algal* extract as a reducing agent, with an absorption peak at 330 nm. This peak indicates the presence of green BaONPs nanoparticles. Rokkarukala et al. examined gold nanoparticles (AuNPs) using UV-visible spectroscopy, as provided in Figure 19 [110]. This technique provided a comprehensive analysis of the optical properties of AuNPs synthesized through an aqueous solution extracted from *Sarcophyton crassocaule*. The UV-visible absorption spectrum shows a surface plasmon resonance peak for the AuNPs at 540 nm (Figure 19a), which is attributed to their formation and confirms the successful synthesis. It was also supported by the color change from light yellow to dark purple upon adding the coral extract. No change in absorbance peaks was recorded as a function of time (Figure 19b), reflecting the stability of SCE-AuNPs formation without any aggregation.

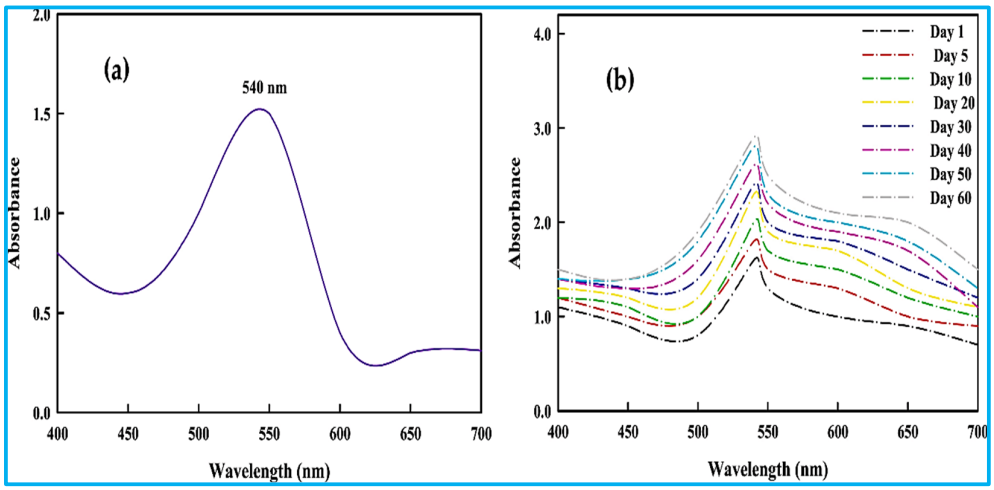


Figure 19. UV-visible spectra of (**a**) AuNPs, (**b**) stability peaks verified over time [110].

To confirm the formation and stability of green-synthesized niobium oxide (Nb_2O_5NPs) nanoparticles using *aloe vera* gel and niobium ethoxide, the optical properties of Nb_2O_5NPs were analyzed using UV-Vis spectroscopy at wavelengths ranging from 200 to 600 nm [111]. The resulting data showed an absorption spectrum extending beyond 400 nm, identified as that of Nb_2O_5NPs. The optical properties of ruthenium oxide nanoparticles (RuONPs) synthesized from an aqueous extract of *Gunnera perpensa* leaves as a reducing agent were investigated using UV-visible spectroscopy and are accessible in Figure 20. The UV-visible spectrum of RuONPs showed a prominent absorption peak at a wavelength of 413 nm, indicating the formation of green RuONPs [112].

Bharathidasan et al. used *Solanum xanthocarpum* to synthesize molybdenum nanoparticles (MoNPs) by green synthesis [113]. To investigate the stability and morphology of MoNPs, UV-visible spectroscopy was performed over a wavelength range of 200–1000 nm. The spectrum displays a prominent absorption peak at about 320 nm. The position of this peak demonstrates the effectiveness of *Solanum xanthocarpum* extract in synthesizing MoNPs. The preparation of indium oxide nanoparticles (In_2O_3NPs) was confirmed using UV-visible spectroscopy [114]. The In_2O_3NPs manufactured from the *Barbadensis miller* variety of *Aloe vera* exhibited prominent, sharp absorption peaks at 317 nm. These results

were consistent with the standard absorption spectrum of indium oxide (In_2O_3) NPs, reinforcing their formation and purity. It was found that the bandgap energy of In_2O_3NPs was approximately 3.26 eV.

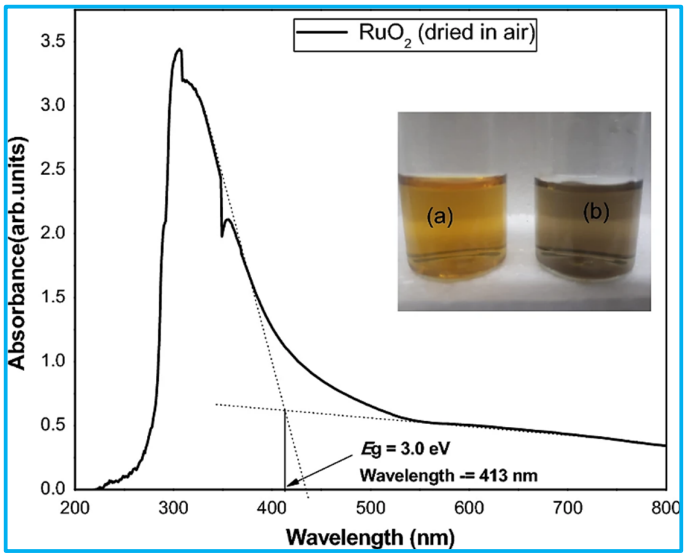


Figure 20. UV–visible spectrum of RuONPs (**a**) *Gunnera perpensa* extract (**b**) RuONPs [112].

Collectively, these techniques provide a comprehensive understanding of the structural, chemical, and functional characteristics of plant-derived nanoparticles, laying the foundations for their applications in medicine, catalysis, and environmental pollution control.

Moreover, evaluating the surface charge properties of plant-based nanoparticles is essential, as they strongly influence colloidal stability and interactions with charged pollutants. These characteristics are commonly determined through zeta-potential measurements and point-of-zero-charge (pHpzc) analysis.

4.5. Surface Charge Properties

The surface charge characteristics of plant-derived nanoparticles play a decisive role in determining adsorption selectivity, colloidal stability, and photocatalytic performance in aqueous environments. Surface charge is commonly evaluated through zeta potential (ζ) measurements and the point of zero charge (pHpzc), which defines the pH conditions at which nanoparticle surfaces shift from positively to negatively charged. These parameters strongly influence electrostatic interactions between the catalyst surface and ionic pollutants, as well as aggregation behavior under realistic ionic-strength conditions [115].

For many metal oxide nanoparticles synthesized through plant-mediated routes (e.g., ZnO, TiO_2, and Fe_2O_3), the reported pHpzc values typically fall within the 5 to 9 pH range. However, the exact pHpzc range depends on the composition of the precursors, the surface functionalization by phytochemicals, and the post-treatment conditions. When the solution pH is lower than the pHpzc, the nanoparticle surface generally acquires a positive charge, favoring the adsorption of anionic contaminants such as dyes or oxyanion species. Conversely, at pH values above the pHpzc, negatively charged surfaces promote interactions with cationic pollutants but may also increase electrostatic repulsion between particles, influencing dispersion stability and catalytic accessibility [116].

High absolute ζ-potential values ($|\zeta| \geq$ 25–30 mV) are generally associated with stable colloidal suspensions, whereas low ζ-potential values may lead to aggregation and reduced active surface area. In photocatalytic systems, stable dispersion enhances light exposure and pollutant–surface contact, thereby improving reaction kinetics. Experimental studies on plant-mediated ZnO and related nanomaterials have shown that variations in

surface charge across the pH range directly affect both dispersion stability and pollutant removal efficiency, demonstrating the importance of electrokinetic characterization in evaluating treatment performance [117].

In natural waters containing dissolved salts and organic matter, ionic strength can compress the electrical double layer, reducing electrostatic repulsion and facilitating aggregation. Consequently, adsorption capacity and photocatalytic activity measured under laboratory conditions may differ from those observed in real wastewater systems. Integrating systematic reporting of pHpzc values, ζ-potential ranges, and ionic-strength effects would therefore improve the comparability of studies and strengthen the interpretation of structure–property–performance relationships in plant-based nanomaterials for water purification [118].

5. Water Treatment Performance

Plant-based nanoparticles exhibit various chemical, physical, and biological properties, making them especially suitable for a wide range of applications, including environmental science research, particularly in contaminated water treatment.

5.1. Adsorption and Mechanism Processes

Contaminated waters are usually laden with a combination of polymeric, elemental, inorganic, and organic pollutants, posing a serious hazard to aquatic biodiversity, water quality, ecosystems, and soil fertility [119–121]. In the face of these considerable challenges, nanotechnology has emerged as a promising alternative, offering advanced catalytic processes to efficiently reduce water contamination, including membrane separation, oxidation, adsorption, coagulation-flocculation, and photocatalytic degradation [122–125]. Adsorption can be classified as one of the most efficient and cost-effective methods for treating toxic pollutants [126–128]. Generally, the type and nature of the adsorbent material influence adsorption efficiency. Nevertheless, characteristics such as reusability, large active surface area, sensitivity, selectivity, and stability are the principal properties selected for adsorbents.

Various research studies have documented the use of natural or processed bio-adsorbents to remove harmful pollutants [129,130]. Currently, plant-based nanoparticles are among the most celebrated materials for wastewater eradication due to their abundance, cost-effectiveness, regenerative properties, and eco-friendliness [131,132]. Table 2 presents the retention of pollutants using various plant-based nanoparticles, along with the corresponding optimum conditions and maximum adsorption capacities. Plant-based nanoparticles exhibit a higher adsorption capacity for pollutants than other commercial adsorbents.

Several plants were used to extract green nanoparticles for use as adsorbents, including *Nigella sativa*, *Muntingia calabura*, *Phyllanthus niruri*, *Justicia adhatoda*, *Punica granatum, Corn cobs*, and *Yali pears.* For example, Aynur Şahin et al. used *Codium macroalgae* to synthesize palladium (PdNPs), iron oxide (Fe_3O_4NPs), and platinum (PtNPs) nanoparticles. They used them for adsorbing cresol red (CR), methylene blue (MB), and naproxen (NPX) from real and synthetic wastewater [133]. The findings showed that the PdNPs have a high BET surface area of 99.613 m^2/g with small pore diameters of 3.10 nm, while the BET surface area and the pore sizes of Fe_3O_4NPs and PtNPs were, respectively, 6.356 m^2/g and 7.938 m^2/g with 3.87 nm. 25 mg L^{-1} of dye/drug was adsorbed using a 0.025 g dose of NPs at room temperature in 150 min. In real wastewater, PdNPs showed significant retention efficiencies of 50.03 mg g^{-1} for NPX and 37.19 mg/g for CR at pH 5. At the same time, the MB removal capacity was around 40.01 mg g^{-1} with PtNPs at pH 8. The Langmuir and pseudo-second-order models better described the retention processes of MB, NPX, and CR. In addition, a new hydrogel-bio-nanocomposite as a petroleum-based adsorbent was synthesized from carboxyl-functionalized carbon nanotubes and *Tragacanth gum* via

ultrasonication [134]. The adsorbent's surface area was measured at 8.3 m^2/g, and the pore diameter was 16.7 nm. A high-efficiency removal of 50 mg L^{-1} MB was observed using the linear Redlich-Peterson model, with an adsorption capacity of around 1092 mg g^{-1} in 40 min at pH 11 and 40 °C, suggesting a mixture of multi- and monolayer adsorption. In contrast, the pseudo-second-order model indicated that chemical adsorption was more dominant. The work of Almas Hamid et al. revealed the synthesis of palladium green nanoparticles (PdNPs) using *Lallemantia royleana* seeds as an adsorbent for tebuconazole (TBZ), chlorpyrifos (CP), and Congo red (CR) from an aqueous solution [135]. A hexagonal structure of PdNPs was observed, with pore sizes ranging from 15 to 61 nm. After 30 min, large retention capacities were observed, including 10.400 mg g^{-1} for CR, 16.745 mg g^{-1} for TBZ, and 14.633 mg/g for CP. Furthermore, magnetic nanoparticles derived from maize offal biomass (MOB/MNPs) were used to remove methyl orange (MO) and Congo red (CR) [136]. It was shown that the surface area and the pore volume of MOB/MNPs were 30.55 m^2/g and 89.4 nm, respectively. At pH 5, 2 g L^{-1} of MOB/MNPs eliminated 320 mg L^{-1} of MO and CR, with retention capacities of 29 and 114.75 mg g^{-1}, respectively. The three models of Elovich, Freundlich, and pseudo-second order well explained the elimination of MO and CR using MOB/MNPs. The retention processes of MO and CR were exothermic and spontaneous, with enhanced randomization.

Nevertheless, various plant parts were selected for the extraction of metal nanoparticles, including leaves, fruits, flowers, seeds, peels, barks, and roots [137,138]. Similarly, Manviri Rani et al. manufacture highly crystalline metal hexacyanoferrates (MHCFs) of Ni, Zn, Co, and Cu from *Sapindus mukorossi* seed extract [139]. The MHCFs were evaluated in an aqueous solution to eliminate tebuconazole (TEB), thiamethoxam (TH), and chlorpyrifos (CP). The specific surface areas were detected as approximately 72.55 m^2/g for CoHCF, 108.70 m^2/g for ZnHCF, 80.65 m^2/g for NiHCF, and 95.32 m^2/g for CuHCF, whereas the particle sizes of CuHCF and ZnHCF were approximately 100 nm. In contrast, the diameters of NiHCF and CoHCF were less than 10 nm. A high retention capacity was observed with 15 mg of MHCFs at neutral pH and 50 mg L^{-1} pesticide concentration after 12 h. Langmuir isotherm statistical data obtained using CoHCF, ZnHCF, NiHCF, and CuHCF indicated that the CP retentions were 123.76, 189.03, 125, and 130.38 mg/g, respectively, while the TH removal capacities were 104.60, 111.98, 105.26, and 106.61 mg/g, respectively. In contrast, TEB equilibrium capacities were 85.91, 104.16, 86.21, and 101, respectively. The pesticide elimination performance of ZnHCF was higher than that of the other adsorbents, owing to its higher BET surface area and zeta potential. Following Han Jiang et al., *Ocimum sanctum* (*tulsi*) leaves were used to synthesize cobalt nanoparticles. These nanoparticles were evaluated for their ability to remove methyl orange from an aqueous solution [140]. The average size of the Co nanoparticle crystals was 0.110 μm. In 5 h, 25 μg mL^{-1} of MO was eliminated by 125 μg mL^{-1} of Co nanoparticles at 70 °C in an acid solution (pH 2), yielding 71% elimination. Therefore, copper oxide nanoparticles (CuONPs) were prepared from *Nyctanthes arbortristis* flowers via green synthesis [141]. The removal of Cd (II), Cr (VI), Pb (II), and U (VI) ions was affected using CuONPs from an aqueous solution. The CuONPs were approximately 11.6 nm in size. The retention capacities of Cd (II), Cr (VI), Pb (II), and U (VI) using CuONPs were 90.90, 131.57, 155.27, and 200 mg/g, respectively. These capacities were detected using 10 mg of CuONPs in 120 min with an initial concentration of Cd (II), Cr (VI), Pb (II), and U (VI) of 50 mg L^{-1} at room temperature, while the removal pH of Cr (VI) and Cu (VI) ions was 4 and 6 for Cd (VI) and Pb (II) ions. According to the findings, the two pseudo-second-order and Langmuir models were better suited to the removal of Cd (II), Cr (VI), Pb (II), and U (VI) ions by CuONPs.

The most widely used in the adsorption process are metal oxides such as Fe_2O_4, Ag_2O, ZnO, CeO_2, SiO_2, MnO_2, SnO_2, TiO_2, and Mn_2O_3 [142–144]. In the same manner,

the zinc oxide nanoparticles (g-ZnONPs) derived from *Artemisia wormwood* leaves were studied as adsorbents for the removal of Cr (VI) ions from an aqueous solution [145]. The experiment revealed that g-ZnONPs with a large BET surface of 52.5858 m^2/g and a pore size of 17 nm displayed more dynamic, delocalized surface states. According to Langmuir's model, 0.25 g L^{-1} of g-ZnONPs could adsorb 25 mg L^{-1} of Cr (VI) ions at pH 4, with a maximum capacity of 315.46 mg g^{-1} over 150 min. The retention process of Cr (VI) ions was endothermic and spontaneous, with a disorder at the solid-solution interface. The regeneration process revealed that g-ZnONPs could be reused at least 6 times with higher removal efficiency. In another study, MnO-ZnONPs and MnO-CuONPs binary nanoparticles were produced from *hemp* seeds for the removal of methylene blue (MB), ibuprofen (IBU), and lead (Pb (II)) [146]. MnO-ZnONPs and MnO-CuONPs have a low pore size of 0.0108 nm and 0.0195 nm, respectively, and the specific surface area was 24.79 m^2/g for MnO-ZnONPs and 21.55 m^2/g for MnO-CuONPs. Optimum conditions were achieved at 1440 min at pH 8 with 20 mg/L dosages of MnO-ZnONPs and MnO-CuONPs and a 100 mg L^{-1} pollutant concentration. The retention of MB, IBU, and Pb (II) was found to be multilayered, with heterogeneous MnO-ZnONPs and MnO-CuONPs surfaces, as indicated by the Freundlich model. MnO-CuONPs exhibited higher removal capacities of 68.95 mg g^{-1} for MB, 21.50 mg g^{-1} for IBU, and 66.58 mg g^{-1} for Pb (II). The kinetic investigation revealed two phases: the first, caused by the rapid removal of MB, IBU, and Pb (II); and the second, attributable to the saturation of the active sites, marked by a gradual increase in the retention rate. Therefore, increasing temperature reduces IBU's retention capacity and increases the removal efficiency of MB and Pb (II), indicating an exothermic reaction for IBU and endothermic reactions for MB and Pb (II). Research conducted by Aynur Şahin et al. synthesized iron oxide nanoparticles from *Prunus avium* stems using a green synthesis method to remove methylene blue from wastewater [42]. The particle size of iron oxide NPs was 91.28 nm. At natural pH, 30 mg L^{-1} of MB dye was removed by 0.3 g of iron oxide NP_3 in 150 min at 25 °C, yielding a high MB retention rate of 67.34%. The correlation coefficient indicated that the Freundlich model provided a better fit to the removal process. This indicated that the iron oxide NP_3 surface was heterogeneous, with a monolayer and a multilayer retention mixture. The paper by Malarvizhi et al. investigated the feasibility of eliminating the crystal violet (CV) and methylene blue dyes using zinc oxide nanoparticles (EF-ZnONPs) [147]. These nanoparticles were recovered from the leaves of *Dracaena trifasciata* (snake plant) using the ecological co-precipitation method. The surface area of EF-ZnONPs was 37 m^2/g, while the average pore diameter was 17.74 nm. The optimum conditions indicated retention percentages of 88% for CV and 86% for MB after 50 min in a basic medium (pH = 10), using 0.06 g of EF-ZnONPs, with initial CV and MB concentrations of 50 mg/L at 40 °C. The Freundlich model best described the removal of CV by EF-ZnONPs, whereas the elimination of MB using EF-ZnONPs followed the Temkin model, with high retention capacities of 84.75 and 144.93 mg g^{-1}, respectively. The Elovich model was more consistent with the CV removal using EF-ZnONPs, and the pseudo-first-order model can trace the retention of MB using EF-ZnONPs.

The specific surface area is not the only factor influencing pollutant retention capacity; the contaminant-binding mechanism and adsorbent stability also significantly affect removal efficiency. Furthermore, pH influences surface properties and the density of active sites, both of which are critical for pollutant removal. For instance, in TiO_2NPs, the preparation pH determines the point of zero charge and the density of surface hydroxyl groups, thereby affecting electrostatic interactions with charged pollutants, which, in turn, modulate interactions with adsorbates and adsorbents. Iron oxide nanoparticles (FeONPs) synthesized from *Moringa oleifera* leaf extract were evaluated for fluoride ion removal from aqueous solution [148]. It was reported that 6 mg L^{-1} of fluoride ions were retained at pH 7

within 40 min using 0.5 g L^{-1} of FeONPs at 30 °C. A low fluoride ion retention of around 1.40 mg g^{-1} was detected despite a high specific surface area of 99.79 m^2/g and a small diameter size of 0.08 nm. The fluoride ion removal process was spontaneous, endothermic, and monolayer, and the FeONPs surface was homogeneous. The regeneration findings indicated that FeONPs can be reused three times with stable fluoride-ion elimination capacity. In addition, the retention of As(V) ions via *Vaccinium corymbosum*-based iron nanoparticles from an aqueous solution was investigated by Manquián-Cerda et al. [149]. Green synthesis was used to prepare iron nanoparticles derived from *blueberry* leaf and shoot extracts (BB-FeNPs). Although the specific surface area (70.7 m^2/g) and average size (52.4 nm) of BB-FeNPs were high, their removal capacity of 200 mg L^{-1} of As(V) ions was slightly lower at 50.40 mg g^{-1} and slower (120 min) in an acid solution (pH = 4) using 50 mg of BB-FeNPs. The experimental results demonstrate that both the Langmuir-Freundlich and pseudo-second-order models were in excellent accord with the retention process of As(V) ions. The iron nanoparticles have a high affinity for As(V) ions, and active sites predominate on the surface of BB-FeNPs, including Fe-O-OH and Fe-OH.

The functional groups of the adsorbents identify the nature of the retention mechanism. In contrast, when the number of adsorbent functional groups was higher, interactions between the pollutants and the adsorbent were stronger, allowing pollutants to be fixed in different positions. Figure 21 shows the proposed mechanisms for removing organic and inorganic contaminants using plant-based NPs.

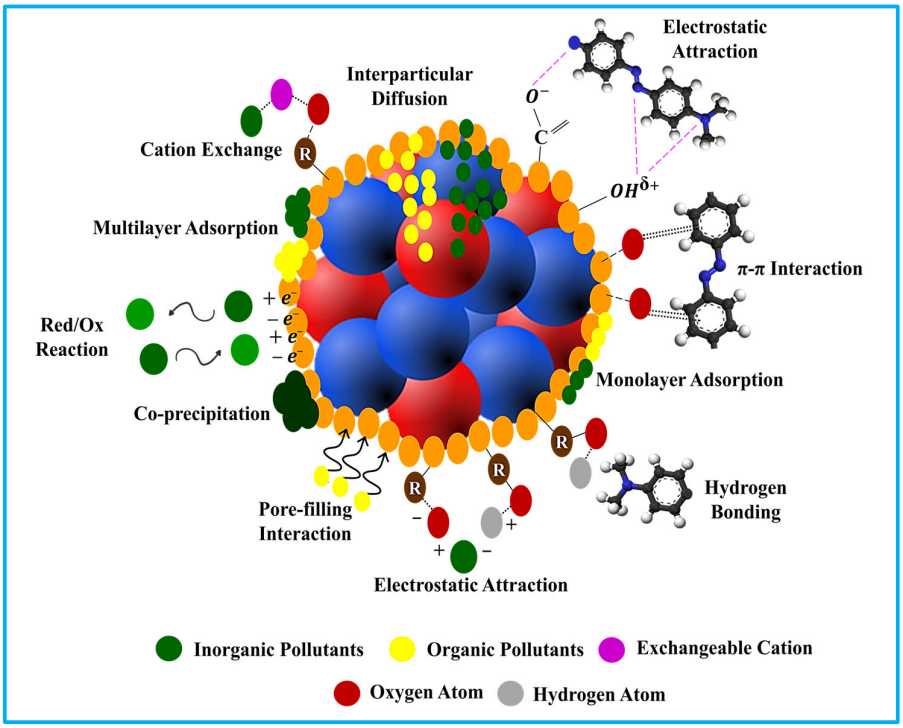


Figure 21. Removal mechanisms suggested for the retention of organic and inorganic pollutants by plant-based NPs.

Table 2. Retention of heavy metals, dyes, antibiotics, pesticides, herbicides, and other pollutants using plant-based metal oxide nanoparticles.

Pollutant Type	Pollutant Example	Plant	NPs	S_{BET} (m^2/g)	V_{Pore} (cm^3/g)	Size (nm)	Optimal Conditions				Q_{max} (mg g^{-1})	Ref.
							Time (min)	Dose (g L^{-1})	pH	C_i (mg L^{-1})		
Dyes	Methylene blue	*Olive tree*	NiO	-	-	42	100	6	10	25	38.46	[150]
	Methyl orange						160	6	2	20	6.91	
	Congo Red	*Lemon leaf*	ZnO-$CdWO_4$	-	-	40	60	2	7	20	5	[151]
	Methylene blue	*Psidium guajava*	Fe_2O_3	-	-	52	90	1	7	10	69.63	[152]
	Malachite green	*Costus woodsonii*	Mn_3O_4	-	-	-	20	0.5	5	100	162	[153]
	Congo Red	*Muntingia calabura*	Hydroxyapatite	-	-	-	137	0.5	7	33.18	217.39	[154]
	Methyl orange	*Phyllanthus niruri*	TiO_2	-	-	20	40	0.02	7	10	273.37	[155]
	Crystal violet	*Fig leaves*	Fe_3O_4	-	-	-	25	0.05	8	4	53.47	[156]
		Azolla					25	0.03	8	3	30.21	
	Congo Red	*Prunus armeniaca* L.	Se	-	-	9.96	200	0.16	7	180	96.59	[157]
	Acid blue 113	*Thunbergia grandiflora*	Fe_3O_4	114.42	0.23	8.18	210	1	2	25	138.89	[158]
	Reactive Blue 19	*Nymphaeaceae fronds*	ZnO	-	-	-	60	0.02	5	50	219.6	[159]
	Reactive Orange 16						60	0.03	4	50	129.6	
	Congo Red						60	0.03	4	50	118.8	
Antibiotics	Amoxicillin	*Oenothera biennis*	Ag	-	-	8.10	30	0.5	4	30	101.01	[160]
	Tetracycline hydrochloride	*Justicia adhatoda*	Fe_2O_3	-	-	6.4	30	0.01	4	400	200	[161]
	Ciprofloxacin	*Stevia rebaudiana*	ZnO	15.28	0.095	30.13	120	4	5	10	27.07	[162]
	Tetracycline						120	4	5	25	15.88	
Pesticides and Herbicides	Ametryn	*Black tea*	Fe_2O_3	-	-	-	30	2.5	7	30	14.29	[163]
	Chlorpyrifos	*Sapindus mukorossi*	Co	72.55	-	<10	12 h	0.015	7	50	123.76	[139]
	Thiamethoxam										104.60	
	Tebuconazole										85.91	

Table 2. *Cont.*

Pollutant Type	Pollutant Example	Plant	NPs	S_{BET} (m^2/g)	V_{Pore} (cm^3/g)	Size (nm)	Optimal Conditions				Q_{max} (mg g^{-1})	Ref.
							Time (min)	Dose (g L^{-1})	pH	C_i (mg L^{-1})		
Pesticides and Herbicides	Chlorpyrifos	*Sapindus mukorossi*	Ni	80.65	-	<10	12 h	0.015	7	50	125	[139]
	Thiamethoxam										105.26	
	Tebuconazole										86.21	
	Fenpropathrin	*Crossa leaves*	MgO	-	-	35.12	120	1.0	7	50	32.18	[164]
	Bromoxynil	*Mentha piperita leaves*	Zero-valent iron	-	-	10	25	0.4	7	-	200	[165]
	Paraquat						18	0.3	7	-	180	
	Glyphosate	*Pomegranate Eucalyptus Pecan leaves*	Fe_3O_4	94. 20	0.497	20.54	120	1.5	4	35	21.17	[166]
Heavy metals	Cr (VI)	*Heterophragma adenophylla*	Ag	-	-	21.81	60	0.8	4	25	4	[167]
		Syzygium cumini		-	-	4.6	40	0.8	6	25	8.55	
	Mn (II)	*Palm pruning*	Fe_3O_4	-	-	50	60	-	7	-	159	[168]
	Co (II)						60	-	7	-	153	
	Pb (II)						60	-	7	-	197	
	As (V)	*Camellia sinensis*	Fe_3O_4	18.33	-	70	48 h	1	6	10	18.98	[169]
		Quercus virginiana		23.12	-	100	48 h	1	6	10	32.05	
		C. sinensis		3.26	-	40	48 h	1	6	10	13.7	
		Punica granatum		0.83	-	80	48 h	1	6	10	11.65	
		Eucalyptus globulus		22.57	-	50	48 h	1	6	10	39.84	
	U (VI)	*Carica papaya*	Fe_3O_4	-	-	26.4	40	0.1	7	150	120.48	[170]
	Hg (II)	*Ficus Panda*	SnO_2	-	-	-	45	1	5	50	10	[171]
	Cd (II)						60	1.5	5	35	12.8	
	Hg (II)	*Wheat straw*	Fe_3O_4	-	-	22.48	45	1	6	40	101.1	[172]

Table 2. *Cont.*

Pollutant Type	Pollutant Example	Plant	NPs	S_{BET} (m^2/g)	V_{Pore} (cm^3/g)	Size (nm)	Optimal Conditions				Q_{max} ($mg\ g^{-1}$)	Ref.
							Time (min)	Dose ($g\ L^{-1}$)	pH	C_i ($mg\ L^{-1}$)		
Heavy metals	V (V)	*Yali pear peel*	Fe	-	-	<100	20	0.4	3.7	90	362.7	[173]
	U (VI)	*Citrus limon*	CeO_2	-	-	-	40	0.003	4	0.1	46.2	[174]
Others	Phosphate	*Eucalyptus*	Fe_3O_4	-	-	80	45	1	2	60	18.69	[175]
	Fluoride	*Moringa oleífera*	FeO	99.79	4.14	0.08	40	0.5	7	6	1.40	[148]
	Phosphate	*Parthenium*	Fe_3O_4	-	-	60	240	2	6	5	15.69	[176]
	Phosphorus	*Pistachio green*	FeO	-	-	40	120	2.5	5	5	29.33	[177]
		Shirazi thyme		-	-	40	240	2.5	5	5	40.52	
	Phosphate	*Eucalyptus*	Fe_3O_4	-	-	60	15	1	7	10	38.91	[178]
	Ammonia						15	1	7	10	3.47	
	Phosphorus	*Green tea*	FeO	-	-	20	24 h	2.5	7.5	300	53.47	[179]
		Walnut green		-	-	20	24 h	2.5	8.1	300	45.82	

In summary, the adsorption of organic and inorganic compounds by nanoparticles depends on the nature of the surfaces of the adsorbent and the adsorbate. It mainly involves surface precipitation and coprecipitation, ligand exchange, diffusion-controlled reactions, redox reactions, cation exchange, π–π interactions, hydrogen bonding, electrostatic attraction, and inner sphere complexation [180–183].

A research study by Aklima A. Akhi et al. reported the removal of MB by *Ophiorrhiza mungos* leaves-based silver nanoparticles (Om-AgNPs) [184]. The pore size of Om-AgNPs was 17 nm with a low specific surface area of 4.39 m^2/g. A high retention capacity of 80.451 mg g^{-1} was observed despite the low specific surface area for Om-AgNPs at pH 7.4, in 60 min, with an initial MB concentration of 10 mg L^{-1}, using 0.6 g L^{-1} of Om-AgNPs at 25 °C. The removal of MB by Om-AgNPs was better described by the Langmuir and pseudo-second-order models, indicating monolayer and chemical adsorption, respectively. It was found that MB retention by Om-AgNPs can involve multiple mechanisms, including hydrogen bonding, π-π stacking, and electrostatic interactions. The CO and OH groups present on the surface of Om-AgNPs can react with MB and adsorb through hydrogen bonds between the hydroxyl groups of Om-AgNPs and the sulfur and nitrogen atoms of MB. The aromatic rings of the biomolecules surrounding Om-AgNPs and MB may confirm the presence of a π-π stacking mechanism. The electrostatic interaction mechanism between MB and functional groups on the surface of Om-AgNPs, including OH, C=C, and C=O groups, was investigated. Moreover, Aquib Jawed et al. proposed the synthesis of iron oxide nanoparticles (IONPs) from extracts of *Camellia sinensis* var. *Assamica* tea leaves, focusing on their performance in removing Cr (VI) ions from contaminated water [185]. The specific surface area and pore diameter of IONPs were 18.27 m^2/g and 37 nm, respectively. A 96% removal rate of Cr (VI) (40 mg L^{-1}) was attained at 25 °C in 48 min by dosing 0.75 g L^{-1} of IONPs at pH = 2. The pseudo-second-order model exhibits exothermic retention of Cr (VI) ions, while the Langmuir model provides a significant removal capacity of 1272 mg g^{-1}. According to the results, the Cr (VI) ions interacted with the active sites on the IONPs' surface, while some Cr (VI) ions were reduced to Cr (III), which liberated Fe^{2+}/Fe^{3+} ions. Simultaneously, the oxidation of Fe^{2+} to Fe^{3+} and Fe^0 to Fe^{2+} and the conversion of Cr (III) to Cr (VI) occurred. An increase in pH leads to precipitation of Cr (III) in the form of $Cr(OH)_3$ and co-precipitation of $Cr_xFe_{1-x}(OH)_3$ $x(OH)_3$ in the presence of Fe(III). These results are consistent with those obtained in the study conducted by Yu et al. [186].

The iron nanoparticles sustained via corn straw biochar (PE-FeNPs@BC) were applied to remove V(V) [173]. PE-FeNPs@BC was synthesized from corn straw biochar as a support, and iron nanoparticles extracted from *Yali pear* peel were employed as a functional body. The pore diameter of PE-FeNPs@BC was lower than 100 nm. The Langmuir model indicates that 90 mg L^{-1} V(V) was adsorbed by 0.4 g L^{-1} PE-FeNPs@BC at pH 3.7, with a retention capacity of 362.7 mg g^{-1} at 25 °C over 120 min. The pseudo-second-order model provided the best fit for the removal process, indicating that chemical retention was the dominant mechanism. The electrostatic retention and reduction reactions were the main interactions between PE-FeNPs@BC and V(V) ions. According to the findings, the mechanism of vanadium (V) removal using PE-FeNPs@BC was performed following three steps: (a) V(V) ions were adsorbed on the surface of PE-FeNPs@BC via electrostatic interactions, (b) the reduction of V^{5+} ($H_2VO_4^-$) to V^{4+} (VO^{2+}) and the oxidation of Fe^{2+} and Fe^0 in PE-FeNPs@BC to Fe^{3+}, as shown in Formulae (1) and (2), and (c) the combination and co-precipitation of $H_2VO_4^-$ and Fe^{3+} creating the $xFe_2O_3 \cdot yV_2O_5 \cdot zH_2O$ precipitate following Formula (3). Thus, Formula (4) illustrates that VO^{2+} interacted with OH- to make

the VO_2H_2O precipitate and was adsorbed onto the PE-FeNPs@BC surface, owing to the increase in pH and the consumption of H^+.

$$Fe^0 + H_2VO_4^- + 6H^+ \rightarrow Fe^{3+} + VO^{2+} + 4H_2O \quad (1)$$

$$Fe^{2+} + H_2VO_4^- + 4H^+ \rightarrow Fe^{3+} + VO^{2+} + 3H_2O \quad (2)$$

$$2xFe^{3+} + 2yH_2VO_4^- + 6xOH^- \rightarrow xFe_2O_3.yV_2O_5.zH_2O\ (s) \quad (3)$$

$$VO^{2+} + 2OH^- \rightarrow VO_2.H_2O\ (s) \quad (4)$$

Plant-based nanoparticles exhibit enhanced adsorption performance mainly due to their rich surface chemistry derived from phytochemicals such as polyphenols, flavonoids, terpenoids, and organic acids. These biomolecules introduce abundant functional groups (–OH, –COOH, $–NH_2$) on the nanoparticle surface, which promote strong interactions with pollutants through hydrogen bonding, electrostatic attraction, and surface complexation [187,188]. In addition, the typically small particle size and irregular morphology increase the effective surface area and availability of active sites. Consequently, plant-based nanoparticles can efficiently capture and concentrate contaminants from aqueous media, thereby improving adsorption capacity and selectivity.

Photodegradation of Dyes

The extensive use of organic dyes across sectors such as clothing, papermaking, leather, food, and cosmetics generates substantial amounts of wastewater contaminated with dyes. These organic pollutants are often highly resistant, water-soluble, and non-biodegradable, posing grave environmental and human health hazards [189]. Moreover, their presence in water can cause numerous problems, including unattractive coloration, increased biochemical oxygen requirement, and toxicity, threatening aquatic life [190]. Not only that, they can persist in the environment for long periods, accumulate in the food chain, and pose a potential threat to human health [191]. The traditional treatment approaches mentioned above frequently fail to remove these complex aromatic compounds. This is why there is growing interest in alternative techniques, such as photocatalytic degradation, which offer more effective and sustainable solutions for dye removal [192]. Metal nanoparticles have proved highly effective for this application due to their large surface area and high catalytic activity. Recently, nanoparticles derived from plant extracts have emerged as a promising, environmentally friendly approach to dye photodegradation, offering a potential solution to the environmental challenges posed by dye-contaminated wastewater [193].

Several related studies have been undertaken on the removal of the methylene blue dye using plant-based metal oxide nanoparticle photocatalysts. For example, H. Ali et al. developed cerium nanoparticles (CeO_2NPs) via a green method using *Spirulina platensis* (Sp) extract as a stabilizing agent. They applied them as photocatalysts for the removal of methylene blue dye. Characterization results showed that the green CeO_2NPs had a stable crystal structure with well-defined morphological properties and exhibited bandgap energies of 3.15 eV for CeO_2@Sp (2:1) and 2.94 eV for CeO_2@Sp (1:1), lower than those of pure CeO_2 (3.3 eV). Furthermore, the CeO_2@Sp (1:1) nanocomposite achieved a high MB dye photodegradation efficiency of 88.8% compared with pure CeO_2 (76.4%) at pH 11, contact time of 90 min, catalyst dose of 0.3 g L^{-1}, and initial MB dye concentration of 100 mg L^{-1}. Meanwhile, MB dye degradation by ceria NPs was well fitted with the pseudo-second-order kinetic model [194]. In another study, Selvi et al. adopted the same approach to synthesize niobium (Nb_2O_5) nanoparticles from *Brassica oleracea* leaf extract. The eco-friendly Nb_2O_5 NPs exhibited a spherical morphology, an average particle size

of 9 nm, and a bandgap energy of 3.2 eV. After 80 min of UV exposure, the resulting nanoparticles completely degraded the MB dye. It is important to note that the large number of active surface sites on the novel Nb_2O_5 nanospheres enables them to exhibit excellent photocatalytic activity [195].

Similarly, several studies have used this type of catalyst to photodegrade the Rhodamine B dye. Barrios-Navarro et al. reported the synthesis of CuO, Bi_2O_3, and CuO/Bi_2O_3 nanocomposites using a natural *bamboo* leaf extract. Using the dye Rhodamine B (RhB) as a model organic pollutant, the photocatalytic performance of the CuO/Bi_2O_3 nanocomposite was the best, as a dosage of 35 mg was able to degrade 95.6% of RhB at a concentration of 10 mg L^{-1} compared to the catalysts CuO (40.2%) and Bi_2O_3 (80.5%) in 180 min under UV irradiation with good reusability. The enhanced photocatalytic property of CuO/Bi_2O_3 NPs (2.4 eV) in degrading RhB dye under optimal conditions results from the good coupling of CuO (2.1 eV) with Bi_2O_3 (2.9 eV) nanoparticles [196]. Likewise, Prescilio et al. have investigated the use of two types of nanocomposites from magnetic-iron oxide and zinc oxide, one pure FeOx@ZnO (FZ) and the other doped with nickel, FeOx@ZnO-Ni (FZNi), biosynthesized using *Magonia pubescens* extracts, for the removal of the aqueous RhB dye. Theoretical results, consistent with experimental results, revealed that partial nickel doping and the presence of its nanoparticles on the material surface effectively reduced the bandgap of the FZNi nanocomposite, which reached a smaller value (2.46 eV) compared to FZ (3.17 eV), increasing its absorption of visible light, which improved its performance in degrading RhB dye with a very high efficiency of 96.8% after 300 min under light irradiation [197].

Related work also examines the efficiency of green nanocomposites in degrading the methyl orange dye under illumination. In a study conducted by Bayahia, an aqueous medium of *Schinus molle* leaf extract was used to prepare a new monoclinic $FeNbO_4$ semiconductor nanocomposite ($FeNbO_4$-HT + *S. molle*) via the hydrothermal method, intended for use as a photocatalyst for methyl orange dye elimination. The $FeNbO_4$-HT + *S. molle* nanocatalyst was found to have the smallest nanoparticles (22.8 nm) with the lowest bandgap energy (2.78 eV) and a consistent morphology that resulted in its photocatalytic activity exhibiting superior light absorption and photostability, which enhanced its performance in degrading 96% MO (10 mg L^{-1}) under visible light for 50 min [198]. In addition, Arif et al. used a green stabilizing agent derived from *Acacia nilotica* (*Kiker*) leaf extract to synthesize niobium-doped iron oxide nanoparticles (Nb-doped Fe_2O_3NPs) as catalysts that exhibited efficient photocatalytic activity in the degradation of the MO dye. Increasing the niobium doping ratio in green iron oxide nanoparticles reduced the band gap to 1.45 eV upon adding 15% Nb, thereby enhancing light absorption and improving their photocatalytic activity [199].

Applications of green semiconducting nanoparticles in photodegradation have also targeted other types of dyes as organic pollutants. For instance, Safitri and Yulizar have successfully applied an ecologically bio-based approach using *Citrus limon* (L.) Osbeck leaf extract in developing $ZnFe_2O_4$-decorated Y_2O_3 nanocomposites for use as photocatalysts in the decomposition of the malachite green (MG) dye. The $ZnFe_2O_4/Y_2O_3$ composite showed the best photocatalytic efficiency in degrading MG dye (95%) in 120 min compared with pure $ZnFe_2O_4$ and Y_2O_3. This enhanced photocatalytic performance of $ZnFe_2O_4/Y_2O_3$ was attributable to its unique morphology, with a nanoparticle size of 49.61 nm and a narrow band gap of 2.08 eV [200]. In another work, Hasan et al. tested the potential of biosynthesized $Ag@Fe_3O_4$ nanocomposites using an aqueous extract of *Laurus nobilis* leaves to treat dye-contaminated water. Their findings demonstrated enhanced photocatalytic elimination of rose bengal (RB), methylene blue (MB), and toluidine blue (TB) dyes within 120 min under solar illumination, with good regeneration and recyclability [201].

5.2. Photodegradation and Mechanism Processes

For water treatment, photocatalytic degradation using plant-based NPs as catalysts has attracted considerable attention as one of the most promising approaches, unlike other techniques such as adsorption, membrane separation, etc. [138,202]. As mentioned above, this type of NPs is prepared by a facile, eco-friendly, and economical method and does not require harmful reactants. They are produced in a manner similar to conventional photocatalysts, using plant extracts and a variety of natural phytochemicals, such as flavonoids, steroids, and phenolics [203]. These composites are recognized as stabilizing, capping, and reducing agents and play an essential role in lowering ions of diverse metals to metallic oxide photocatalysts [204]. The potential of these modern plant-based nanoparticle catalysts in the environmental field, particularly in photocatalytic applications, is considerable due to their many beneficial properties, including enhanced surface area and high density of catalytically active sites, which make them effective in removing aquatic organic pollutants via adsorption, degradation, and reduction pathways [205,206].

Plant-mediated metal and metal oxide nanoparticles have emerged as promising semiconductor photocatalysts for the degradation of aquatic organic pollutants, including synthetic dyes, pharmaceutical residues, and agrochemicals, under ultraviolet or solar irradiation [207–210]. Upon light absorption with energy equal to or exceeding the bandgap, electrons are excited from the valence band to the conduction band, generating electron–hole (e^-/h^+) pairs. While this initial photoexcitation step is common to semiconductor photocatalysis, the subsequent charge-transfer and oxidative pathways are highly dependent on the catalyst composition, surface chemistry imparted by phytochemicals, and reaction conditions [211,212].

In aqueous systems, photogenerated holes may oxidize surface-adsorbed water molecules or hydroxide ions to yield hydroxyl radicals (•OH), whereas conduction-band electrons can reduce dissolved oxygen to superoxide radicals ($O_2\bullet^-$) [209,213]. In several studies involving green-synthesized ZnO, TiO_2, Fe_2O_3, and CuO nanoparticles, the involvement of •OH and $\bullet O_2^-$ has been directly supported by radical-scavenger experiments. The suppression of photocatalytic activity in the presence of tert-butanol, isopropanol, or benzoquinone provides strong evidence for the participation of hydroxyl and superoxide radicals, respectively [208,210,214–216]. In a limited number of reports, electron spin resonance (ESR) spectroscopy has further confirmed the formation of these reactive species under illumination, strengthening mechanistic conclusions [215,217].

However, in many plant-based photocatalytic systems, ROS participation is inferred indirectly rather than directly measured. Enhanced degradation efficiencies, reduced bandgap energies, or improved light absorption are often interpreted as indicators of effective ROS generation, although such observations alone do not constitute definitive proof [211,218]. Consequently, ROS pathways proposed in these cases should be regarded as hypothesized mechanisms, inferred from band-structure considerations and photocatalytic performance trends.

Secondary reactions may also contribute to pollutant degradation. Superoxide radicals can undergo proton-assisted reactions to form hydrogen peroxide (H_2O_2), which may subsequently decompose into additional hydroxyl radicals under irradiation [213,219]. These reactive oxygen species initiate oxidative attacks on chromophoric groups, aromatic rings, and heteroatom-containing moieties within organic pollutants, leading to molecular fragmentation and, in favorable cases, partial mineralization [207,220]. A generalized schematic representation of charge excitation, ROS generation, and pollutant oxidation is presented in Figure 22.

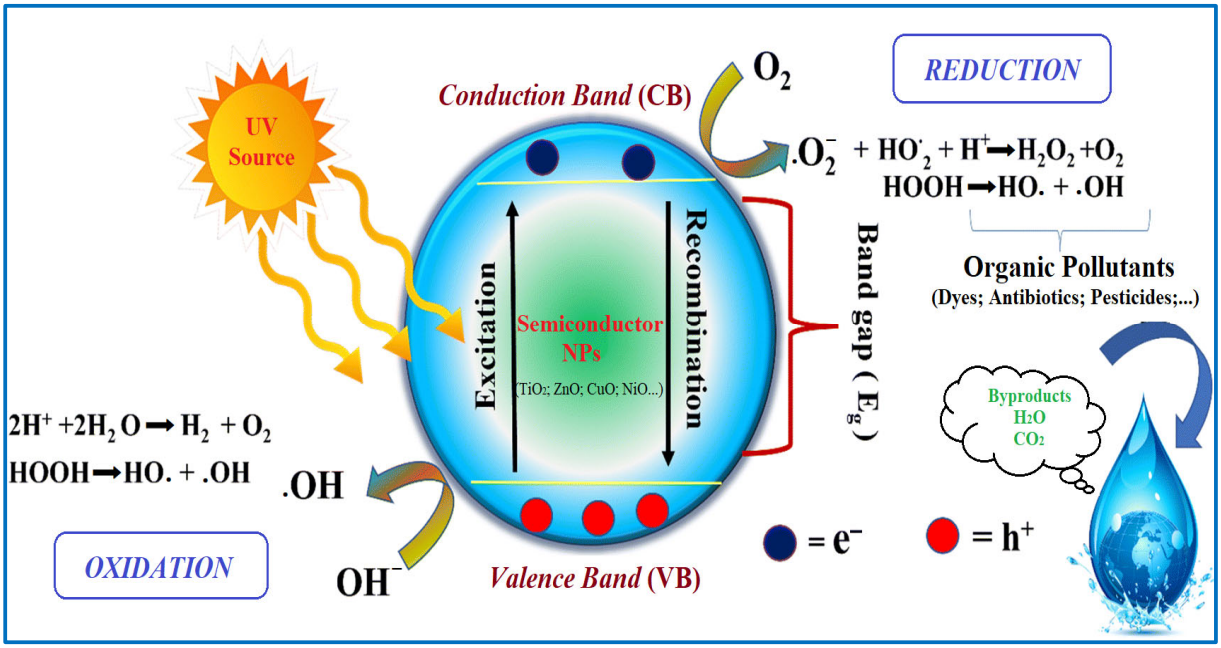


Figure 22. A comprehensive description of the photocatalysis mechanism using semiconducting nanoparticles.

Material modification strategies further illustrate the system-specific nature of ROS pathways. Yu et al. combined density functional theory (DFT) calculations with experimental electrochemical analyses to demonstrate that Ce doping in Fe_2O_3 modifies electron density distribution, enhances charge separation, and promotes the formation of reactive species in electro-Fenton systems [186]. Similar synergistic effects have been reported for plant-derived doped-metal oxides, where surface-bound phytochemicals influence nucleation, defect density, and charge-carrier lifetimes [212,221]. Nevertheless, such findings are catalyst-specific and should not be generalized across all plant-mediated nanoparticle systems.

Overall, hydroxyl and superoxide radicals are the most frequently implicated oxidative species in plant-based photocatalysis when supported by scavenger or spectroscopic evidence. In contrast, the relative contribution of H_2O_2-derived pathways, singlet oxygen, or direct hole oxidation remains uncertain in many systems due to limited experimental verification. Future studies integrating standardized scavenger protocols, ESR spectroscopy, band-edge position analysis, and oxygen-controlled experiments are essential to distinguish dominant ROS pathways and to strengthen structure–property–performance relationships in green photocatalytic materials.

Advanced scientific investigations have been conducted into the photocatalytic degradation of various organic pollutants, including dyes, pharmaceuticals, pesticides, and other compounds. Furthermore, thanks to a "green" approach, a selection of renewable, durable products has been used to produce effective photocatalytic nanoparticles, which are discussed in the following sections.

5.2.1. Photodegradation of Pharmaceuticals

The widespread presence of pharmaceutical residues in aquatic environments has emerged as a serious environmental and public health concern [222]. These compounds, including antibiotics, anti-inflammatory drugs, and analgesics, are often incompletely metabolized in the human or animal body and are released into the environment through wastewater, hospital discharge, and improper disposal. Their continuous presence in water bodies poses serious risks to ecosystems and human health, including disrupting aquatic life and promoting the spread of drug-resistant bacteria [223]. In recent years,

increasing attention has been directed toward removing these contaminants through advanced oxidation processes (AOPs), particularly photocatalysis. Among the innovative green photocatalytic materials, plant-based nanoparticles have gained interest due to their eco-friendly synthesis, cost-effectiveness, and high efficiency in generating reactive oxygen species like hydroxyl (•OH) and superoxide ($\bullet O_2^-$) radicals under light irradiation [224]. These reactive species can break down complex pharmaceutical molecules into less harmful byproducts. This subsection explores the application of plant-derived nanoparticles in the photocatalytic degradation of pharmaceutical pollutants, highlighting their potential as sustainable alternatives in water treatment technologies.

In the case of Gizachew et al., it was reported that green Ag/Fe/ZnO nanocomposites prepared using an aqueous extract of *Embelia schimperi* leaves were applied as a photocatalyst for the degradation of amoxicillin (AMX), an antibiotic. This natural extract significantly enhanced the photocatalytic performance of the Ag-Fe-ZnO nanoproduct, thereby reducing the number of active sites available for oxidizing amoxicillin molecules. After 180 min under visible light in the presence of the Ag-Fe-ZnO composite, 98.5% of the AMX was eliminated [225]. Rana et al. also studied the photodegradation of amoxicillin using ecological zinc oxide nanoparticles (ZnONPs) doped with transition-metal catalysts (Fe, Ni, and Co), prepared by a green method from an *orange* peel extract. It was found that Ni-doped ZnONPs exhibited the highest AMX degradation rates under UV (80.71%) and UV + visible light (86.21%), with Ni doping improving charge separation, as reflected in the photocatalytic performance [226].

In another investigation undertaken by Balarabe, *Moringa* leaf extract was used as a stabilizing agent in the biosynthesis of plasmonic gold-titania nanoparticles (Au@AuNPs), which were tested as green catalysts for the photodegradation of ciprofloxacin (CIP) pollutant under visible light. Characterization results showed a uniform distribution of nanoparticles with a diameter of around 10 nm on the anatase TiO_2 nanoparticle surface, enhancing the photocatalytic activity of the Au@AuNPs, which degraded approximately 95% of CIP at high concentration under visible-light conditions [227]. Similarly, Golmohammadi et al. successfully recycled *Melia azedarach* fruit by using its extract to synthesize silver nanoparticles impregnated on amorphous silica extracted from rice husk (Ag/silica nanocomposite), which, as a photocatalyst, showed excellent efficiency in removing the CIP antibiotic from an aqueous medium under direct sunlight. Experimental findings demonstrated the effective deposition of eco-friendly silver nanoparticles on amorphous silica, resulting in 98% photodegradation of the CIP pollutant by the Ag/silica nanocomposite under optimal conditions of pH (6.7), reaction time (180 min), and catalyst load (0.12 g) [228].

Recently, Aggarwal et al. targeted the photocatalytic removal of the tetracycline (TC) pharmaceutical pollutant using $NiFe_3O_4$NPs formulated via a bioinspired synthesis pathway using extracts of *Psidium guajava* and *Terminalia chebula* plants. The two resulting spinel nanocatalysts (NFTC and NFGL), with the required form and crystalline structure, reduced the TC organic pollutant in solution by over 93% in just 30 min under visible-light illumination, demonstrating their excellent photocatalytic activity, which remained stable over several regeneration cycles [229]. In the case of Nguyen et al., biosynthesis of ZnONPs and Ag-ZnONPs at varying proportions (0.5%, 1%, 3%, 5%, and 7%) via an alkali-free process using *Morinda citrifolia* fruit extract was studied. The nanocatalysts developed were applied to degrade tetracycline (TC) under visible-light illumination. Incorporation of Ag into ZnO at 1% significantly enhanced visible light absorption, improved carrier separation, and facilitated charge transport of the Ag-1%/ZnO nanocomposite, resulting in the highest photocatalytic performance in TC degradation with an efficiency of 84% [230].

On the other hand, Mahlaule-Glory et al. examined the photocatalytic degradation of sulfisoxazole (SSX) antibiotic waste using Fe_3O_4NPs, which were greenly fabricated via wet-chemical synthesis from the aqueous extract of the *Mammoth Burkina* plant. The Fe_3O_4NPs were characterized as rod-shaped, mesoporous, and showing signs of phytochemical deposition, with a bandgap of 3.74 eV. These properties enabled Fe_3O_4NPs to exhibit excellent photoactivity, resulting in approximately 60% degradation of SSX (10 mg L^{-1}) at a dose of 1 g L^{-1} after 120 min under UV irradiation [231]. Moreover, Sanjeev and Valsan have prepared biogenic, eco-friendly ZnONPs using the aqueous extract of *neem* (*Azadirachta indica*) leaves. These nanoparticles were then immobilized by coating them onto activated carbon derived from spent tea waste (TAC), producing a recyclable, reusable ZnONPs@TAC nanocomposite. Under optimal conditions, the resulting ZnONPs@TAC photocatalyst completely removed the pharmaceutical compounds acetaminophen (ATP) and sulfadiazine (SFZ) from aqueous solution after 30 min and 90 min, respectively, upon UV illumination [232].

5.2.2. Photodegradation of Pesticides

The intensive use of pesticides in agriculture, while essential for pest control and crop productivity, has resulted in significant environmental pollution. These chemical compounds, including commonly used herbicides such as glyphosate, atrazine, and chlorpyrifos, are often detected in soil, surface water, and groundwater due to their high solubility and persistence. Even at low concentrations, pesticides pose serious threats to ecosystems and human health, with documented effects such as hormonal disruption, neurological damage, and potential carcinogenicity [233]. Traditional treatment methods often struggle to completely remove these stable compounds from water bodies. Among emerging approaches, photocatalysis holds promise as a technique for breaking down pesticide molecules into less harmful substances. In particular, plant-based nanoparticles offer an eco-friendly and sustainable alternative to conventional catalysts. Thanks to their natural origin, ease of synthesis, and ability to produce reactive oxygen species under light, they show great potential in degrading pesticide residues [138]. This section reviews recent advancements in using plant-based nanoparticles for the photocatalytic degradation of pesticides in contaminated water.

In this context, Purkait et al. explored a novel, environmentally and economically sustainable green photocatalyst, prepared from *Trema orientalis* extract as TiO_2NPs, to assess its performance in photodegrading the hazardous herbicide flurasulam. The resulting data indicated that the small size and broad dispersion of the engineered TiO_2 nanoparticles led to almost complete elimination of florasulam after a few hours under UV light, with the pseudo-first-order model fitting the experimental kinetic data best [234]. In a study also conducted by Purkait et al., green synthesis of zinc oxide nanoparticles was achieved using the aqueous extract of *Trema orientalis* (L.) leaves, and the nanoparticles were tested as a photocatalyst for the UV-light-mediated degradation of zoxamide, a benzamide fungicide. The resulting green catalyst yielded nanoparticles with a mean crystalline size of 24 nm and a particle size of 65–67 nm, with a direct band gap of 3.13 eV. It demonstrated excellent photocatalytic performance for removing zoxamide from aqueous media at pH 10, requiring about 6 h under UV irradiation [235]. In the same vein, Iqbal et al. tested the photocatalytic removal of lambda-cyhalothrin (L-CHT) using two types of nanocomposites, copper oxide (CuO) and nickel oxide (NiO), produced via an eco-friendly biosynthetic process using a natural reducing agent derived from phytochemicals in *Capparis decidua* leaf extract. The high photocatalytic activity of the new spherical flower-shaped nanoparticles resulted in approximately 99% L-CHT removal by the CuO nanocomposite and approximately 89% by the NiO nanocomposite after three hours of exposure to UV light using a photocatalyst

dose of 2 mg L^{-1}, an L-CHT concentration of 20 mg L^{-1}, and pH 7 as optimum operating conditions [236]. In another work by Rani et al., a cost-effective green synthesis method using *green tea* extract was adopted to prepare a silver-doped metal hexacyanoferrate (Ag@MHCFs) nanocomposite for photocatalytic degradation of the endosulfan (ES) and atrazine (AT) pesticides from aqueous solutions under direct sunlight. The large specific surface area of 89.3 m^2/g, the high zeta potential of −43.4 mV, the low band gap of 1.5 eV, and the weak photoluminescence intensity all contributed to Ag@FeHCF's enhanced photocatalytic activity in removing ES and AT with maximum degradation efficiencies of 98% and 96%, respectively, at a pollutant concentration of 5 mg L^{-1}, a catalyst dosage of 20 mg for ES and 15 mg for AT, and at neutral pH under sunlight. Meanwhile, this green catalyst demonstrated excellent reusability, ensuring charge separation, stability, and durability [237]. In addition, Singh and Devi studied the performance of bimetallic copper-zinc nanoparticles (Cu–Zn BMNPs) prepared by an environmentally friendly method using an aqueous extract of the *Zinger* plant in the photodegradation of carbendazim, chlorpyrifos, monocrotophos, and cypermethrin as organic pesticides. Characterization results showed that Cu-Zn BMNPs with diameters ranging from 60 to 100 nm formed stably under high pH conditions, demonstrating high photocatalytic efficiency in eliminating 53–95% of the four pesticides over an incubation period of 24–72 h under visible light [238].

5.2.3. Photodegradation of Other Organic Pollutants

Industrial development and urbanization have continuously released various organic pollutants into the environment, particularly phenolic compounds such as bisphenol A, 4-chlorophenol, and dinitrophenol. These substances are difficult to eliminate through conventional treatment due to their chemical stability and resistance to natural degradation. As a result, they persist in aquatic environments, where they can accumulate and exert toxic effects on living organisms [189]. To address this issue, photocatalytic degradation has emerged as a practical approach for breaking down such pollutants into less harmful byproducts. Recently, plant-based nanoparticles have shown promise in this field, offering a sustainable and efficient pathway for environmental remediation. Their ability to generate multiple reactive species under light exposure enables the rapid decomposition of stubborn organic molecules. This subsection explores recent advances in using plant-derived nanoparticles to photodegrade diverse organic pollutants, with a focus on improving water quality and reducing ecological risks.

For instance, Devi et al. adopted an ecological approach by exploiting the plant biomass present in the *carambola* leaf extract to design green gold nanoparticles (gAuNPs) loaded onto reduced graphene oxide (RGO) and applying them as photocatalysts in the removal of bisphenol-A (BPA), 2-nitrophenol (2-NP), 2-chlorophenol (2-CP), and phenol (P) pollutants. The synergistic action of superconducting gold nanoparticles and the RGO sheets' π-conjugated carbon network enhanced the photocatalytic efficiency of gAuNPs loaded at 2% on RGO (2gAu/RGO) in removing BPA, 2-NP, 2-CP, and P by around 98.92%, 97.64%, 92.67%, and 89.16%, respectively, in 130 min at normal pH under visible light illumination [239]. Likewise, Haseena et al. researched the photocatalytic removal of phenol pollutant from aqueous solution using two types of α-Fe_2O_3 nanoparticles biotreated with *Phyllanthus niruri* (PN) and *Moringa stenopetala* (MS) leaf extracts. Physicochemical characterizations confirmed the successful formation of spherical α-Fe_2O_3NPs with a rhombohedral structure, on which adsorption of PN and MS extract biomolecules was observed, and they contained Fe-2p and O-1s elements, which reflected positively on the photocatalytic activity of the resulting α-Fe_2O_3 nanocomposites. The rapid production of $\bullet O_2^-$ and •OH radicals during the photocatalytic process enabled PNFO and MSFO to have high phenol degradation efficiencies of 90% and 92%, respectively, after 240 min

of visible light illumination [240]. In another study, Velázquez-Hernández et al. evaluated photosynthesis using *Eichhornia crassipes* leaf extract containing titanium dioxide nanoparticles (TiO_2NPs), which serve as catalysts in the photocatalytic degradation of the phenol pollutant. The photosynthesized TiO_2 nanoparticles with a bandgap energy of 3.2 eV, a tetragonal crystalline form, and particle sizes ranging from 20 to 50 nm showed high photocatalytic efficiency in the photodegradation of phenol (10 mg L^{-1}) at acidic pH, achieving 98.7% after 120 min under ultraviolet light [241]. Recently, Ahmad et al. reported using a leaf extract of *Cyropegia omissa Huber* to prepare eco-friendly photocatalytic zinc oxide nanocubes that effectively degraded 86% of BPA in just 30 min under visible light. It was revealed that the excellent photocatalytic activity of ZnO nanocubes was due to their high crystallinity and 3.1 eV band gap. The plant biomolecules distributed on the surface of ZnONPs played a crucial role in increasing the zinc ion valency and facilitating oxygen binding [242].

In photodegradation processes, plant-based nanoparticles benefit from both their nanoscale structure and bio-derived surface modifiers. The presence of phytochemical residues can act as sensitizers or electron donors, enhancing light absorption and facilitating charge transfer under irradiation. These surface species also help suppress electron–hole recombination, thereby increasing the lifetime of reactive charge carriers. As a result, the generation of reactive oxygen species such as •OH and $O_2\bullet^-$ is enhanced, enabling more effective degradation of adsorbed pollutants. The strong synergy between adsorption and photodegradation ensures that contaminants are rapidly degraded at the nanoparticle surface, thereby improving photocatalytic efficiency.

This section reviews selected studies in which plant-mediated metal oxide nanoparticles have been explored as photocatalysts for the removal of organic contaminants, including dyes, pharmaceutical residues, pesticides, and related compounds. Table 3 summarizes representative investigations that report photocatalytic performance under several experimental conditions. Rather than serving as a direct basis for performance comparison, the table is intended to illustrate recurring tendencies observed across the literature. In many cases, substantial pollutant removal can be achieved by optimizing the synthesis parameters and operating conditions. Reported photodegradation efficiencies (PDEs) are influenced by several interconnected factors, including the type of metal oxide used, the chemical composition of the plant extract, and key operational variables such as solution pH, initial pollutant concentration, catalyst dosage, irradiation time, and light source characteristics. Differences in optical bandgap values further affect light absorption and the reactive species generation, contributing to variability in photocatalytic behavior. It is important to note that most degradation efficiencies reported in Table 3 are derived from changes in UV–visible absorbance and therefore primarily reflect discoloration rather than complete mineralization. Consequently, direct quantitative comparison among studies should be approached with caution, as irradiance, wavelength range, reactor configuration, mixing conditions, and evaluation criteria are not uniform across reports. Taken together, these studies nonetheless demonstrate the adaptability of plant-derived metal oxide nanoparticles and support their promise as environmentally sustainable photocatalysts for water treatment applications.

The composition of plant extracts has a key role in determining the functional and structural properties of the synthesized nanoparticles. Compounds like flavonoids, phenolics, and other oxygen-containing biomolecules act as reducing agents, stabilizers, and capping agents during nanoparticle formation. These molecules affect nucleation and growth kinetics, leading to variations in crystallinity, particle size, morphology, and surface chemistry.

Table 3. Efficiency of plant-based metal oxide nanoparticles in removing various types of organic pollutants under different operating conditions.

Pollutant Types	Pollutant Example	Plant Species	Metal Salt Solution	NPs	Bandgap (eV)	Light Source	Power (W)/λ (nm)	Reactor	Operating Factors				PDE (%)	Efficiency Definition	Ref.
									Ci (mg L^{-1})	pH	Dose (g L^{-1})	Time (Min)			
Dyes	Methylene blue	*Citrus jambhiri lushi*	$Zn(CH_3COO)_2$	ZnO	3–3.05	UV	-	Photoreactor	10	-	0.05	120	96.0	Decolorization	[243]
		Monsonia burkeana	TiF_4	TiO_2	3.53	UV	300 W	Batch reactor	20	10	0.24	120	85	Decolorization	[244]
Dyes		*Phoenix dactylifera*	$AgNO_3$	Ag/Ag_2O	2.07–2.86	UV and Vis	-	Batch reactor	-	6.4	0.01	50	84.5	Decolorization	[245]
		Leucophyllum frutescens	$Cu(NO_3)_2$	CuO	2.53	Vis	-	-	-	-	0.10	120	88	Decolorization	[246]
		Camellia sinensis	$Mg(NO_3)_2$	MgO	4.21	UV	8 W	Batch reactor	1	-	0.25	120	97	Decolorization	[247]
	Methyl orange	*Vernonia amygdalina*	$Fe(NO_3)_3$	α-Fe_2O_3	2.07	UV	8 W	-	10	6	0.71	90	93.5	Decolorization	[248]
		Mimosa tenuiflora	$Zn(NO_3)_2$	ZnO	3.37	UV	10 W	Photoreactor	15	-	0.05	90	96	Decolorization	[249]
		Hibiscus sabdariffa	$AgNO_3 + PdCl_2$	Ag–Pd	-	Sunlight	-	-	-	-	0.25	120	67.88	Decolorization	[250]
		Punica granatum	$Ni(NO_3)_2$	NiO	3.5	UV	-	Photoreactor	10	3	2.0	0.62	90	Decolorization	[251]
		Hedyotis capitellata	$Ce(NO_3)_3 + Zn(NO_3)_2$	HC-Ce@ZnO	2.59	Vis	-	-	10	5	0.50	240	92	Decolorization	[252]
	Rhodamine B	*Shorea robusta*	$AgNO_3$	Ag	-	UV	11 W	Photoreactor	20	7	1.0	90	90.41	Decolorization	[253]
		Origanum vulgare	$Zn(NO_3)_2$	ZnO	2.29	UV	10 W	Photoreactor	15	-	1.0	100	94.24	Decolorization	[254]
		Cocos nucifera	$FeCl_3$	Fe_2O_3	1.82	Vis	300 W	Photoreactor	10	-	1.0	50	92	Decolorization	[255]
		Citrus × paradisi	$SnCl_2$	SnO_2	2.69	UV	10 W	Photoreactor	15	-	1.0	60	100	Mineralization	[256]
		Citrofortunella microcarpa	$Cu(NO_3)_2$	CuO	2.86	UV	-	Photoreactor	10	7	0.01	100	98.31	Decolorization	[257]
	Congo red	*Tribulus terrestris*	$NiCl_2$	NiO	-	UV/Vis	245 nm	Photoreactor	15	-	0.2	20	92	Decolorization	[258]
		Epipremnum aureum	$Zn(CH_3COO)_2$	ZnO	3.73	UV	-	UV chamber	10	2	0.4	100	80.82	Decolorization	[259]
Dyes	Congo red	*Catharanthus roseus*	$Mg(NO_3)_2 + AgNO_3$	Ag-MgO	2.70	UV	-	UV chamber	10	-	0.1	120	80	Decolorization	[260]
		Sutherlandia frutescens	TiF_4	TiO_2	3.19	UV	300 W	Photoreactor	5	-	0.1	120	87.76	Decolorization	[34]
		Mukia madrasapatna	$Ti[OCH(CH_3)_2]_4 + NiCl_2$	Ni-TiO_2	2.84	UV	450 W/250 nm	Photoreactor	10	7	0.8	180	92.31	Decolorization	[261]

Table 3. *Cont.*

Pollutant Types	Pollutant Example	Plant Species	Metal Salt Solution	NPs	Bandgap (eV)	Light Source	Power (W)/λ (nm)	Reactor	Operating Factors				PDE (%)	Efficiency Definition	Ref.
									Ci (mg L^{-1})	pH	Dose (g L^{-1})	Time (Min)			
Pharmaceuticals	Sulfisoxazole	*Commelina benghanlensis*	TiF_4	TiO_2	3.69	UV	-	UV reactor	20	12	0.1	120	82.4	Degradation	[262]
		Commelina benghalensis	$Zn(NO_3)_2$	ZnO	3.40	UV	-	Pho-tore-actor	20	-	0.3	120	46	Degradation	[263]
		Monsonia burkeana	$Fe(NO_3)_3$ + $Cu(NO_3)_2$ + $AgNO_3$	$AgCuFe_2O_4$	3.71	UV	150 W	Pho-tore-actor	10	-	1.0	120	60	Degradation	[33]
		Sutherlandia frutescens	$CdCl_2$ + Na_2S	CdS	3.55	UV	300 W	Pho-tore-actor	10	-	1.0	120	68	Degradation	[264]
		Monsonia burkeana	$Ni(NO_3)_2$ + $Fe(NO_3)_2$	$NiFe_2O_4$	3.64	UV	150 W	cylindrical quartz	10	-	1.0	120	74	Degradation	[265]
	Ciprofloxacin Amoxicillin	*Euphorbia polygonifolia*	$FeCl_3$ + $FeCl_2$ + $CuSO_4$	Fe_3O_4-CuO	1.57	UV	-	Pho-tore-actor	10	7	1.5	60	94	Degradation	[266]
		Moringa oleifera	$Zn(NO_3)_2$ + $Ce(NO_3)_3$ + $AgNO_3$	Ag@ZnO-CeO_2	2.00	Sunlight	-	-	-	-	0.1	120	74	Mineralization	[267]
		Juglans regia	$Ni(NO_3)_2$ + $Fe(NO_3)_3$	$NiFe_2O_4$	1.53	UV	-	Pho-tore-actor	5	3	-	60	90	Degradation	[268]
		Melia Azedarach	$AgNO_3$	Ag/Silica	-	Sunlight	-	-	40	6.7	0.6	180	98	Mineralization	[228]
	Ofloxacin	*Moringa*	$Ti[OCH(CH_3)_2]_4$ + $HAuCl_4$	TiO_2@Au	3.01	Vis	125 W	Photoreactor	50	-	0.025	60	95.53	Degradation	[227]
		Ocimum basilicum	$Ti[OCH(CH_3)_2]_4$	TiO_2	-	Solar irra-diation	-	Batch mode reactor	10	5	0.25	150	91.36	Mineralization	[70]
		Aloe Vera	$CuSO_4$ + $MnSO_4$	Mn-Doped Cu_2O	2.2	Sunlight	900 W/m^2	-	15	9	1.0	160	92	Degradation	[269]
		Dalbergia parviflora	$Zn(NO_3)_2$	ZnO	3.22	UV	125 W	Photoreactor	10	-	0.25	120	95	Degradation	[270]
	Sulfamethoxazole	*Sutherlandia frutescens*	TiF_4	TiO_2	3.19	UV	300 W	Photoreactor	10	-	0.1	120	82	Degradation	[34]
	Tetracycline	*Sutherlandia frutescens*	$Zn(NO_3)_2$ + $SnCl_2$	$ZnOSnO_2$	3.08	UV	300 W	Photoreactor	10	-	0.24	120	70	Degradation	[271]
		Senna siamea	$Zn(CH_3COO)_2$	ZnO	3.10	UV	-	-	10	-	0.25	180	99	Mineralization	[272]
		Aloe vera	$FeCl_3$ + $NiCl_2$	$NiFe_2O_4$	1.84	UV	-	-	-	-	0.80	120	75	Mineralization	[273]
		Stevia rebaudiana	$Ce(NO_3)_3$	CO_2	-	UV	18 W	Plexiglas cubic photo reactor	5	10	0.75	45	80.68	Degradation	[274]
		Vernonia amygdalina	$Zn(NO_3)_2$ + Nb_2O_5	Nb-ZnO	2.25	Vis	250 W	Quartz reactor	15	7	0.25	180	93.2	Degradation	[275]
		Pometia pinnata	$NiCl_2$	NiO/rGO	3.28	UV and Vis	100 W	Batch photoreactor	20	-	0.80	30	100	Mineralization	[276]

Table 3. *Cont.*

Pollutant Types	Pollutant Example	Plant Species	Metal Salt Solution	NPs	Bandgap (eV)	Light Source	Power (W)/λ (nm)	Reactor	Operating Factors				PDE (%)	Efficiency Definition	Ref.
									Ci (mg L^{-1})	pH	Dose (g L^{-1})	Time (Min)			
Pesticides	Atrazine	*Azadirachta indica*	$Cd(O_2CCH_3)_2$ + $ZnCl_2$	ZnO@CdS	3.37	Sunlight	-	-	50	7	0.8	360	89	Mineralization	[277]
		eucalyptus	$AgNO_3$	Ag/kaolin	-	Vis	24.5 W	Photoreactor	10	-	1.0	120	66.8	Mineralization	[278]
	Endosulfan	*Camellia sinensis*	$K_3[Fe(CN)_6]$ + $AgNO_3$	Ag-FeHCF	1.5	Sunlight	-	-	5	7	0.3 0.4	30	96 98	Mineralization	[237]
	Ethion Toxaphene	*Azadirachta indica*	$Bi(NO_3)_3$ + $SnCl_2$ + HNO_3	N-doped Bi_2O_3@SnO_2	2.1	Sunlight	-	-	2	7	1.2	260	96 90	Mineralization	[279]
	2,4-DA	*Orthosiphon stamineus*	-	Ag	-	UV	29 W/400 nm	Pyrex batch photoreactor	8.15	3.24	0.009	180	98.80	Degradation	[280]
		Muntingia calabura	$Zn(CH_3COO)_2$	ZnO	3.41	Sunlight	-	-	10	-	0.2	180	99.34	Degradation	[281]
		Pedalium murex	$ZnCl_2$ + $FeCl_3$ + AgCl	$ZnFe_2O_4$@Ag	-	UV	360 nm	Photoreactor	30	7	0.04	60	94	Mineralization	[282]
	2,4-DPA	*Curcuma longa*	NH_4VO_3 + $Bi(NO_3)_3$	$BiVO_4$	2.40	Vis	≥400 nm	Photoreactor	20	-	1.0	120	90.23 70.52	Degradation	[283]
	4-aminopyridine	*Tabernaemontana divaricate*	$AgNO_3$	Ag	-	Vis	125 W	Photoreactor	5	7	1.6	120	61	Mineralization	[284]
	Malathion	*Ziziphus jujube*	$Ti(OBu)_4$	TiO_2@g-C_3N_4	2.83	UV	8 W	cylindrical quartz glass reactor	20	-	0.4	150	71	Degradation	[285]
	Diuron	*Para rubber*	$Zn(CH_3COO)_2$	ZnO	3.21	UV	18 W	Photoreactor	5	-	1.0	300	34.8	Degradation	[286]
Pesticides	chlorpyrifos	*Melia azedarach*	$Cu(NO_3)_2$ + $Zn(NO_3)_2$	Cu–ZnO	2.92	Sunlight	-	Batch reactor	200	6	3.0	240	91	Mineralization	[287]
	Thiamethoxam	*Basil tulsi*	$NiNO_3$ + $Mn(CH_3COO)_2$	NiO/Mn_3O_4	2.39–2.67	Sunligh	-	-	20	6	0.3	90	93	Mineralization	[288]

Table 3. *Cont.*

Pollutant Types	Pollutant Example	Plant Species	Metal Salt Solution	NPs	Bandgap (eV)	Light Source	Power (W)/λ (nm)	Reactor	Operating Factors				PDE (%)	Efficiency Definition	Ref.
									Ci (mg L^{-1})	pH	Dose (g L^{-1})	Time (Min)			
Others	Phenol	*Elaeis guineensis*	$Ce(NO_3)_3$	CeO_2	-	Vis	500 W	Batch photoreactor	-	-	-	360	92.24	Degradation	[289]
	4-Nitrophenol	*Banana peel*	$ZnCl_2 + (NH_2)_2CS$	ZnS	4.12	UV	75 W/365 nm	Glass cell photoreactor	20	10	0.6	120	80 71	Degradation	[290]
	4-Chlorophenol	*Ficus Johannis*	$Zn(NO_3)_2 + Na_2S$	ZnS	-	UV	36 W	Photoreactor	25 50	-	0.2	120	- -	Degradation	[291]
	3-Amino phenols	*Azadirachta indica*	$Cu(NO_3)_2$ + $Fe(NO_3)_3$	$CuFe_2O_4$	2.40	Sunlight	452 ± 183 W/m^2	-	20	7	5.33	300	93	Mineralization	[292]
	Bisphenol-A	*Maple*	$AgNO_3 + TiO_2$ powder	Ag–TiO_2	2.83	UV	40 W	Box photoreactor	10	3	2	15	96.83	Degradation	[293]
		Arcopilus globulus	$MnSO_4$	AGE-Mn	-	Sunlight	-	-	20	-	0.2	180	66.3	Degradation	[294]
	4-Nonylphenol	*Azadirachta indica*	$Bi(NO_3)_3$ + $Cu(NO_3)_2$	CuS-Bi_2O_3	2.32	Sunlight	-	-	50	7	0.2	180	91 97	Mineralization	[295]
	2,4-Dinitrophenol	*Chlorella vulgaris*	$FeCl_3$	Fe_3O_4	2.3–2.73	UV	-	Photoreactor	50	6	0.3	60	>85	Degradation	[296]

Therefore, XRD and FTIR analyses confirm the presence of surface-bound functional groups extracted from the plant, reducing agglomeration, promoting the formation of well-defined crystalline planes, and enhancing particle stabilization. The increased specific surface area and decreased crystal size, coupled with improved crystallinity, enable more efficient charge transport, critical for photocatalytic activity. Furthermore, the surface biomolecules provide active sites that enhance adsorption via hydrogen bonds, van der Waals forces, and electrostatic interactions.

The adsorption performance of nanoparticles is directly related to the surface characteristics induced by the extract. Nanoparticles with abundant functional groups and a larger specific surface area have a greater capacity to adsorb pollutants. Similarly, photocatalytic efficiency is modulated by surface and structural characteristics: smaller particle size shortens the diffusion length of photogenerated carriers, while high crystallinity minimizes electron-hole recombination. Surface biomolecules further facilitate the adsorption of target molecules and enhance interfacial charge transfer, thereby improving degradation rates under irradiation.

Overall, these observations demonstrate a clear mechanistic relationship in which the phytochemical composition of the plant extract governs nanoparticle formation and surface chemistry, which, in turn, controls their adsorption capacity and photocatalytic activity. This structure-activity correlation highlights the importance of the choice and composition of plant extracts in optimizing the performance of environmentally synthesized nanomaterials for environmental applications.

6. Conclusions, Prospects, and Limitations

6.1. Conclusions

The growing pressure posed by water pollution and resource depletion has accelerated interest in sustainable nanomaterial design. In this context, plant-mediated synthesis of metallic and metal oxide nanoparticles has emerged as a credible alternative to conventional chemical routes, combining reduced environmental impact with functional performance. This review consolidates recent advances in the green synthesis of plant-based nanoparticles, with particular emphasis on their physicochemical properties and their relevance to water treatment applications.

Across the literature, a consistent structure–property–performance relationship is evident. The chemical composition of plant extracts, especially polyphenols, flavonoids, terpenoids, sugars, and proteins, directly governs metal-ion reduction, nucleation, and growth. These biomolecules also serve as capping agents, influencing particle size, morphology, surface functional groups, and colloidal stability. In turn, these properties determine adsorption capacity, surface reactivity, light-absorption behavior, and charge-transfer efficiency during photocatalytic processes. Nanoparticles synthesized from polyphenol-rich extracts typically exhibit smaller crystallite sizes, higher surface areas, and improved dispersion, which translate into enhanced adsorption of metal ions and dyes, as well as improved photocatalytic degradation of organic pollutants.

Physicochemical characterization using complementary techniques, including UV–visible spectroscopy, X-ray diffraction, Fourier Transform Infrared spectroscopy, scanning and transmission electron microscopy, and energy-dispersive X-ray analysis, remains essential for correlating synthesis parameters with functional performance. Collectively, the reviewed studies demonstrate that plant-based nanoparticles, particularly Ag, ZnO, TiO_2, and Fe-based systems, can achieve competitive removal efficiencies for heavy metals, dyes, pharmaceuticals, and other persistent contaminants when their structure and surface chemistry are properly controlled.

6.2. Current Limitations and Knowledge Gaps

Despite the considerable progress achieved in the development of plant-based nanoparticles for water purification, several factors still limit their reliable application and large-scale implementation.

One of the primary challenges concerns reproducibility. The physicochemical characteristics of green-synthesized nanoparticles are strongly influenced by the botanical source of the extract, geographical origin, seasonal variations, extraction procedures, and the chemical nature of the precursor salts. In addition, synthesis parameters such as pH, temperature, precursor concentration, and reaction time play a decisive role in nucleation and particle growth processes. Even small deviations in these variables can lead to significant differences in particle size distribution, crystallinity, morphology, and surface chemistry, making it difficult to compare results across studies or establish broadly applicable design guidelines.

Another important limitation is the incomplete mechanistic understanding of nanoparticle formation. Although spectroscopic techniques such as FTIR and UV–visible spectroscopy are frequently used to suggest the participation of functional groups in reduction and stabilization steps, these methods rarely provide direct identification of the specific phytochemicals responsible for electron transfer and surface capping. As a result, many proposed synthesis pathways remain based on indirect interpretations rather than detailed molecular or kinetic evidence. Similarly, operational factors such as pH are often reported only as experimental conditions, without thorough discussion of their effects on nucleation kinetics, surface charge development, zeta potential, colloidal stability, and the resulting adsorption or photocatalytic behavior.

Environmental considerations also represent a significant knowledge gap. The high dispersibility of nanoparticles in aqueous systems enhances their interaction with pollutants but may also introduce potential ecological risks. Under irradiation, nanoparticles can generate reactive oxygen species that are beneficial for contaminant degradation yet may induce oxidative stress in aquatic organisms. Issues related to metal ion release, long-term persistence, bioaccumulation, and trophic transfer have not been systematically evaluated in many studies, and available toxicity assessments are often limited to short-term laboratory experiments rather than long-term ecological investigations.

Practical aspects related to catalyst recovery further complicate real-world applications. Because nanoparticles act as catalysts and remain suspended in treated water, their separation after treatment can be technically challenging. Inefficient recovery may lead to secondary contamination or environmental accumulation. Although strategies such as immobilization, magnetic modification, membrane integration, and composite fabrication have been proposed, these approaches are not consistently incorporated into experimental performance evaluations.

Finally, most reported investigations rely on simplified batch experiments using single model pollutants under controlled laboratory conditions. The long-term stability of nanoparticles, their regeneration capability over repeated cycles, and their performance in real wastewater systems containing competing ions and natural organic matter remain insufficiently explored. In addition, limited attention has been given to life-cycle assessment, economic feasibility, and energy consumption, all of which are essential for evaluating the sustainability and scalability of these technologies.

Addressing these limitations will be critical for translating laboratory-scale advances into dependable and environmentally responsible water treatment solutions based on plant-derived nanomaterials.

6.3. Future Perspectives and Research Priorities

To advance the field responsibly, future research should adopt more systematic and integrated approaches that connect plant extract chemistry, synthesis parameters, nanoparticle characteristics, environmental behavior, and treatment performance.

Improving reproducibility should be a primary objective. Establishing standardized extraction procedures and benchmark synthesis protocols for widely studied systems would facilitate cross-study comparison and help define reliable structure–property–performance relationships. Advanced analytical profiling of plant extracts using chromatographic and spectrometric techniques should be combined with conventional nanoparticle characterization to clarify reduction mechanisms and stabilization pathways. Such integration would enable more rational control over particle size, morphology, surface charge, and defect density.

Environmental safety must be treated as a central research priority rather than a secondary consideration. Future studies should systematically evaluate nanoparticle stability in aquatic environments, including aggregation behavior, dissolution kinetics, ion release, and transformation under irradiation. Comprehensive ecotoxicity assessments involving representative aquatic organisms, oxidative stress biomarkers, and chronic exposure studies are essential to determine whether photocatalytic benefits outweigh potential ecological risks.

Equally important is the development of effective recovery strategies. Immobilized systems, magnetic nanocomposites, membrane-supported catalysts, and structured reactors offer promising routes to minimize nanoparticle release into treated water. Designing materials with both high activity and straightforward separability will be critical for real-world implementation.

Application-focused research should also expand beyond model dyes toward more complex and realistic pollutant mixtures, including pharmaceuticals, antibiotic combinations, endocrine-disrupting compounds, and multi-contaminant systems. Experiments conducted under simulated or real wastewater conditions will provide more meaningful insights into operational robustness.

Recent studies on engineered hybrid treatment systems demonstrate that integrating advanced functional materials into continuous-flow platforms can significantly enhance long-term operational stability and pollutant removal efficiency, highlighting the importance of translating laboratory-scale nanomaterials into practical environmental technologies [180,181].

Finally, future work should integrate performance evaluation with life-cycle assessment, energy consumption analysis, and economic feasibility studies. Only by addressing efficiency, safety, recovery, and sustainability simultaneously can plant-based nanoparticles transition from laboratory demonstrations to scalable and environmentally responsible water treatment technologies.

By acknowledging these limitations and prioritizing these research directions, the field can move toward safer, more reproducible, and genuinely sustainable applications of plant-derived nanomaterials in water purification.

Author Contributions: Conceptualization, M.E.A., H.S., Y.R., S.B. and S.A.; methodology, M.E.A., H.S., Y.R., S.B. and S.A.; software, B.A.; validation, H.S., S.B. and S.A.; formal analysis, B.A. and Y.R.; investigation, B.A.; data curation, Y.R.; writing—original draft preparation, M.E.A., B.A., R.B., M.B.T., A.B. and W.A.; writing—review and editing, M.E.A., B.A., R.B., M.B.T., A.B. and W.A.; visualization, H.S., S.B. and S.A.; supervision, S.A. All authors have read and agreed to the published version of the manuscript.

Funding: This research received no external funding.

Institutional Review Board Statement: Not applicable.

Informed Consent Statement: Not applicable.

Data Availability Statement: Original contributions presented in this study are included in this article.

Acknowledgments: This work has been made possible with the assistance of several people. All thanks to the authors for their collaboration, excellent articles, precious help, patience, and proofreading and corrections. Thanks to everyone who helped and contributed to this research.

Conflicts of Interest: The authors declare no conflicts of interest.

Abbreviations

The following abbreviations are used in this manuscript:

2CP	2-chlorophenol
2NP	2-nitrophenol
AMX	Amoxicillin
AT	Atrazine
ATP	Acetaminophen
BET	Brunauer–Emmett–Teller
BPA	Bisphenol-A
CIP	Ciprofloxacin
CP	Chlorpyrifos
CR	Congo Red
CV	Crystal Violet
EDX	Energy Dispersive X-Ray Spectroscopy
ES	Endosulfan
FT-IR	Fourier Transform Infra-Red
IBU	Ibuprofen
L-CHT	Lambda-cyhalothrin
MB	Methylene Blue
MO	Methyl Orange
NPs	Nanoparticles
NPX	Naproxen
P	Phenol
PDE	Photodegradation efficiency
RB	Rose Bengal
RhB	Rhodamine B
ROS	Reactive Oxygen Species
SAED	Selected Area Electron Diffraction
S_{BET}	BET specific surface area
SEM	Scanning Electron Microscopy
SFZ	Sulfadiazine
SSX	Sulfisoxazole
TBZ	Tebuconazole
TB	Toluidine Blue
TC	Tetracycline
TEB	Tebuconazole
TEM	Transmission Electron Microscopy
TH	Thiamethoxam
UV-Vis	Ultraviolet-Visible
XPS	X-ray Photoelectron Spectroscopy
XRD	X-ray Diffraction

References

1. Ijaz, I.; Bukhari, A.; Gilani, E.; Nazir, A.; Zain, H.; Saeed, R.; Hussain, S.; Hussain, T.; Bukhari, A.; Naseer, Y.; et al. Green synthesis of silver nanoparticles using different plants parts and biological organisms, characterization and antibacterial activity. *Environ. Nanotechnol. Monit. Manag.* **2022**, *18*, 100704. [CrossRef]
2. Gupta, D.; Boora, A.; Thakur, A.; Gupta, T.K. Green and sustainable synthesis of nanomaterials: Recent advancements and limitations. *Environ. Res.* **2023**, *231*, 116316. [CrossRef]
3. Osman, A.I.; Zhang, Y.; Farghali, M.; Rashwan, A.K.; Eltaweil, A.S.; Abd El-Monaem, E.M.; Mohamed, I.M.A.; Badr, M.M.; Ihara, I.; Rooney, D.W.; et al. Synthesis of green nanoparticles for energy, biomedical, environmental, agricultural, and food applications: A review. *Environ. Chem. Lett.* **2024**, *22*, 841–887. [CrossRef]
4. Muthukrishnan, S.; Bhakya, S.; Ramalingam, V. Metal nanoparticles synthesis: An overview of different synthesis methods, mode of action and their biomedical application. *Discov. Appl. Sci.* **2025**, *7*, 1079. [CrossRef]
5. Ren, G.; Han, H.; Wang, Y.; Liu, S.; Zhao, J.; Meng, X.; Li, Z. Recent Advances of Photocatalytic Application in Water Treatment: A Review. *Nanomaterials* **2021**, *11*, 1804. [CrossRef] [PubMed]
6. Sun, N.; Ren, Z.; Chen, P.; Yue, M.; Wu, J.; Fu, Y.; Ma, J. Highly stretchable TPU/g-C_3N_4 composite nanofiber film for enhancing the piezo-photocatalytic sewage treatment by electrospinning-induced pretension. *npj Clean Water* **2025**, *8*, 19. [CrossRef]
7. Huang, J.; Rasouli, K.; Zong, Z.; Wang, P.; Zhang, Y.; Li, Z. Engineering a high-performance $ZnFe_2O_4$/BiOBr/MXene S-scheme heterostructure for CO_2 photoreduction and wastewater treatment. *Chem. Eng. J.* **2026**, *530*, 173675. [CrossRef]
8. Hanna, D.H.; Nady, D.S.; Wasef, M.W.; Fakhry, M.H.; Mohamed, F.S.; Isaac, D.M.; Kirolos, M.M.; Azmy, M.S.; Hakeem, G.E.; Fathy, C.A. Plant-derived nanoparticles: Green synthesis, factors, and bioactivities. *Next Mater.* **2025**, *9*, 101275. [CrossRef]
9. Khan, F.; Shahid, A.; Zhu, H.; Wang, N.; Javed, M.R.; Ahmad, N.; Xu, J.; Alam, M.A.; Mehmood, M.A. Prospects of algae-based green synthesis of nanoparticles for environmental applications. *Chemosphere* **2022**, *293*, 133571. [CrossRef]
10. Sonawane, H.; Shelke, D.; Chambhare, M.; Dixit, N.; Math, S.; Sen, S.; Borah, S.N.; Islam, N.F.; Joshi, S.J.; Yousaf, B.; et al. Fungi-derived agriculturally important nanoparticles and their application in crop stress management—Prospects and environmental risks. *Environ. Res.* **2022**, *212*, 113543. [CrossRef]
11. Kim, D.-Y.; Kim, M.; Sung, J.-S.; Koduru, J.R.; Nile, S.H.; Syed, A.; Bahkali, A.H.; Seth, C.S.; Ghodake, G.S. Extracellular synthesis of silver nanoparticle using yeast extracts: Antibacterial and seed priming applications. *Appl. Microbiol. Biotechnol.* **2024**, *108*, 150. [CrossRef] [PubMed]
12. Singh, N.A.; Narang, J.; Garg, D.; Jain, V.; Payasi, D.; Suleman, S.; Swami, R.K. Nanoparticles synthesis via microorganisms and their prospective applications in agriculture. *Plant Nano Biol.* **2023**, *5*, 100047. [CrossRef]
13. Bai, D.; Wang, Y.; Yang, X.; Lai, J.; Luo, X. Effects of Long-Term (10 Years) Remediation of *Caragana* on Soil Enzyme Activities, Heavy Metals, Microbial Diversity and Metabolic Spectrum of Coal Gangue. *Ecol. Eng.* **2022**, *181*, 106679. [CrossRef]
14. Thipe, V.C.; Karikachery, A.R.; Çakılkaya, P.; Farooq, U.; Genedy, H.H.; Kaeokhamloed, N.; Phan, D.-H.; Rezwan, R.; Tezcan, G.; Roger, E.; et al. Green nanotechnology—An innovative pathway towards biocompatible and medically relevant gold nanoparticles. *J. Drug Deliv. Sci. Technol.* **2022**, *70*, 103256. [CrossRef]
15. Maanane, F.; El Yadini, A.; El Alouani, M.; Mabrouki, J.; Saufi, H.; Tabyaoui, M. Green Development of Titanium Dioxide Using *Astragalus boeticus* for the Degradation of Cationic and Anionic Dyes in an Aqueous Environment. *Water* **2023**, *15*, 3471. [CrossRef]
16. Tiwari, A.K.; Jha, S.; Tripathi, S.K.; Shukla, R.; Awasthi, R.R.; Bhardwaj, A.K.; Singh, A.K.; Dikshit, A. Spectroscopic investigations of green synthesized zinc oxide nanoparticles (ZnO NPs): Antioxidant and antibacterial activity. *Discov. Appl. Sci.* **2024**, *6*, 399. [CrossRef]
17. Zulfiqar, Z.; Khan, R.R.M.; Summer, M.; Saeed, Z.; Pervaiz, M.; Rasheed, S.; Shehzad, B.; Kabir, F.; Ishaq, S. Plant-mediated green synthesis of silver nanoparticles: Synthesis, characterization, biological applications, and toxicological considerations: A review. *Biocatal. Agric. Biotechnol.* **2024**, *57*, 103121. [CrossRef]
18. Madani, M.; Hosny, S.; Alshangiti, D.M.; Nady, N.; Alkhursani, S.A.; Alkhaldi, H.; Al-Gahtany, S.A.; Ghobashy, M.M.; Gaber, G.A. Green synthesis of nanoparticles for varied applications: Green renewable resources and energy-efficient synthetic routes. *Nanotechnol. Rev.* **2022**, *11*, 731–759. [CrossRef]
19. Malik, A.Q.; Mir, T.U.G.; Kumar, D.; Mir, I.A.; Rashid, A.; Ayoub, M.; Shukla, S. A review on the green synthesis of nanoparticles, their biological applications, and photocatalytic efficiency against environmental toxins. *Environ. Sci. Pollut. Res.* **2023**, *30*, 69796–69823. [CrossRef]
20. Kirubakaran, D.; Wahid, J.B.A.; Karmegam, N.; Jeevika, R.; Sellapillai, L.; Rajkumar, M.; SenthilKumar, K.J. A Comprehensive Review on the Green Synthesis of Nanoparticles: Advancements in Biomedical and Environmental Applications. *Biomed. Mater. Devices* **2026**, *4*, 388–413. [CrossRef]
21. Subramaniyam, V.; Subashchandrabose, S.R.; Thavamani, P.; Megharaj, M.; Chen, Z.; Naidu, R. *Chlorococcum* sp. MM11—A novel phyco-nanofactory for the synthesis of iron nanoparticles. *J. Appl. Phycol.* **2015**, *27*, 1861–1869. [CrossRef]
22. Thomas, S.; Gonsalves, R.A.; Jose, J.; Zyoud, S.H.; Prasad, A.R.; Garvasis, J. Plant-based synthesis, characterization approaches, applications and toxicity of silver nanoparticles: A comprehensive review. *J. Biotechnol.* **2024**, *394*, 135–149. [CrossRef] [PubMed]

23. Khan, H.; Piccolella, S.; Pacifico, S. Harnessing plant extracts for green nanoparticle synthesis: Toward a sustainable future. *Mater. Today Sustain.* **2025**, *31*, 101195. [CrossRef]
24. Elgarahy, A.M.; Elwakeel, K.Z.; Akhdhar, A.; Hamza, M.F. Recent advances in greenly synthesized nanoengineered materials for water/wastewater remediation: An overview. *Nanotechnol. Environ. Eng.* **2021**, *6*, 9. [CrossRef]
25. Nasrollahzadeh, M.; Sajjadi, M.; Iravani, S.; Varma, R.S. Green-synthesized nanocatalysts and nanomaterials for water treatment: Current challenges and future perspectives. *J. Hazard. Mater.* **2021**, *401*, 123401. [CrossRef]
26. Aouan, B.; Alehyen, S.; Alouani, M.E.; Iqajtaoune, A.; Tourtit, M.B.; Saufi, H.; Fadil, M.; Taibi, M. The Dye-Contaminated Water Treatment Efficiency of Two Types of Geopolymers: A Comparative Study of Structural, Microstructural and Adsorption Properties. *J. Inorg. Organomet. Polym. Mater.* **2024**, *35*, 1819–1844. [CrossRef]
27. Parida, V.K.; Das, S.; Maity, S.; Mahanty, A.; Datta, D.; Pradhan, A. Green Synthesis of Nanocatalysts and Nanomaterials for Effluent Treatment. In *Sustainable Effluent Treatment Resource Recovery*; American Chemical Society: Washington, DC, USA, 2025; Volume 1, pp. 1–44. [CrossRef]
28. Arabkhani, P.; Asfaram, A.; Aghaei-Jazeh, M.; Ateia, M. Plant-mediated green synthesis of nanocomposite-based multifunctional adsorbent with antibacterial activity and high removal efficiency of micropollutants from contaminated waters. *J. Water Process Eng.* **2022**, *49*, 103025. [CrossRef]
29. Eltaweil, A.S.; Abd El-Monaem, E.M.; El-Subruiti, G.M.; Ali, B.M.; Abd El-Latif, M.M.; Omer, A.M. Graphene oxide incorporated cellulose acetate beads for efficient removal of methylene blue dye; isotherms, kinetic, mechanism and co-existing ions studies. *J. Porous Mater.* **2023**, *30*, 607–618. [CrossRef]
30. Batool, S.S.; Saleem, R.; Khan, R.R.M.; Saeed, Z.; Pervaiz, M.; Summer, M. Enhancing photocatalytic performance of zirconia-based nanoparticles: A comprehensive review of factors, doping strategies, and mechanisms. *Mater. Sci. Semicond. Process.* **2024**, *178*, 108419. [CrossRef]
31. Zango, Z.U.; Garba, A.; Shittu, F.B.; Imam, S.S.; Haruna, A.; Zango, M.U.; Wadi, I.A.; Bello, U.; Adamu, H.; Keshta, B.E.; et al. A state-of-the-art review on green synthesis and modifications of ZnO nanoparticles for organic pollutants decomposition and CO_2 conversion. *J. Hazard. Mater. Adv.* **2025**, *17*, 100588. [CrossRef]
32. Mariselvam, R.; Ranjitsingh, A.J.A.; Thamaraiselvi, C.; Ignacimuthu, S.J.S. Degradation of AZO dye using plants based silver nanoparticles through ultraviolet radiation. *J. King Saud Univ. Sci.* **2019**, *31*, 1363–1365. [CrossRef]
33. Makofane, A.; Motaung, D.E.; Hintsho-Mbita, N.C. Green synthesis of silver deposited on copper ferrite nanoparticles for the photodegradation of dye and antibiotics. *Appl. Surf. Sci. Adv.* **2024**, *21*, 100601. [CrossRef]
34. Langa, C.; Tetana, Z.N.; Hintsho-Mbita, N.C. Effect of calcination temperature on the synthesis of TiO_2 nanoparticles from *Sutherlandia frutescence* for the degradation of Congo red dye and antibiotics ciproflaxin and sulfamethoxazole. *Chem. Phys. Impact* **2023**, *7*, 100389. [CrossRef]
35. Wahab, A.; Muhammad, M.; Ullah, S.; Abdi, G.; Shah, G.M.; Zaman, W.; Ayaz, A. Agriculture and environmental management through nanotechnology: Eco-friendly nanomaterial synthesis for soil-plant systems, food safety, and sustainability. *Sci. Total Environ.* **2024**, *926*, 171862. [CrossRef] [PubMed]
36. Dhanapal, A.R.; Thiruvengadam, M.; Vairavanathan, J.; Venkidasamy, B.; Easwaran, M.; Ghorbanpour, M. Nanotechnology Approaches for the Remediation of Agricultural Polluted Soils. *ACS Omega* **2024**, *9*, 13522–13533. [CrossRef]
37. Jadoun, S.; Arif, R.; Jangid, N.K.; Meena, R.K. Green synthesis of nanoparticles using plant extracts: A review. *Environ. Chem. Lett.* **2021**, *19*, 355–374. [CrossRef]
38. Velgosova, O.; Dolinská, S.; Podolská, H.; Mačák, L.; Čižmárová, E. Impact of Plant Extract Phytochemicals on the Synthesis of Silver Nanoparticles. *Materials* **2024**, *17*, 2252. [CrossRef]
39. Lithi, I.J.; Nakib, K.I.A.; Chowdhury, A.M.S.; Hossain, M.S. A review on the green synthesis of metal (Ag, Cu, and Au) and metal oxide (ZnO, MgO, Co_3O_4, and TiO_2) nanoparticles using plant extracts for developing antimicrobial properties. *Nanoscale Adv.* **2025**, *7*, 2446–2473. [CrossRef]
40. Radini, I.A.; Hasan, N.; Malik, M.A.; Khan, Z. Biosynthesis of iron nanoparticles using *Trigonella foenum-graecum* seed extract for photocatalytic methyl orange dye degradation and antibacterial applications. *J. Photochem. Photobiol. B* **2018**, *183*, 154–163. [CrossRef]
41. Rac, O.; Suchorska-Woźniak, P.; Fiedot, M.; Teterycz, H. Influence of stabilising agents and pH on the size of SnO_2 nanoparticles. *Beilstein J. Nanotechnol.* **2014**, *5*, 2192–2201. [CrossRef]
42. Şahin, A.; Altınsoy, Ş.; Kızılbey, K. An approach for cationic dyes removal from wastewater: Green synthesis of iron nanoparticles using Prunus avium stems extracts. *Kuwait J. Sci.* **2024**, *51*, 100226. [CrossRef]
43. Alkhulaifi, M.M.; Alshehri, J.H.; Alwehaibi, M.A.; Awad, M.A.; Al-Enazi, N.M.; Aldosari, N.S.; Hatamleh, A.A.; Abdel-Raouf, N. Green synthesis of silver nanoparticles using Citrus limon peels and evaluation of their antibacterial and cytotoxic properties. *Saudi J. Biol. Sci.* **2020**, *27*, 3434–3441. [CrossRef] [PubMed]

44. Sachin; Jaishree; Singh, N.; Singh, R.; Shah, K.; Pramanik, B.K. Green synthesis of zinc oxide nanoparticles using lychee peel and its application in anti-bacterial properties and CR dye removal from wastewater. *Chemosphere* **2023**, *327*, 138497. [CrossRef] [PubMed]
45. Abegunde, S.M.; Adebayo, M.A.; Olasehinde, E.F. Green synthesis of ZnO nanoparticles and its application for methyl green dye adsorption. *Green Energy Resour.* **2024**, *2*, 100073. [CrossRef]
46. Mali, S.C.; Dhaka, A.; Githala, C.K.; Trivedi, R. Green synthesis of copper nanoparticles using *Celastrus paniculatus* Willd. leaf extract and their photocatalytic and antifungal properties. *Biotechnol. Rep.* **2020**, *27*, e00518. [CrossRef]
47. Nguyen, P.A.; Nguyen, A.V.P.; Dang-Bao, T.; Phan, H.P.; Nguyen, T.T.V.; Tran, B.A.; Huynh, T.L.D.; Hoang, T.C.; Huynh, V.T.; Nguyen, T. Green synthesis of copper nanoparticles using Cocoa pod extract and its catalytic activity in deep oxidation of aromatic hydrocarbons. *SN Appl. Sci.* **2020**, *2*, 1795. [CrossRef]
48. Eltaweil, A.S.; Fawzy, M.; Hosny, M.; Abd El-Monaem, E.M.; Tamer, T.M.; Omer, A.M. Green synthesis of platinum nanoparticles using *Atriplex halimus* leaves for potential antimicrobial, antioxidant, and catalytic applications. *Arab. J. Chem.* **2022**, *15*, 103517. [CrossRef]
49. Sattar, Z.A.; Mishaal Mohammed, A.; Khalaf, Y.H. Green synthesis of Curcuma longa-mediated Palladium nanoparticles as antioxidant, antimicrobial, and anticancer agents. *Results Chem.* **2024**, *9*, 101675. [CrossRef]
50. Mohamed Isa, E.D.; Aid, S.R.; Rasit Ali, R.; Asako, Y.; Shameli, K.; Jonny, N.F.A.; Zazuli, A.H.; Mohd Taib, S.H.; Yusefi, M. Green synthesis of gold nanoparticles via *Artocarpus odoratissimus* peel extract for potential applications of optical filter and catalytic degradation. *J. King Saud Univ. Sci.* **2024**, *36*, 103209. [CrossRef]
51. Poorshamohammad, C.; Liu, L.; Cheng, X.; Abbas Momtazi-Borojeni, A.; Chai, J. Green synthesis of plant-stabilized Au nanoparticles for the treatment of gastric carcinoma. *Arab. J. Chem.* **2023**, *16*, 104386. [CrossRef]
52. Saka, A.; Shifera, Y.; Jule, L.T.; Badassa, B.; Nagaprasad, N.; Shanmugam, R.; Priyanka Dwarampudi, L.; Seenivasan, V.; Ramaswamy, K. Biosynthesis of TiO_2 nanoparticles by Caricaceae (Papaya) shell extracts for antifungal application. *Sci. Rep.* **2022**, *12*, 15960. [CrossRef] [PubMed]
53. Ansari, A.; Siddiqui, V.U.; Rehman, W.U.; Akram, M.K.; Siddiqi, W.A.; Alosaimi, A.M.; Hussein, M.A.; Rafatullah, M. Green Synthesis of TiO_2 Nanoparticles Using *Acorus calamus* Leaf Extract and Evaluating Its Photocatalytic and In Vitro Antimicrobial Activity. *Catalysts* **2022**, *12*, 181. [CrossRef]
54. Lin, Z.; Weng, X.; Owens, G.; Chen, Z. Simultaneous removal of Pb (II) and rifampicin from wastewater by iron nanoparticles synthesized by a tea extract. *J. Clean. Prod.* **2020**, *242*, 118476. [CrossRef]
55. Mafhala, L.; Khumalo, N.; Zikalala, N.E.; Azizi, S.; Cloete, K.J.; More, G.K.; Kamika, I.A.; Mokrani, T.; Zinatizadeh, A.A.; Maaza, M. Antibacterial and cytotoxicity activity of green synthesized silver nanoparticles using aqueous extract of naartjie (*Citrus unshiu*) fruit peels. *Emerg. Contam.* **2024**, *10*, 100348. [CrossRef]
56. Jaast, S.; Grewal, A. Green synthesis of silver nanoparticles, characterization and evaluation of their photocatalytic dye degradation activity. *Curr. Res. Green Sustain. Chem.* **2021**, *4*, 100195. [CrossRef]
57. Rajeshkumar, S.; Parameswari, R.P.; Sandhiya, D.; Al-Ghanim, K.A.; Nicoletti, M.; Govindarajan, M. Green Synthesis, Characterization and Bioactivity of *Mangifera indica* Seed-Wrapped Zinc Oxide Nanoparticles. *Molecules* **2023**, *28*, 2818. [CrossRef]
58. Bizuayehu, T.; Kassaw, B.; Kendie, M. Green synthesis, characterization, and antibacterial activity investigation of zinc oxide nanoparticles using *Rumex Nervosus Vahl* Leaf extract. *Results Chem.* **2025**, *13*, 102046. [CrossRef]
59. Nzilu, D.M.; Madivoli, E.S.; Makhanu, D.S.; Wanakai, S.I.; Kiprono, G.K.; Kareru, P.G. Green synthesis of copper oxide nanoparticles and its efficiency in degradation of rifampicin antibiotic. *Sci. Rep.* **2023**, *13*, 14030. [CrossRef]
60. Azad, A.; Hussain, S.; Akram, H.; Fida, H.; Iqbal, M.A.; Butt, T.E. Environmentally-friendly synthesis of platinum nanoparticles: Phytochemical, antioxidant, and antimicrobial properties of *Cichorium intybus* in different solvents. *Discov. Plants* **2024**, *1*, 24. [CrossRef]
61. Zhang, Y.; Cheng, S.; Jia, H.; Zhou, J.; Xi, J.; Wang, J.; Chen, X.; Wu, L. Green synthesis of platinum nanoparticles by *Nymphaea tetragona* flower extract and their skin lightening, antiaging effects. *Arab. J. Chem.* **2023**, *16*, 104391. [CrossRef]
62. Shaik, M.R.; Ali, Z.J.Q.; Khan, M.; Kuniyil, M.; Assal, M.E.; Alkhathlan, H.Z.; Al-Warthan, A.; Siddiqui, M.R.H.; Khan, M.; Adil, S.F. Green Synthesis and Characterization of Palladium Nanoparticles Using *Origanum vulgare* L. Extract and Their Catalytic Activity. *Molecules* **2017**, *22*, 165. [CrossRef] [PubMed]
63. Alamier, W.M.; Oteef, M.D.Y.; Bakry, A.M.; Hasan, N.; Ismail, K.S.; Awad, F.S. Green Synthesis of Silver Nanoparticles Using *Acacia ehrenbergiana* Plant Cortex Extract for Efficient Removal of Rhodamine B Cationic Dye from Wastewater and the Evaluation of Antimicrobial Activity. *ACS Omega* **2023**, *8*, 18901–18914. [CrossRef] [PubMed]
64. Şahin Ün, Ş.; Ünlü, A.; Ün, İ.; Ok, S. Green synthesis, characterization and catalytic activity evaluation of palladium nanoparticles facilitated by *Punica granatum* peel extract. *Inorg. Nano-Met. Chem.* **2020**, *51*, 1232–1240. [CrossRef]
65. Wang, Y.; Chen, J.; Bo, Y.; Chen, J.; Liu, Y.; Li, Z.; Yu, C.; Liu, J.; Wang, S. Green synthesis of Au nanoparticles by *Scutellaria barbata* extract for chemo-photothermal anticancer therapy. *Pharmacol. Res. Mod. Chin. Med.* **2024**, *13*, 100536. [CrossRef]

66. Yang, X.; Bao, Y.; Zhou, X.; Zhu, H.; Gao, J. Green chemistry-based synthesis of gold nanoparticles using *Nicotiana plumbaginifolia* and their anticancer properties against cervical cancer. *Arab. J. Chem.* **2024**, *17*, 106029. [CrossRef]
67. Olaoye, A.B.; Owoeye, S.S.; Nwobegu, J.S. Facile green synthesis of plant-mediated selenium nanoparticles (SeNPs) using *Moringa oleifera* leaf and bark extract for targeting α-amylase and α-glucosidase enzymes in diabetes management. *Hybrid Adv.* **2024**, *7*, 100281. [CrossRef]
68. Cittrarasu, V.; Kaliannan, D.; Dharman, K.; Maluventhen, V.; Easwaran, M.; Liu, W.C.; Balasubramanian, B.; Arumugam, M. Green synthesis of selenium nanoparticles mediated from *Ceropegia bulbosa* Roxb extract and its cytotoxicity, antimicrobial, mosquitocidal and photocatalytic activities. *Sci. Rep.* **2021**, *11*, 1032. [CrossRef]
69. Khudier, M.A.A.; Hammadi, H.A.; Atyia, H.T.; Al-Karagoly, H.; Albukhaty, S.; Sulaiman, G.M.; Dewir, Y.H.; Mahood, H.B. Antibacterial activity of green synthesized selenium nanoparticles using *Vaccinium arctostaphylos* (L.) fruit extract. *Cogent Food Agric.* **2023**, *9*, 2245612. [CrossRef]
70. Sulaiman, F.A.; Alwared, A.I. Green synthesis of TiO_2 using *Ocimum basilicum* leaf extract and its application in photocatalytic degradation of amoxicillin residues from aqueous solution. *Desalination Water Treat.* **2022**, *262*, 312–322. [CrossRef]
71. Yitagesu, G.B.; Leku, D.T.; Workneh, G.A. Green Synthesis of TiO_2 Using *Impatiens rothii* Hook.*f.* Leaf Extract for Efficient Removal of Methylene Blue Dye. *ACS Omega* **2023**, *8*, 43999–44012. [CrossRef]
72. Saleh, A.K.; Shaban, A.S.; Diab, M.A.; Debarnot, D.; Elzaref, A.S. Green synthesis and characterization of aluminum oxide nanoparticles using *Phoenix dactylifera* seed extract along with antimicrobial activity, phytotoxicity, and cytological effects on Vicia faba seeds. *Biomass Convers. Biorefin.* **2023**, *14*, 31859–31875. [CrossRef]
73. Sharif, M.S.; Hameed, H.; Waheed, A.; Tariq, M.; Afreen, A.; Kamal, A.; Mahmoud, E.A.; Elansary, H.O.; Saqib, S.; Zaman, W. Biofabrication of Fe_3O_4 Nanoparticles from *Spirogyra hyalina* and *Ajuga bracteosa* and Their Antibacterial Applications. *Molecules* **2023**, *28*, 3403. [CrossRef]
74. Eid, A.M.; Fouda, A.; Hassan, S.E.-D.; Hamza, M.F.; Alharbi, N.K.; Elkelish, A.; Alharthi, A.; Salem, W.M. Plant-Based Copper Oxide Nanoparticles; Biosynthesis, Characterization, Antibacterial Activity, Tanning Wastewater Treatment, and Heavy Metals Sorption. *Catalysts* **2023**, *13*, 348. [CrossRef]
75. Jaishi, D.R.; Ojha, I.; Bhattarai, G.; Baraili, R.; Pathak, I.; Ojha, D.R.; Shrestha, D.K.; Sharma, K.R. Plant-Mediated Synthesis of Zinc Oxide (ZnO) Nanoparticles Using *Alnus Nepalensis* D. Don for Biological Applications. *Heliyon* **2024**, *10*, e39255. [CrossRef] [PubMed]
76. Al Masoudi, L.M.; Alqurashi, A.S.; Abu Zaid, A.; Hamdi, H. Characterization and Biological Studies of Synthesized Titanium Dioxide Nanoparticles from Leaf Extract of *Juniperus phoenicea* (L.) Growing in Taif Region, Saudi Arabia. *Processes* **2023**, *11*, 272. [CrossRef]
77. Muhaymin, A.; Mohamed, H.E.A.; Hkiri, K.; Safdar, A.; Azizi, S.; Maaza, M. Green synthesis of magnesium oxide nanoparticles using *Hyphaene thebaica* extract and their photocatalytic activities. *Sci. Rep.* **2024**, *14*, 20135. [CrossRef]
78. Gingasu, D.; Culita, D.C.; Calderon Moreno, J.M.; Marinescu, G.; Bartha, C.; Oprea, O.; Preda, S.; Chifiriuc, M.C.; Popa, M. Synthesis of $CoFe_2O_4$ through Wet Ferritization Method Using an Aqueous Extract of *Eucalyptus* Leaves. *Coatings* **2023**, *13*, 1250. [CrossRef]
79. Khan, M.; Khan, A.A.; Parveen, A.; Min, K.; Yadav, V.K.; Khan, A.U.; Alam, M. Mitigating the growth of plant pathogenic bacterium, fungi, and nematode by using plant-mediated synthesis of copper oxide nanoparticles (CuO NPs). *Green Chem. Lett. Rev.* **2023**, *16*, 2177520. [CrossRef]
80. Hameed, H.; Waheed, A.; Sharif, M.S.; Saleem, M.; Afreen, A.; Tariq, M.; Kamal, A.; Al-onazi, W.A.; Al Farraj, D.A.; Ahmad, S.; et al. Green Synthesis of Zinc Oxide (ZnO) Nanoparticles from Green Algae and Their Assessment in Various Biological Applications. *Micromachines* **2023**, *14*, 928. [CrossRef]
81. Blessymol, B.; Kalaiselvi, V.; Yasotha, P.; Gopi, S. Comparative Study of Chemically and Green Synthesized Titanium Dioxide Nanoparticles using *Leucas aspera* Leaf Extract. *J. Environ. Nanotechnol.* **2023**, *12*, 10–13. [CrossRef]
82. Babiker, M.E.M. Eco-Environmentally Friendly Green Synthesis and Characterization of Aluminum Oxide Nanoparticles Using Leaf Extract of *Mentha Pulegium*. *Int. J. Chem. Biochem. Sci.* **2024**, *25*, 958–965. [CrossRef]
83. Ali, S.; Sudha, K.G.; Thirumalaivasan, N.; Ahamed, M.; Pandiaraj, S.; Rajeswari, V.D.; Vinayagam, Y.; Thiruvengadam, M.; Govindasamy, R. Green Synthesis of Magnesium Oxide Nanoparticles by Using *Abrus precatorius* Bark Extract and Their Photocatalytic, Antioxidant, Antibacterial, and Cytotoxicity Activities. *Bioengineering* **2023**, *10*, 302. [CrossRef] [PubMed]
84. Kushwaha, P.; Chauhan, P. Facile green synthesis of $CoFe_2O_4$ nanoparticles using hibiscus extract and their application in humidity sensing properties. *Inorg. Nano-Met. Chem.* **2023**, *53*, 664–671. [CrossRef]
85. Mohanaparameswari, S.; Balachandramohan, M.; Kumar, K.G.; Revathy, M.S.; Sasikumar, P.; Rajeevgandhi, C.; Vimalan, M.; Pugazhendhi, S.; Batoo, K.M.; Hussain, S.; et al. Green Synthesis of Silver Oxide Nanoparticles Using *Plectranthus amboinicus* and *Solanum trilobatum* Extracts as an Eco-friendly Approach: Characterization and Antibacterial Properties. *J. Inorg. Organomet. Polym. Mater.* **2024**, *34*, 3191–3211. [CrossRef]

86. Hussain, S.; Ali Muazzam, M.; Ahmed, M.; Ahmad, M.; Mustafa, Z.; Murtaza, S.; Ali, J.; Ibrar, M.; Shahid, M.; Imran, M. Green synthesis of nickel oxide nanoparticles using *Acacia nilotica* leaf extracts and investigation of their electrochemical and biological properties. *J. Taibah Univ. Sci.* **2023**, *17*, 2170162. [CrossRef]
87. Cheah, S.Y.; Tey, L.H.; Aminuzzaman, M.; Phang, Y.K.; Chan, Y.B.; Djearamane, S.; Wong, L.S.; Watanabe, A. Green Synthesis and Characterizations of Chromium Oxide Nanoparticles (Cr_2O_3 NPs) Derived from Pomegranate Husk and its α-Amylase Inhibitory and Antioxidant Properties. *Nano Hybrids Compos.* **2023**, *39*, 51–55. [CrossRef]
88. Omidtorshiz, A.; Benam, M.; Momennezhad, M.; Sabouri, Z.; Darroudi, M. Green synthesis of lead oxide nanoparticles using *Ocimum basilicum* extract: Photocatalytic assessment and cytotoxicity effects. *Inorg. Chem. Commun.* **2023**, *158*, 111575. [CrossRef]
89. Castillo-Saenz, J.; Salomón-Carlos, J.; Beltrán-Partida, E.; Valdez-Salas, B. Eco-Friendly Synthesis of Cerium Oxide Nanoparticles from *Lycium cooperi*. *Reactions* **2025**, *6*, 14. [CrossRef]
90. Shah, I.H.; Manzoor, M.A.; Sabir, I.A.; Ashraf, M.; Gulzar, S.; Chang, L.; Zhang, Y. A green and environmental sustainable approach to synthesis the Mn oxide nanomaterial from *Punica granatum* leaf extracts and its in vitro biological applications. *Environ. Monit. Assess.* **2022**, *194*, 921. [CrossRef]
91. Kolahalam, L.A.; Prasad, K.R.S.; Krishna, P.M.; Supraja, N. *Lawsonia inermis* plant-based cobalt oxide nanoparticles: Synthesis, characterization and their biological studies. *Results Chem.* **2024**, *7*, 101367. [CrossRef]
92. Khan, A.U.; Hussain, T.; Abdullah; Khan, M.A.; Almostafa, M.M.; Younis, N.S.; Yahya, G. Antibacterial and Antibiofilm Activity of Ficus carica-Mediated Calcium Oxide (CaONPs) Phyto-Nanoparticles. *Molecules* **2023**, *28*, 5553. [CrossRef]
93. Fernando, I.; Zhou, Y. Impact of pH on the stability, dissolution and aggregation kinetics of silver nanoparticles. *Chemosphere* **2019**, *216*, 297–305. [CrossRef] [PubMed]
94. Król-Górniak, A.; Railean, V.; Pomastowski, P.; Płociński, T.; Gloc, M.; Dobrucka, R.; Kurzydłowski, K.J.; Buszewski, B. Comprehensive study upon physicochemical properties of bio-ZnO NCs. *Sci. Rep.* **2023**, *13*, 587. [CrossRef] [PubMed]
95. Abdul Karem, L.K.; Ali, A.T. Biosynthesis, Characterization, Adsorption and Antimicrobial studies of Vanadium Oxide Nanoparticles Using *Punica Granatum* Extract. *Baghdad Sci. J.* **2023**, *21*, 0410. [CrossRef]
96. Chelliah, P.; Wabaidur, S.M.; Sharma, H.P.; Majdi, H.S.; Smait, D.A.; Najm, M.A.; Iqbal, A.; Lai, W.-C. Photocatalytic Organic Contaminant Degradation of Green Synthesized ZrO_2 NPs and Their Antibacterial Activities. *Separations* **2023**, *10*, 156. [CrossRef]
97. Esakkirajan, M.; Kumaraguru, S.; Gopinath, K.; Suresh, J. Environmentally sustainable synthesis of MoO_3 nanoparticles: Antibacterial efficacy and biocompatibility assessment. *Chem. Phys. Impact* **2024**, *8*, 100487. [CrossRef]
98. Narasaiah, B.P.; Banoth, P.; Sohan, A.; Mandal, B.K.; Bustamante Dominguez, A.G.; De Los Santos Valladares, L.; Kollu, P. Green Biosynthesis of Tin Oxide Nanomaterials Mediated by Agro-Waste Cotton Boll Peel Extracts for the Remediation of Environmental Pollutant Dyes. *ACS Omega* **2022**, *7*, 15423–15438. [CrossRef]
99. Duraisamy, N.K.; Periakaruppan, R.; Abed, S.A.; Al-Dayan, N.; Dhanasekaran, S.; Aldhayan, S.H.A. Production and Characterization of *Azadirachta indica*-Mediated SiO_2 Nanoparticles and an Evaluation of Their Antioxidant and Antimicrobial Activities. *Silicon* **2023**, *15*, 6663–6671. [CrossRef]
100. Asri, M.; Naghizadeh, A.; Hasani, A.; Mortazavi-Derazkola, S.; Javid, A.; Masoudi, F. Sustainable green synthesis of $ZnFe_2O_4$@ZnO nanocomposite using Oleaster tree bark methanolic extract for photocatalytic degradation of aqueous humic acid in the presence of UVc irradiation. *AQUA-Water Infrastruct. Ecosyst. Soc.* **2023**, *72*, 1800–1814. [CrossRef]
101. Rozina; Ahmad, M.; Ezeji, T.; Emmanuel, O.; Qureshi, N.; Khan, A. Utilization of waste seed oil from *Cestrum nocturnum* as a novel source for cleaner production of biodiesel using green nano-catalyst of antimony oxide. *Fuel* **2024**, *364*, 131124. [CrossRef]
102. Moorthy, P.; Kavitha, H.P. Comparative Evaluation of Bioefficiency and Photocatalytic Activity of Green Synthesized Bismuth Oxide Nanoparticles Using Three Different Leaf Extracts. *ACS Omega* **2023**, *8*, 14752–14765. [CrossRef]
103. Algarni, T.S.; Al-Mohaimeed, A.M.; Abduh, N.A.Y.; Habab, R.A.; Alqahtani, S.M. Green Synthesis of Mixed ZnO-SnO_2 Nanoparticles for Solar-Assisted Degradation of Synthetic Dyes. *Catalysts* **2023**, *13*, 1509. [CrossRef]
104. Maryam, I.; Iqbal, T.; Syed, A.; Bahkali, A.H.; Tehseen, A.; Afsheen, S.; Sultan, M.S. Facile green synthesis of novel tantalum doped tungsten trioxide for photocatalytic degradation: Correlation with COMSOL simulation. *Spectrochim. Acta. A Mol. Biomol. Spectrosc.* **2024**, *314*, 124191. [CrossRef] [PubMed]
105. Lachini, S.A.; Eslami, A. Excellent electrochemical hydrogen storage capabilities of green synthesized $LiCoO_2$ nanoparticles. *Int. J. Hydrogen Energy* **2024**, *51*, 51–60. [CrossRef]
106. Pushparaj, T.L.; Raj, E.F.I.; Rani, E.F.I.; Appadurai, M. Synthesis of biogenic cerium oxide-supported osmium oxide nanoalloy from *Oldenlandia umbellata* L. plant extract for pharmacological applications. *Biomass Convers. Biorefin.* **2023**, *15*, 1327–1341. [CrossRef]
107. Medina-Acosta, M.; Chinchillas-Chinchillas, M.J.; Garrafa-Gálvez, H.E.; Garcia-Maro, C.A.; Rosas-Casarez, C.A.; Lugo-Medina, E.; Luque-Morales, P.A.; Soto-Robles, C.A. Photocatalytic Degradation of Four Organic Dyes Present in Water Using ZnO Nanoparticles Synthesized with Green Synthesis Using Ambrosia ambrosioides Leaf and Root Extract. *Processes* **2024**, *12*, 2456. [CrossRef]

108. Tian, Y.; Luo, J.; Wang, H.; Zaki, H.E.M.; Yu, S.; Wang, X.; Ahmed, T.; Shahid, M.S.; Yan, C.; Chen, J.; et al. Bioinspired Green Synthesis of Silver Nanoparticles Using Three Plant Extracts and Their Antibacterial Activity against Rice Bacterial Leaf Blight Pathogen *Xanthomonas oryzae* pv. Oryzae. *Plants* **2022**, *11*, 2892. [CrossRef]
109. Abdullah; Rahman, A.U.; Faisal, S.; Almostafa, M.M.; Younis, N.S.; Yahya, G. Multifunctional *Spirogyra-hyalina*-Mediated Barium Oxide Nanoparticles (BaONPs): Synthesis and Applications. *Molecules* **2023**, *28*, 6364. [CrossRef]
110. Rokkarukala, S.; Cherian, T.; Ragavendran, C.; Mohanraju, R.; Kamaraj, C.; Almoshari, Y.; Albariqi, A.; Sultan, M.H.; Alsalhi, A.; Mohan, S. One-pot green synthesis of gold nanoparticles using *Sarcophyton crassocaule*, a marine soft coral: Assessing biological potentialities of antibacterial, antioxidant, anti-diabetic and catalytic degradation of toxic organic pollutants. *Heliyon* **2023**, *9*, e14668. [CrossRef]
111. Pawar, M.J.; Gaonar, M.D.; Khajone, A.D.; Malasane, P.R. Green Synthesis of Nb_2O_5 Nanoparticles and Photodegradation of Remazol Yellow RR Dye. *East Afr. Sch. Multidiscip. Bull.* **2023**, *6*, 1–9. [CrossRef]
112. Mfengwana, P.-M.-A.H.; Sone, B.T. Green synthesis and characterization of ruthenium oxide nanoparticles using *Gunnera perpensa* for potential anticancer activity against MCF7 cancer cells. *Sci. Rep.* **2023**, *13*, 22638. [CrossRef] [PubMed]
113. Bharathidasan, P.; Surya, M.; Sravanthy, P.G.; Saravanan, M.; Muthupandian, S. Green Synthesis of Molybdenum Nanoparticles from *Solanum xanthocarpum* and Evaluation of Their Antimicrobial and Antioxidant Activity Against Multidrug-Resistant Wound Isolates. *Cureus* **2024**, *16*, e56760. [CrossRef] [PubMed]
114. Kulkarni, S.C.; Salunke, V.T.; Naeem, S.; Patil, A.V.; Akhtar, M.S.; Ameen, S. Sustainable synthesis of indium oxide nanoparticles via Aloe Vera for gas sensing applications. *Microchem. J.* **2024**, *207*, 111941. [CrossRef]
115. Zyoud, A.; Zyoud, A.H.; Zyoud, S.H.; Nassar, H.; Zyoud, S.H.; Qamhieh, N.; Hajamohideen, A.; Hilal, H.S. Photocatalytic degradation of aqueous methylene blue using ca-alginate supported ZnO nanoparticles: Point of zero charge role in adsorption and photodegradation. *Environ. Sci. Pollut. Res.* **2023**, *30*, 68435–68449. [CrossRef]
116. Abdulqodus, A.N.; Abdulrahman, A.F.; Mostafa, S.H.; Kareem, A.A.; Hamad, S.M.; Ahmed, S.M.; Almessiere, M.A.; Shaikhah, D. Green synthesis of ZnO nanoparticles: Effect of pH on morphology and photocatalytic degradation efficiency. *Appl. Phys. A* **2025**, *131*, 720. [CrossRef]
117. Shrestha, S.; Tiwari, L.; Dhungana, S.; Maharjan, J.; Khadka, D.; Kim, A.A.; Pokhrel, M.R.; Baral, J.; Park, M.; Poudel, B.R. Exploring Photocatalytic, Antimicrobial and Antioxidant Efficacy of Green-Synthesized Zinc Oxide Nanoparticles. *Nanomaterials* **2025**, *15*, 858. [CrossRef]
118. Kamel, A.H.; Abd-Rabboh, H.S.M.; El-Fattah, A.A.; Stambouli, G.B.; Adeida, L. Metal oxides and their composites for the remediation of organic pesticides: Advanced photocatalytic and adsorptive solutions. *RSC Adv.* **2025**, *15*, 6875–6901. [CrossRef]
119. Ghaffar, I.; Hussain, A.; Hasan, A.; Deepanraj, B. Microalgal-induced remediation of wastewaters loaded with organic and inorganic pollutants: An overview. *Chemosphere* **2023**, *320*, 137921. [CrossRef]
120. Rahmani, A.; Shabanloo, A.; Shabanloo, N. A mini-review of recent progress in lead dioxide electrocatalyst for degradation of toxic organic pollutants. *Mater. Today Chem.* **2023**, *27*, 101311. [CrossRef]
121. Sun, N.; Shi, H.; Li, X.; Gao, C.; Liu, R. Combined toxicity of micro/nanoplastics loaded with environmental pollutants to organisms and cells: Role, effects, and mechanism. *Environ. Int.* **2023**, *171*, 107711. [CrossRef]
122. Ahmed, S.F.; Mofijur, M.; Nuzhat, S.; Chowdhury, A.T.; Rafa, N.; Uddin, M.A.; Inayat, A.; Mahlia, T.M.I.; Ong, H.C.; Chia, W.Y.; et al. Recent developments in physical, biological, chemical, and hybrid treatment techniques for removing emerging contaminants from wastewater. *J. Hazard. Mater.* **2021**, *416*, 125912. [CrossRef] [PubMed]
123. Daud, N.M.; Abdullah, S.R.S.; Hasan, H.A.; Ismail, N.; Dhokhikah, Y. Integrated physical-biological treatment system for batik industry wastewater: A review on process selection. *Sci. Total Environ.* **2022**, *819*, 152931. [CrossRef] [PubMed]
124. Dutta, S.; Gupta, B.; Srivastava, S.K.; Gupta, A.K. Recent advances on the removal of dyes from wastewater using various adsorbents: A critical review. *Mater. Adv.* **2021**, *2*, 4497–4531. [CrossRef]
125. Kumar, S.; Yadav, S.; Kataria, N.; Chauhan, A.K.; Joshi, S.; Gupta, R.; Kumar, P.; Chong, J.W.R.; Khoo, K.S.; Show, P.L. Recent Advancement in Nanotechnology for the Treatment of Pharmaceutical Wastewater: Sources, Toxicity, and Remediation Technology. *Curr. Pollut. Rep.* **2023**, *9*, 110–142. [CrossRef]
126. El Alouani, M.; Saufi, H.; Aouan, B.; Bassam, R.; Alehyen, S.; Rachdi, Y.; El Hadki, H.; El Hadki, A.; Mabrouki, J.; Belaaouad, S.; et al. A comprehensive review of synthesis, characterization, and applications of aluminosilicate materials-based geopolymers. *Environ. Adv.* **2024**, *16*, 100524. [CrossRef]
127. Bassam, A.; Bassam, R.; El Alouani, M.; Rachdi, Y.; Saufi, H.; Belaaouad, S. Synthesis of geopolymer powder and beads based on red clay waste for the adsorption of methyl orange dye from aqueous solutions: Characterization, application of response surface methodology, and cost analysis. *Sustain. Chem. Pharm.* **2024**, *39*, 101575. [CrossRef]
128. Bassam, R.; El Alouani, M.; Maissara, J.; Jarmouni, N.; Belhabra, M.; El Mahi Chbihi, M.; Belaaouad, S. Investigation of competitive adsorption and desorption of heavy metals from aqueous solution using raw rock: Characterization kinetic, isotherm, and thermodynamic. *Mater. Today Proc.* **2022**, *52*, 158–165. [CrossRef]

129. Farias, K.C.S.; Guimarães, R.C.A.; Oliveira, K.R.W.; Nazário, C.E.D.; Ferencz, J.A.P.; Wender, H. Banana Peel Powder Biosorbent for Removal of Hazardous Organic Pollutants from Wastewater. *Toxics* **2023**, *11*, 664. [CrossRef]
130. Saravanan, A.; Karishma, S.; Kumar, P.S.; Thamarai, P.; Yaashikaa, P.R. Recent insights into mechanism of modified bio-adsorbents for the remediation of environmental pollutants. *Environ. Pollut.* **2023**, *339*, 122720. [CrossRef]
131. Bakhtiari, S.; Salari, M.; Shahrashoub, M.; Zeidabadinejad, A.; Sharma, G.; Sillanpää, M. A Comprehensive Review on Green and Eco-Friendly Nano-Adsorbents for the Removal of Heavy Metal Ions: Synthesis, Adsorption Mechanisms, and Applications. *Curr. Pollut. Rep.* **2024**, *10*, 1–39. [CrossRef]
132. Hoseinpour, V.; Ghaemi, N. Green synthesis of manganese nanoparticles: Applications and future perspective—A review. *J. Photochem. Photobiol. B* **2018**, *189*, 234–243. [CrossRef]
133. Şahin, M.; Arslan, Y.; Tomul, F.; Akgül, F.; Akgül, R. Green synthesis of metal nanoparticles from Codium macroalgae for wastewater pollutants removal by adsorption. *CLEAN–Soil Air Water* **2024**, *52*, 2300187. [CrossRef]
134. Mallakpour, S.; Tabesh, F. Green and plant-based adsorbent from tragacanth gum and carboxyl-functionalized carbon nanotube hydrogel bionanocomposite for the super removal of methylene blue dye. *Int. J. Biol. Macromol.* **2021**, *166*, 722–729. [CrossRef] [PubMed]
135. Hamid, A.; Ahmad, S.R.; Ali, F.; Iqbal, M.S.; Nazir, R. Treatment of pesticides (chlorpyrifos and tebuconazole) and Congo red dye by the application of green synthesized palladium nanoparticles using hemicellulose obtained from *Lallemantia royleana* seed. *Environ. Dev. Sustain.* **2024**, *26*, 579–599. [CrossRef]
136. Tariq, M.S.; Imran, M.; Din, S.U.; Murtaza, B.; Naeem, M.A.; Amjad, M.; Shah, N.S.; Khalid, M.S.; Abdel-Maksoud, M.A.; Alfuraydi, A.A.; et al. Magnetic nanocomposite of maize offal biomass for effective sequestration of Congo red and methyl orange dyes from contaminated water: Modeling, kinetics and reusability. *Int. J. Phytoremediat.* **2024**, *26*, 975–992. [CrossRef] [PubMed]
137. Manzoor, K.; Batool, M.; Naz, F.; Nazar, M.F.; Hameed, B.H.; Zafar, M.N. A comprehensive review on application of plant-based bioadsorbents for Congo red removal. *Biomass Convers. Biorefin.* **2024**, *14*, 4511–4537. [CrossRef]
138. Bhushan, D.; Shoran, S.; Kumar, R.; Gupta, R. Plant biomass-based nanoparticles for remediation of contaminants from water ecosystems: Recent trends, challenges, and future perspectives. *Chemosphere* **2024**, *365*, 143340. [CrossRef]
139. Rani, M.; Shanker, U. Removal of chlorpyrifos, thiamethoxam, and tebuconazole from water using green synthesized metal hexacyanoferrate nanoparticles. *Environ. Sci. Pollut. Res.* **2018**, *25*, 10878–10893. [CrossRef]
140. Jiang, H.; Sathiyavimal, S.; Cai, L.; Devanesan, S.; Sayed, S.R.M.; Jhanani, G.K.; Lin, J. Tulsi (*Ocimum sanctum*) mediated Co nanoparticles with their anti-inflammatory, anti-cancer, and methyl orange dye adsorption properties. *Environ. Res.* **2023**, *236*, 116749. [CrossRef]
141. Kashyap, K.; Moharana, M.; Pattanayak, S.K.; Khan, F. Adsorptive removal of heavy metal ions from aqueous solution by using green synthesized copper oxide nanoparticles. *Inorg. Nano-Met. Chem.* **2024**, *55*, 493–504. [CrossRef]
142. Yadav, J.; Rani, M.; Shanker, U.; Sillanpaa, M. Forging the advances of iron-based nanomaterials by functionalizing charge carriers regions for eradication of heavy metal ion contamination. *Inorg. Chem. Commun.* **2024**, *164*, 112440. [CrossRef]
143. Parlayıcı, Ş. Sustainable Synthesis of Silver Nanoparticles Using Plant-Based Waste Biomass for the Removal of Cationic Dyes—A Review. *Fine Chem. Eng.* **2024**, *5*, 414–451. [CrossRef]
144. Nasrollahzadeh, M.; Sajjadi, M.; Dadashi, J.; Ghafuri, H. Pd-based nanoparticles: Plant-assisted biosynthesis, characterization, mechanism, stability, catalytic and antimicrobial activities. *Adv. Colloid Interface Sci.* **2020**, *276*, 102103. [CrossRef] [PubMed]
145. Singh, S.; Naik, T.S.S.K.; Thamaraiselvan, C.; Behera, S.K.; Pavithra, N.; Nath, B.; Dwivedi, P.; Singh, J.; Ramamurthy, P.C. Applicability of New Sustainable and Efficient Green Metal-Based Nanoparticles for Removal of Cr (VI): Adsorption Anti-Microbial, and DFT Studies. *Environ. Pollut.* **2023**, *320*, 121105. [CrossRef]
146. Mphuthi, B.R.; Thabede, P.M.; Monapathi, M.E.; Shooto, N.D. Hemp seed nanoparticle composites for removing lead, methylene blue, and ibuprofen from an aqueous solution and their antimicrobial towards *Escherichia coli* and *Staphylococcus aureus*. *Case Stud. Chem. Environ. Eng.* **2023**, *8*, 100436. [CrossRef]
147. Malarvizhi, T.; Muthukumaran, K.; Thamarai, P. A green solution for eliminating methylene blue and crystal violet dyes using eco-friendly zinc oxide nanoparticles synthesized from *Dracaena trifasciata*. *Desalination Water Treat.* **2024**, *320*, 100699. [CrossRef]
148. Silveira, C.; Shimabuku, Q.L.; Silva, M.F.; Bergamasco, R. Iron-oxide nanoparticles by the green synthesis method using *Moringa oleifera* leaf extract for fluoride removal. *Environ. Technol.* **2018**, *39*, 2926–2936. [CrossRef]
149. Manquián-Cerda, K.; Cruces, E.; Rubio, M.A.; Reyes, C.; Arancibia-Miranda, N. Preparation of nanoscale iron (oxide, oxyhydroxides and zero-valent) particles derived from blueberries: Reactivity, characterization and removal mechanism of arsenate. *Ecotoxicol. Environ. Saf.* **2017**, *145*, 69–77. [CrossRef]
150. Rashid, I.; Salman, S.; Mohammed, P.K.; Mahdi, Y. Green Synthesis of Nickle Oxide Nanoparticles for Adsorption of Dyes. *Sains Malays.* **2022**, *51*, 533–546. [CrossRef]
151. Fatima, B.; Siddiqui, S.I.; Nirala, R.K.; Vikrant, K.; Kim, K.-H.; Ahmad, R.; Chaudhry, S.A. Facile green synthesis of ZnO–$CdWO_4$ nanoparticles and their potential as adsorbents to remove organic dye. *Environ. Pollut.* **2021**, *271*, 116401. [CrossRef]

152. Abdulla, N.K.; Siddiqui, S.I.; Tara, N.; Hashmi, A.A.; Chaudhry, S.A. Psidium guajava leave-based magnetic nanocomposite γ-Fe_2O_3@GL: A green technology for methylene blue removal from water. *J. Environ. Chem. Eng.* **2019**, *7*, 103423. [CrossRef]
153. Tran, T.V.; Nguyen, D.T.C.; Kumar, P.S.; Din, A.T.M.; Qazaq, A.S.; Vo, D.-V.N. Green synthesis of Mn_3O_4 nanoparticles using *Costus woodsonii* flowers extract for effective removal of malachite green dye. *Environ. Res.* **2022**, *214*, 113925. [CrossRef] [PubMed]
154. Vinayagam, R.; Kandati, S.; Murugesan, G.; Goveas, L.C.; Baliga, A.; Pai, S.; Varadavenkatesan, T.; Kaviyarasu, K.; Selvaraj, R. Bioinspiration synthesis of hydroxyapatite nanoparticles using eggshells as a calcium source: Evaluation of Congo red dye adsorption potential. *J. Mater. Res. Technol.* **2023**, *22*, 169–180. [CrossRef]
155. Panneerselvam, A.; Velayutham, J.; Ramasamy, S. Green synthesis of TiO_2 nanoparticles prepared from *Phyllanthus niruri* leaf extract for dye adsorption and their isotherm and kinetic studies. *IET Nanobiotechnol.* **2021**, *15*, 164–172. [CrossRef] [PubMed]
156. Alizadeh, N.; Shariati, S.; Besharati, N. Adsorption of Crystal Violet and Methylene Blue on Azolla and Fig Leaves Modified with Magnetite Iron Oxide Nanoparticles. *Int. J. Environ. Res.* **2017**, *11*, 197–206. [CrossRef]
157. Turna, T.; Solmaz, A.; Baran, A. Green Synthesis Study: Adsorption of Congo Red Dye with Selenium Nanoparticles Obtained from *Prunus armeniaca* L. Leaf Waste. *ChemistrySelect* **2024**, *9*, e202403106. [CrossRef]
158. Pai, S.; Kini, S.M.; Narasimhan, M.K.; Pugazhendhi, A.; Selvaraj, R. Structural characterization and adsorptive ability of green synthesized Fe_3O_4 nanoparticles to remove Acid blue 113 dye. *Surf. Interfaces* **2021**, *23*, 100947. [CrossRef]
159. Doondani, P.; Panda, D.; Gomase, V.; Peta, K.R.; Jugade, R. Novel Chitosan-ZnO nanocomposites derived from Nymphaeaceae fronds for highly efficient removal of Reactive Blue 19, Reactive Orange 16, and Congo Red dyes. *Environ. Res.* **2024**, *247*, 118228. [CrossRef]
160. Lotfollahzadeh, R.; Yari, M.; Sedaghat, S.; Delbari, A.S. Biosynthesis and characterization of silver nanoparticles for the removal of amoxicillin from aqueous solutions using *Oenothera biennis* water extract. *J. Nanostruct. Chem.* **2021**, *11*, 693–706. [CrossRef]
161. Ghosh, N.; Sen, S.; Biswas, G.; Saxena, A.; Haldar, P.K. Adsorption and Desorption Study of Reusable Magnetic Iron Oxide Nanoparticles Modified with *Justicia adhatoda* Leaf Extract for the Removal of Textile Dye and Antibiotic. *Water. Air. Soil Pollut.* **2023**, *234*, 202. [CrossRef]
162. Guirguis, H.A.; Youssef, N.; William, M.; Abdel-Dayem, D.; El-Sayed, M.M.H. Bioinspired *Stevia rebaudiana* Green Zinc Oxide Nanoparticles for the Adsorptive Removal of Antibiotics from Water. *ACS Omega* **2024**, *9*, 12881–12895. [CrossRef] [PubMed]
163. Ali, I.; AL-Othman, Z.A.; Alwarthan, A. Green synthesis of functionalized iron nanoparticles and molecular liquid phase adsorption of ametryn from water. *J. Mol. Liq.* **2016**, *221*, 1168–1174. [CrossRef]
164. Kar, A.; Deole, S.; Gadratagi, B.G.; Patil, N.; Guru-Pirasanna-Pandi, G.; Mahapatra, B.; Adak, T. Facile synthesis of novel magnesium oxide nanoparticles for pesticide sorption from water. *Environ. Sci. Pollut. Res.* **2023**, *30*, 101467–101482. [CrossRef] [PubMed]
165. Shad, S.; Bashir, N.; Lynch, I. Low-cost iron nanoparticles for remediation of agricultural pollution: Adsorption of herbicides bromoxynil and paraquat. *Environ. Sci. Nano* **2024**, *11*, 3774–3789. [CrossRef]
166. Diel, J.C.; Franco, D.S.P.; Igansi, A.V.; Cadaval, T.R.S.; Pereira, H.A.; Nunes, I.D.S.; Basso, C.W.; Alves, M.D.C.M.; Morais, J.; Pinto, D.; et al. Green synthesis of carbon nanotubes impregnated with metallic nanoparticles: Characterization and application in glyphosate adsorption. *Chemosphere* **2021**, *283*, 131193. [CrossRef]
167. Dar, A.; Ashfaq, H.; Sherin, L.; Salman, M.; Anwar, J. Synthesis, Characterization and Applications of Plant Based Silver Nanocomposites for Effective Removal of Chromium (VI) from Contaminated Water. *Mater. Innovations* **2021**, *1*, 56–63.
168. Alothman, Z.A.; Habila, M.A.; Moshab, M.S.; Al-Qahtani, K.M.; AlMasoud, N.; Al-Senani, G.M.; Al-Kadhi, N.S. Fabrication of renewable palm-pruning leaves based nano-composite for remediation of heavy metals pollution. *Arab. J. Chem.* **2020**, *13*, 4936–4944. [CrossRef]
169. Kamath, V.; Chandra, P.; Jeppu, G.P. Comparative study of using five different leaf extracts in the green synthesis of iron oxide nanoparticles for removal of arsenic from water. *Int. J. Phytoremediat.* **2020**, *22*, 1278–1294. [CrossRef]
170. Deshmukh, P.; Sar, S.K.; Jindal, M.K.; Ray, T. Magnetite based green bio composite for uranium exclusion from aqueous solution. *J. Radioanal. Nucl. Chem.* **2023**, *332*, 297–310. [CrossRef]
171. Sudhakar, M.; Reddy, V.S.; Mekala, S.; Ravindhranath, K. Effective Bio-Sorbents for the Simultaneous Removal of Cadmium and Mercury Ions from Polluted Waters: Based on Ficus Panda Plant Areal Roots Active Carbon, Nano Particle of SnO_2 and Al-Alginate Beads. *J. Polym. Environ.* **2023**, *31*, 2032–2054. [CrossRef]
172. Gindaba, G.T.; Demsash, H.D.; Jayakumar, M. Green synthesis, characterization, and application of metal oxide nanoparticles for mercury removal from aqueous solution. *Environ. Monit. Assess.* **2022**, *195*, 9. [CrossRef] [PubMed]
173. Rong, K.; Li, X.; Yang, Q.; Li, R.; Zhang, Z.; Zou, M.; Zheng, H.; Liu, J. Removal of aqueous vanadium(V) by green synthesized iron nanoparticles supported on corn straw biochar. *J. Ind. Eng. Chem.* **2023**, *120*, 170–181. [CrossRef]
174. Kashyap, K.; Khan, F.; Verma, D.K.; Agrawal, S. Effective removal of uranium from aqueous solution by using cerium oxide nanoparticles derived from citrus limon peel extract. *J. Radioanal. Nucl. Chem.* **2023**, *332*, 2435–2445. [CrossRef]
175. Cao, D.; Jin, X.; Gan, L.; Wang, T.; Chen, Z. Removal of phosphate using iron oxide nanoparticles synthesized by eucalyptus leaf extract in the presence of CTAB surfactant. *Chemosphere* **2016**, *159*, 23–31. [CrossRef]

176. Rawat, S.; Samreen, K.; Nayak, A.K.; Singh, J.; Koduru, J.R. Fabrication of iron nanoparticles using Parthenium: A combinatorial eco-innovative approach to eradicate crystal violet dye and phosphate from the aqueous environment. *Environ. Nanotechnol. Monit. Manag.* **2021**, *15*, 100426. [CrossRef]
177. Soliemanzadeh, A.; Fekri, M.; Bakhtiary, S.; Mehrizi, M.H. Biosynthesis of iron nanoparticles and their application in removing phosphorus from aqueous solutions. *Chem. Ecol.* **2016**, *32*, 286–300. [CrossRef]
178. Xu, Q.; Li, W.; Ma, L.; Cao, D.; Owens, G.; Chen, Z. Simultaneous removal of ammonia and phosphate using green synthesized iron oxide nanoparticles dispersed onto zeolite. *Sci. Total Environ.* **2020**, *703*, 135002. [CrossRef]
179. Soliemanzadeh, A.; Fekri, M. Synthesis of green and ecofriendly iron nanoparticles using plant part extracts: Application on the removal of phosphorus from aqueous media. *Inorg. Nano-Met. Chem.* **2021**, *51*, 340–351. [CrossRef]
180. Wang, L.; Zhang, J.-G.; Sha, H.-Y.; Wang, Y.-R.; Wang, H.-Y.; Zhu, G.-C.; Lu, Y.-Z. Lanthanum-quaternized chitosan-modified zeolite for long-lasting operation of constructed wetland: A bifunctional strategy for simultaneous phosphorus removal and microbial clogging mitigation. *Water Res.* **2026**, *288*, 124688. [CrossRef]
181. Sun, Y.; Liu, J.; Chen, J.; Li, G.; Liang, M.; Zhang, M. Soft/hard interface design of bismuth nanodots embedded in $Ti_3C_2T_x$ MXene for highly efficient dechlorination battery deionization. *Desalination* **2025**, *614*, 119183. [CrossRef]
182. Wang, L.; Shao, Z.; Du, H.; Sun, W.; Wang, X.; Sun, H. Progress of plant biomass nanomaterials in the adsorption and removal of environmental pollutants. *Ind. Crops Prod.* **2025**, *235*, 121529. [CrossRef]
183. Bouzekri, O.; Gamouz, S.E.; Ed-Dra, A.; Moussout, H.; Dehmani, Y.; Ziyat, H.; Idrissi, M.E.; Choukrad, M.; Abouarnadasse, S. Green Synthesis of Nickel and Copper Nanoparticles Doped with Silver from Hammada scoparia Leaf Extract and Evaluation of Their Potential to Inhibit Microorganisms and to Remove Dyes from Aqueous Solutions. *Sustainability* **2023**, *15*, 1541. [CrossRef]
184. Akhi, A.A.; Hasan, A.; Saha, N.; Howlader, S.; Bhattacharjee, S.; Dey, K.; Ullah, A.K.M.A.; Bhuiyan, F.R.; Chakraborty, A.K.; Akhtar, U.S.; et al. *Ophiorrhiza mungos*-Mediated Silver Nanoparticles as Effective and Reusable Adsorbents for the Removal of Methylene Blue from Water. *ACS Omega* **2024**, *9*, 4324–4338. [CrossRef] [PubMed]
185. Jawed, A.; Golder, A.K.; Pandey, L.M. Synthesis of iron oxide nanoparticles mediated by *Camellia sinensis* var. Assamica for Cr (VI) adsorption and detoxification. *Bioresour. Technol.* **2023**, *376*, 128816. [CrossRef]
186. Yu, N.; Zeng, X.; Ma, X.; Sun, Y.; Wang, Y.; Chen, B.; Luo, Z.; Dong, C.; Shen, K.; Wu, J. Preparation of Ce-Fe_2O_3/Al_2O_3 catalyst for simultaneous degradation of benzodiacetone and reduction of Cr (VI) by electro-Fenton process: Performance, mechanism, degradation pathways. *J. Alloys Compd.* **2025**, *1045*, 184745. [CrossRef]
187. Khan, T.; Ullah, N.; Khan, M.A.; Mashwani, Z.-R.; Nadhman, A. Plant-based gold nanoparticles; a comprehensive review of the decade-long research on synthesis, mechanistic aspects and diverse applications. *Adv. Colloid Interface Sci.* **2019**, *272*, 102017. [CrossRef]
188. Yadav, S.; Yadav, A.; Bagotia, N.; Sharma, A.K.; Kumar, S. Adsorptive potential of modified plant-based adsorbents for sequestration of dyes and heavy metals from wastewater—A review. *J. Water Process Eng.* **2021**, *42*, 102148. [CrossRef]
189. Van Thuan, D.; Ngo, H.L.; Thi, H.P.; Chu, T.T.H. Photodegradation of hazardous organic pollutants using titanium oxides-based photocatalytic: A review. *Environ. Res.* **2023**, *229*, 116000. [CrossRef]
190. Yaseen, D.A.; Scholz, M. Textile dye wastewater characteristics and constituents of synthetic effluents: A critical review. *Int. J. Environ. Sci. Technol.* **2019**, *16*, 1193–1226. [CrossRef]
191. Nguyen, N.T.T.; Nguyen, L.M.; Nguyen, T.T.T.; Liew, R.K.; Nguyen, D.T.C.; Tran, T.V. Recent advances on botanical biosynthesis of nanoparticles for catalytic, water treatment and agricultural applications: A review. *Sci. Total Environ.* **2022**, *827*, 154160. [CrossRef]
192. Singh, A.K. A review on plant extract-based route for synthesis of cobalt nanoparticles: Photocatalytic, electrochemical sensing and antibacterial applications. *Curr. Res. Green Sustain. Chem.* **2022**, *5*, 100270. [CrossRef]
193. Marimuthu, S.; Antonisamy, A.J.; Malayandi, S.; Rajendran, K.; Tsai, P.-C.; Pugazhendhi, A.; Ponnusamy, V.K. Silver nanoparticles in dye effluent treatment: A review on synthesis, treatment methods, mechanisms, photocatalytic degradation, toxic effects and mitigation of toxicity. *J. Photochem. Photobiol. B* **2020**, *205*, 111823. [CrossRef] [PubMed]
194. Ali, M.H.H.; Abdelkarim, M.S.; Al-Afify, A.D.G. Characterization and photodegradation of methylene blue dye using bio-synthesized cerium oxide nanoparticles with *Spirulina platensis* extract. *Discov. Appl. Sci.* **2024**, *6*, 94. [CrossRef]
195. Selvi, M.; Balasubramaniyan, S.; Jagatheesan, R. Sphere-like Nb_2O_5 nanoparticles by waste Brassica oleracea leaf extract for lead removal and photocatalytic degradation of methylene blue dye. *J. Indian Chem. Soc.* **2024**, *101*, 101377. [CrossRef]
196. Negash, A.; Derseh, L.M.; Tedla, A.; Yassin, J.M. Eco-friendly synthesis of CuO/Bi_2O_3 nanocomposite for efficient photocatalytic degradation of rhodamine B dye. *Sci. Rep.* **2024**, *14*, 23393. [CrossRef]
197. Prescilio, I.C.; Abe, S.H.M.; Bakuzis, A.F.; Vasconcelos, L.G.; Thaines, E.H.N.S.; de Morais, L.H.; Silva, V.C.P.; Freitas, R.G.; Jacinto, M.J. Biosynthesis of enhanced magnetic iron Oxide@ZnO nanocomposites with incorporated Ni species for the photodegradation of dyes. *Appl. Surf. Sci.* **2025**, *702*, 163385. [CrossRef]
198. Bayahia, H. *Schinus molle* extract mediated green synthesis of iron niobate photocatalyst for the degradation of methyl orange dye under visible light. *J. Saudi Chem. Soc.* **2024**, *28*, 101876. [CrossRef]

199. Arif, I.; Muneer, I.; Abbas, A.; Amanuallah, T.; Yasmeen, F.; Ali, D.; Hanif, M. Eco-friendly synthesis of Nb-doped Fe_2O_3 nanoparticles using *Acacia nilotica* leaf extract for photocatalytic and antibacterial applications. *Optik* **2025**, *329*, 172334. [CrossRef]
200. Safitri, S.E.; Yulizar, Y. Facile green preparation of Y_2O_3 decorated with $ZnFe_2O_4$ using *Citrus limon* (L.) osbeck leaf extract for photocatalytic degradation of malachite green. *Appl. Surf. Sci. Adv.* **2024**, *21*, 100589. [CrossRef]
201. Hasan, G.G.; Laouini, S.E.; Khelef, A.; Mohammed, H.A.; Althamthami, M.; Meneceur, S.; Alharthi, F.; Alshareef, S.A.; Menaa, F. Efficient treatment of oily wastewater, antibacterial activity, and photodegradation of organic dyes using biosynthesized Ag@Fe_3O_4 nanocomposite. *Bioprocess Biosyst. Eng.* **2024**, *47*, 75–90. [CrossRef]
202. Aouan, B.; El Alouani, M.; Bassam, R.; Bassam, A.; Rachdi, Y.; Alehyen, S.; Belaaouad, S.; Saufi, H. The application of nanoparticle-doped geopolymers as innovative photocatalysts for degrading organic pollutants in aquatic environments: A comprehensive review. *J. Mol. Struct.* **2025**, *1338*, 142303. [CrossRef]
203. Shahid-ul-Islam; Bairagi, S.; Kamali, M.R. Review on green biomass-synthesized metallic nanoparticles and composites and their photocatalytic water purification applications: Progress and perspectives. *Chem. Eng. J. Adv.* **2023**, *14*, 100460. [CrossRef]
204. Kaur, M.; Gautam, A.; Guleria, P.; Singh, K.; Kumar, V. Green synthesis of metal nanoparticles and their environmental applications. *Curr. Opin. Environ. Sci. Health* **2022**, *29*, 100390. [CrossRef]
205. Saim, A.K.; Adu, P.C.O.; Amankwah, R.K.; Oppong, M.N.; Darteh, F.K.; Mamudu, A.W. Review of catalytic activities of biosynthesized metallic nanoparticles in wastewater treatment. *Environ. Technol. Rev.* **2021**, *10*, 111–130. Available online: https://www.tandfonline.com/doi/abs/10.1080/21622515.2021.1893831 (accessed on 2 November 2024). [CrossRef]
206. Joseph, A.; Vijayanandan, A. Photocatalysts synthesized via plant mediated extracts for degradation of organic compounds: A review of formation mechanisms and application in wastewater treatment. *Sustain. Chem. Pharm.* **2021**, *22*, 100453. [CrossRef]
207. Chong, M.N.; Jin, B.; Chow, C.W.K.; Saint, C. Recent developments in photocatalytic water treatment technology: A review. *Water Res.* **2010**, *44*, 2997–3027. [CrossRef]
208. Mutukwa, D.; Taziwa, R.T.; Khotseng, L. A Review of Plant-Mediated ZnO Nanoparticles for Photodegradation and Antibacterial Applications. *Nanomaterials* **2024**, *14*, 1182. [CrossRef]
209. Herrmann, J.-M. Heterogeneous photocatalysis: State of the art and present applications In honor of Pr. R.L. Burwell Jr. (1912–2003), Former Head of Ipatieff Laboratories, Northwestern University, Evanston (Ill). *Top. Catal.* **2005**, *34*, 49–65. [CrossRef]
210. Mousa, S.A.; Wissa, D.A.; Hassan, H.H.; Ebnalwaled, A.A.; Khairy, S.A. Enhanced photocatalytic activity of green synthesized zinc oxide nanoparticles using low-cost plant extracts. *Sci. Rep.* **2024**, *14*, 16713. [CrossRef]
211. Zango, Z.U.; Ibnaouf, K.H.; Garba, A.; Aldaghri, O.; Wadi, I.A.; Hosseini-Bandegharaei, A.; Baigenzhenov, O. Advances in green synthesis, modification strategies, and photocatalytic application of metal oxide nanoparticles for organic pollutants degradation: A comprehensive and in-depth review. *J. Mol. Liq.* **2025**, *428*, 127497. [CrossRef]
212. Karanwal, N.; Verma, D.; Butolia, P.; Kim, S.M.; Kim, J. One-pot direct conversion of levulinic acid into high-yield valeric acid over a highly stable bimetallic Nb-Cu/Zr-doped porous silica catalyst. *Green Chem.* **2020**, *22*, 766–787. [CrossRef]
213. Jalviste, E.; Ohta, N. Theoretical foundation of electroabsorption spectroscopy: Self-contained derivation of the basic equations with the direction cosine method and the Euler angle method. *J. Photochem. Photobiol. C Photochem. Rev.* **2007**, *8*, 30–46. [CrossRef]
214. Baniamerian, H.; Tsapekos, P.; Alvarado-Morales, M.; Shokrollahzadeh, S.; Safavi, M.; Angelidaki, I. Anti-algal activity of Fe_2O_3–TiO_2 photocatalyst on *Chlorella vulgaris* species under visible light irradiation. *Chemosphere* **2020**, *242*, 125119. [CrossRef] [PubMed]
215. Puri, A.; Mohite, P.; Ansari, Y.; Mukerjee, N.; Alharbi, H.M.; Upaganlawar, A.; Thorat, N. Plant-derived selenium nanoparticles: Investigating unique morphologies, enhancing therapeutic uses, and leading the way in tailored medical treatments. *Mater. Adv.* **2024**, *5*, 3602–3628. [CrossRef]
216. Batterjee, M.G.; Nabi, A.; Kamli, M.R.; Alzahrani, K.A.; Danish, E.Y.; Malik, M.A. Green Hydrothermal Synthesis of Zinc Oxide Nanoparticles for UV-Light-Induced Photocatalytic Degradation of Ciprofloxacin Antibiotic in an Aqueous Environment. *Catalysts* **2022**, *12*, 1347. [CrossRef]
217. Bag, S.S.; Sinha, S.; Banerjee, A.; Golder, A. Simultaneous sensing and photocatalytic degradation to free water from toxic dye pollutants for possible agricultural and household applications: Role of generated holes and hydroxyl radicals. *J. Environ. Chem. Eng.* **2022**, *10*, 108919. [CrossRef]
218. Govindhan, M. Green Synthesis of Structural and Bandgap Engineering Nickel Oxide Nanostructure for Visible Light Photocatalyst. *Catal. Lett.* **2025**, *155*, 239. [CrossRef]
219. Nosaka, Y.; Nosaka, A.Y. Generation and Detection of Reactive Oxygen Species in Photocatalysis. *Chem. Rev.* **2017**, *117*, 11302–11336. [CrossRef]
220. Bognár, S.; Jovanović, D.; Despotović, V.; Jakšić, S.; Panić, S.; Milanović, M.; Finčur, N.; Putnik, P.; Merkulov, D.Š. Advanced Photocatalytic Degradation of Organic Pollutants Using Green Tea-Based ZnO Nanomaterials Under Simulated Solar Irradiation in Agri-Food Wastewater. *Foods* **2025**, *14*, 622. [CrossRef]

221. Sarkar, D.K.; Selvanathan, V.; Mottakin, M.; Islam, M.A.; Almohamadi, H.; Alharthi, N.H.; Akhtaruzzaman, M. Phytochemicals assisted green synthesis of copper oxide/cobalt oxide as efficient electrocatalyst for oxygen evolution reaction. *Int. J. Hydrogen Energy* **2024**, *51*, 700–712. [CrossRef]
222. Xu, M.; Huang, H.; Li, N.; Li, F.; Wang, D.; Luo, Q. Occurrence and ecological risk of pharmaceuticals and personal care products (PPCPs) and pesticides in typical surface watersheds, China. *Ecotoxicol. Environ. Saf.* **2019**, *175*, 289–298. [CrossRef]
223. Ahmaruzzaman, M. Biochar based nanocomposites for photocatalytic degradation of emerging organic pollutants from water and wastewater. *Mater. Res. Bull.* **2021**, *140*, 111262. [CrossRef]
224. Zanbili, F.; Marjani, A.P. Innovative green and bio-based approaches for photosensitive nanoparticle synthesis: A review on methodologies, characterization, and applications. *Micro Nano Syst. Lett.* **2025**, *13*, 3. [CrossRef]
225. Gizachew, D.G.; Jiru, E.B.; Tekle'Ab, T.; Bayisa, Y.M.; Bullo, T.A. Green synthesis of Silver-iron-zinc oxides nanocomposite via *Embelia schimperia* leaf extract for photo-degradation of antibiotic drug from pharmaceutical wastewater. *Appl. Water Sci.* **2024**, *14*, 210. [CrossRef]
226. Rana, G.; Dhiman, P.; Sharma, J.; Kumar, A.; Sharma, G. Photocatalytic degradation of amoxicillin using TM doped ZnO nanoparticles synthesized from orange peel extract. *Inorg. Chem. Commun.* **2023**, *158*, 111596. [CrossRef]
227. Balarabe, B.Y. Green synthesis of gold-titania nanoparticles for sustainable ciprofloxacin removal and phytotoxicity evaluation on aquatic plant growth. *Hybrid Adv.* **2023**, *4*, 100107. [CrossRef]
228. Golmohammadi, M.; Hanafi-Bojd, H.; Shiva, M. Photocatalytic degradation of ciprofloxacin antibiotic in water by biosynthesized silica supported silver nanoparticles. *Ceram. Int.* **2023**, *49*, 7717–7726. [CrossRef]
229. Aggarwal, D.; Bhavika; Kaur, M.; Bansal, S.; Singhal, S. Fabrication of eco-friendly $NiFe_2O_4$ nanocatalysts via plant extract-mediated synthesis: Kinetic and mechanistic insights into photocatalytic degradation of an anthraquinone dye and tetracycline antibiotic. *J. Mol. Struct.* **2025**, *1319*, 139365. [CrossRef]
230. Nguyen, N.T.T.; Phan, A.N.Q.; Tran, T.V.; Nguyen, T.T.T. *Morinda citrifolia* fruit extract-mediated synthesis of ZnO and Ag/ZnO nanoparticles for photocatalytic degradation of tetracycline. *Environ. Res.* **2025**, *273*, 121209. [CrossRef]
231. Mahlaule-Glory, L.M.; Mapetla, S.; Makofane, A.; Mathipa, M.M.; Hintsho-Mbita, N.C. Biosynthesis of iron oxide nanoparticles for the degradation of methylene blue dye, sulfisoxazole antibiotic and removal of bacteria from real water. *Heliyon* **2022**, *8*, e10536. [CrossRef]
232. Sanjeev, N.O.; Valsan, A.E. Photocatalytic and antibacterial activity of green synthesized and immobilized zinc oxide nanoparticles for the removal of sulfadiazine and acetaminophen: Effect of operational parameters and degradation pathway. *J. Environ. Chem. Eng.* **2024**, *12*, 112649. [CrossRef]
233. Xie, L.; Du, T.; Wang, J.; Ma, Y.; Ni, Y.; Liu, Z.; Zhang, L.; Yang, C.; Wang, J. Recent advances on heterojunction-based photocatalysts for the degradation of persistent organic pollutants. *Chem. Eng. J.* **2021**, *426*, 130617. [CrossRef]
234. Purkait, P.K.; Majumder, S.; Roy, S.; Maitra, S.; Das, G.C.; Chaudhuri, M.G. Enhanced heterogeneous photocatalytic degradation of florasulam in aqueous media using green synthesized TiO_2 nanoparticle under UV light irradiation. *Inorg. Chem. Commun.* **2023**, *155*, 111017. [CrossRef]
235. Purkait, P.; Bhattacharyya, A.; Roy, S.; Maitra, S.; Das, G.C.; Chaudhuri, M.G. Green synthesis of ZnO nanoparticle using *Trema orientalis* (L) leaf: An efficient photocatalyst for degradation of zoxamide fungicide in aqueous organic media under UV light irradiation. *Int. J. Environ. Anal. Chem.* **2023**, *103*, 307–325. [CrossRef]
236. Iqbal, A.; Haq, A.U.; Cerrón-Calle, G.A.; Naqvi, S.A.R.; Westerhoff, P.; Garcia-Segura, S. Green Synthesis of Flower-Shaped Copper Oxide and Nickel Oxide Nanoparticles via Capparis decidua Leaf Extract for Synergic Adsorption-Photocatalytic Degradation of Pesticides. *Catalysts* **2021**, *11*, 806. [CrossRef]
237. Rani, M.; Choudhary, S.; Shanker, U. Green synthesis of silver-doped metal hexacyanoferrates nanostructures for efficient cleanup of endocrine-disrupting pesticides. *Environ. Prog. Sustain. Energy* **2024**, *43*, e14256. [CrossRef]
238. Singh, G.; Devi, T. Studies on photocatalytic mineralization of organic pesticides by bimetallic Cu–Zn nanoparticles derived from Zingiber officinale Roscoe (ginger) using green chemistry approach. *Environ. Sci. Pollut. Res.* **2024**, *31*, 27699–27708. [CrossRef]
239. Devi, A.P.; Padhi, D.K.; Madhual, A.; Mishra, P.M.; Behera, A.K. Plant biomass driven synthesis of gAu/RGO nanocomposite towards photocatalytic degradation of phenolic compounds in wastewater. *J. Environ. Chem. Eng.* **2023**, *11*, 110161. [CrossRef]
240. Haseena, S.; Shanavas, S.; Ahamad, T.; Alshehri, S.M.; Baskaran, P.; Duraimurugan, J.; Acevedo, R.; Khan, M.A.M.; Anbarasan, P.M.; Jayamani, N. Investigation on photocatalytic activity of bio-treated α-Fe_2O_3 nanoparticles using *Phyllanthus niruri* and *Moringa stenopetala* leaf extract against methylene blue and phenol molecules: Kinetics, mechanism and stability. *J. Environ. Chem. Eng.* **2021**, *9*, 104996. [CrossRef]
241. Velázquez-Hernández, A.M.; García-Rivas, J.L.; Martínez-Gallegos, S.; González-Juárez, J.C.; Schabes-Retchkiman, P.; Albiter, V. Phytosynthesis of TiO_2 Nanoparticles Using *E. crassipes* Leaf Extracts, Their Photocatalytic Evaluation and Microbicide Effect. *Int. J. Photoenergy* **2022**, *2022*, 5177859. [CrossRef]

242. Ahmad, A.; Khawar, M.R.; Ahmad, I.; Javed, M.H.; Ahmad, A.; Rauf, A.; Younas, U.; Nazir, A.; Choi, D.; Karami, A.M. Green synthesis of ZnO nanocubes from *Ceropegia omissa* H. Huber extract for photocatalytic degradation of bisphenol An under visible light to mitigate water pollution. *Environ. Res.* **2024**, *249*, 118093. [CrossRef] [PubMed]
243. Waseem, S.; Sittar, T.; Kayani, Z.N.; Gillani, S.S.A.; Rafique, M.; Nawaz, M.A.; Shaheen, S.M.; Assiri, M.A. Plant mediated green synthesis of zinc oxide nanoparticles using *Citrus jambhiri lushi* leaves extract for photodegradation of methylene blue dye. *Phys. B Condens. Matter* **2023**, *663*, 415005. [CrossRef]
244. Ngoepe, N.M.; Mathipa, M.M.; Hintsho-Mbita, N.C. Biosynthesis of titanium dioxide nanoparticles for the photodegradation of dyes and removal of bacteria. *Optik* **2020**, *224*, 165728. [CrossRef]
245. Laouini, S.E.; Bouafia, A.; Soldatov, A.V.; Algarni, H.; Tedjani, M.L.; Ali, G.A.M.; Barhoum, A. Green Synthesized of Ag/Ag_2O Nanoparticles Using Aqueous Leaves Extracts of *Phoenix dactylifera* L. and Their Azo Dye Photodegradation. *Membranes* **2021**, *11*, 468. [CrossRef]
246. Ahmad, A.; Khan, M.; Khan, S.; Luque, R.; Abualnaja, K.M.; Alduaij, O.K.; Yousef, T.A. Bio-Construction of CuO Nanoparticles Using Texas Sage Plant Extract for catalytical degradation of Methylene blue Via Photocatalysis. *J. Mol. Struct.* **2022**, *1256*, 132522. [CrossRef]
247. Kumar, S.A.; Jarvin, M.; Inbanathan, S.S.R.; Umar, A.; Lalla, N.P.; Dzade, N.Y.; Algadi, H.; Rahman, Q.I.; Baskoutas, S. Facile green synthesis of magnesium oxide nanoparticles using tea (*Camellia sinensis*) extract for efficient photocatalytic degradation of methylene blue dye. *Environ. Technol. Innov.* **2022**, *28*, 102746. [CrossRef]
248. Weldegebrieal, G.K.; Sibhatu, A.K. Photocatalytic activity of biosynthesized α-Fe_2O_3 nanoparticles for the degradation of methylene blue and methyl orange dyes. *Optik* **2021**, *241*, 167226. [CrossRef]
249. Quevedo-Robles, R.V.; Vilchis-Nestor, A.R.; Luque, P.A. Study of optical and morphological properties of nanoparticles semiconductors of zinc oxide synthesized using *Mimosa tenuiflora* extract for photodegradation of methyl orange. *Opt. Mater.* **2022**, *128*, 112450. [CrossRef]
250. Karimi, F.; Rezaei-savadkouhi, N.; Uçar, M.; Aygun, A.; Tiri, R.N.E.; Meydan, I.; Aghapour, E.; Seckin, H.; Berikten, D.; Gur, T.; et al. Efficient green photocatalyst of silver-based palladium nanoparticles for methyle orange photodegradation, investigation of lipid peroxidation inhibition, antimicrobial, and antioxidant activity. *Food Chem. Toxicol.* **2022**, *169*, 113406. [CrossRef]
251. Barzinjy, A.A.; Hamad, S.M.; Aydın, S.; Ahmed, M.H.; Hussain, F.H.S. Green and eco-friendly synthesis of Nickel oxide nanoparticles and its photocatalytic activity for methyl orange degradation. *J. Mater. Sci. Mater. Electron.* **2020**, *31*, 11303–11316. [CrossRef]
252. Nguyen-Hong, Y.; Luu, T.V.H.; Doan, V. Green synthesis of Ce-doped ZnO nanoparticles using *Hedyotis capitellata* Leaf extract for efficient photocatalytic degradation of Methyl Orange. *Vietnam J. Chem.* **2021**, *59*, 648–659. [CrossRef]
253. Shaikh, W.A.; Chakraborty, S.; Islam, R.U. Photocatalytic degradation of rhodamine B under UV irradiation using *Shorea robusta* leaf extract-mediated bio-synthesized silver nanoparticles. *Int. J. Environ. Sci. Technol.* **2020**, *17*, 2059–2072. [CrossRef]
254. Luque, P.A.; Garrafa-Gálvez, H.E.; García-Maro, C.A.; Soto-Robles, C.A. Study of the optical properties of ZnO semiconductor nanoparticles using *Origanum vulgare* and its effect in Rhodamine B degradation. *Optik* **2022**, *258*, 168937. [CrossRef]
255. Rajendran, A.; Alsawalha, M.; Alomayri, T. Biogenic synthesis of husked rice-shaped iron oxide nanoparticles using coconut pulp (*Cocos nucifera* L.) extract for photocatalytic degradation of Rhodamine B dye and their in vitro antibacterial and anticancer activity. *J. Saudi Chem. Soc.* **2021**, *25*, 101307. [CrossRef]
256. Luque, P.A.; Garrafa-Gálvez, H.E.; Nava, O.; Olivas, A.; Martínez-Rosas, M.E.; Vilchis-Nestor, A.R.; Villegas-Fuentes, A.; Chinchillas-Chinchillas, M.J. Efficient sunlight and UV photocatalytic degradation of Methyl Orange, Methylene Blue and Rhodamine B, using Citrus×paradisi synthesized SnO_2 semiconductor nanoparticles. *Ceram. Int.* **2021**, *47*, 23861–23874. [CrossRef]
257. Rafique, M.; Shafiq, F.; Gillani, S.S.A.; Shakil, M.; Tahir, M.B.; Sadaf, I. Eco-friendly green and biosynthesis of copper oxide nanoparticles using *Citrofortunella microcarpa* leaves extract for efficient photocatalytic degradation of Rhodamin B dye form textile wastewater. *Optik* **2020**, *208*, 164053. [CrossRef]
258. Khan, Z.U.H.; Khan, A.; Shah, N.S.; Din, I.U.; Salam, M.A.; Iqbal, J.; Muhammad, N.; Imran, M.; Ali, M.; Sayed, M.; et al. Photocatalytic and biomedical investigation of green synthesized NiONPs: Toxicities and degradation pathways of Congo red dye. *Surf. Interfaces* **2021**, *23*, 100944. [CrossRef]
259. Brishti, R.S.; Habib, M.A.; Ara, M.H.; Karim, K.M.R.; Islam, M.K.; Naime, J.; Rumon, M.M.H.; Khan, M.A.R. Green synthesis of ZnO NPs using aqueous extract of *Epipremnum aureum* leave: Photocatalytic degradation of Congo red. *Results Chem.* **2024**, *7*, 101441. [CrossRef]
260. Benisha, R.; Amalanathan, M.; Aravind, M.; Mary, M.S.M.; Ahmad, A.; Tabassum, S.; Al-Qahtani, W.H.; Ahmad, I. *Catharanthus roseus* leaf extract mediated Ag-MgO nanocatalyst for photocatalytic degradation of Congo red dye and their antibacterial activity. *J. Mol. Struct.* **2022**, *1262*, 133005. [CrossRef]

261. Indira, K.; Shanmugam, S.; Hari, A.; Vasantharaj, S.; Sathiyavimal, S.; Brindhadevi, K.; El Askary, A.; Elfasakhany, A.; Pugazhendhi, A. Photocatalytic degradation of congo red dye using nickel–titanium dioxide nanoflakes synthesized by *Mukia madrasapatna* leaf extract. *Environ. Res.* **2021**, *202*, 111647. [CrossRef]
262. Bopape, D.A.; Tetana, Z.N.; Mabuba, N.; Motaung, D.E.; Hintsho-Mbita, N.C. Biosynthesis of TiO_2 nanoparticles using *Commelina benghanlensis* for the photodegradation of methylene blue dye and antibiotics: Effect of plant concentration. *Results Chem.* **2023**, *5*, 100825. [CrossRef]
263. Bopape, D.A.; Motaung, D.E.; Hintsho-Mbita, N.C. Green synthesis of ZnO: Effect of plant concentration on the morphology, optical properties and photodegradation of dyes and antibiotics in wastewater. *Optik* **2022**, *251*, 168459. [CrossRef]
264. Munyai, S.; Tetana, Z.N.; Mathipa, M.M.; Ntsendwana, B.; Hintsho-Mbita, N.C. Green synthesis of Cadmium Sulphide nanoparticles for the photodegradation of Malachite green dye, Sulfisoxazole and removal of bacteria. *Optik* **2021**, *247*, 167851. [CrossRef]
265. Makofane, A.; Maake, P.J.; Mathipa, M.M.; Matinise, N.; Cummings, F.R.; Motaung, D.E.; Hintsho-Mbita, N.C. Green synthesis of $NiFe_2O_4$ nanoparticles for the degradation of Methylene Blue, sulfisoxazole and bacterial strains. *Inorg. Chem. Commun.* **2022**, *139*, 109348. [CrossRef]
266. Pakzad, K.; Alinezhad, H.; Nasrollahzadeh, M. *Euphorbia polygonifolia* extract assisted biosynthesis of Fe_3O_4@CuO nanoparticles: Applications in the removal of metronidazole, ciprofloxacin and cephalexin antibiotics from aqueous solutions under UV irradiation. *Appl. Organomet. Chem.* **2020**, *34*, e5910. [CrossRef]
267. Iqbal, Y.; Ahmed, S.; Aziz, M.H.; Alam, M.; Asif, M.; Huang, Q. Greener approach for the synthesis of Ag decorated ZnO–CeO_2 nanostructure using *Moringa oleifera* LE and its investigation as photocatalyst for degradation of ciprofloxacin and methylene orange. *Mater. Chem. Phys.* **2024**, *318*, 129299. [CrossRef]
268. Taj, M.B.; Alkahtani, M.D.F.; Raheel, A.; Shabbir, S.; Fatima, R.; Aroob, S.; Yahya, R.; Alelwani, W.; Alahmadi, N.; Abualnaja, M.; et al. Bioconjugate synthesis, phytochemical analysis, and optical activity of $NiFe_2O_4$ nanoparticles for the removal of ciprofloxacin and Congo red from water. *Sci. Rep.* **2021**, *11*, 5439. [CrossRef]
269. Gaim, Y.T.; Yimanuh, S.M.; Kidanu, Z.G. Enhanced Photocatalytic Degradation of Amoxicillin with Mn-Doped Cu_2O under Sunlight Irradiation. *J. Compos. Sci.* **2022**, *6*, 317. [CrossRef]
270. Chankhanittha, T.; Yenjai, C.; Nanan, S. Utilization of formononetin and pinocembrin from stem extract of *Dalbergia parviflora* as capping agents for preparation of ZnO photocatalysts for degradation of RR141 azo dye and ofloxacin antibiotic. *Catal. Today* **2022**, *384*, 279–293. [CrossRef]
271. Mahlaule-Glory, L.M.; Mathobela, S.; Hintsho-Mbita, N.C. Biosynthesized Bimetallic ($ZnOSnO_2$) Nanoparticles for Photocatalytic Degradation of Organic Dyes and Pharmaceutical Pollutants. *Catalysts* **2022**, *12*, 334. [CrossRef]
272. Thangsan, P.; Wannakan, K.; Nanan, S. Biosynthesis of ZnO using *Senna siamea* leaf extract for photodegradation of tetracycline antibiotic and azo dye in wastewater. *OpenNano* **2024**, *16*, 100202. [CrossRef]
273. Fatimah, I.; Yanti, I.; Putri, F.H.A.; Herianto, D.; Sagadevan, S.; Tamyiz, M.; Doong, R. Phyto-mediated hydrothermal synthesis of $NiFe_2O_4$ as photocatalyst in tetracycline photodegradation. *Environ. Nanotechnol. Monit. Manag.* **2023**, *20*, 100879. [CrossRef]
274. Malakootian, M.; Asadzadeh, S.N.; Mehdipoor, M.; Kalantar-Neyestanaki, D.; Firouzeh, N. *Stevia rebaudiana* leaf extract mediated green synthesis of cerium oxide nanoparticles for antibacterial activity and photocatalytic degradation of tetracycline. *Desalination Water Treat.* **2024**, *317*, 100126. [CrossRef]
275. Nguyen, T.H.A.; Le, V.T.; Doan, V.-D.; Tran, A.V.; Nguyen, V.C.; Nguyen, A.-T.; Vasseghian, Y. Green synthesis of Nb-doped ZnO nanocomposite for photocatalytic degradation of tetracycline antibiotic under visible light. *Mater. Lett.* **2022**, *308*, 131129. [CrossRef]
276. Fatimah, I.; Citradewi, P.W.; Purwiandono, G.; Hidayat, H.; Sagadevan, S. Nickel oxide decorated reduced graphene oxide synthesized using single bioreductor of *Pometia pinnata* leaves extract as photocatalyst in tetracycline photooxidation and antibacterial agent. *Inorg. Chem. Commun.* **2023**, *148*, 110287. [CrossRef]
277. Rani, M.; Yadav, J.; Keshu; Shanker, U. Green synthesis of sunlight responsive zinc oxide coupled cadmium sulfide nanostructures for efficient photodegradation of pesticides. *J. Colloid Interface Sci.* **2021**, *601*, 689–703. [CrossRef]
278. Rocha, V.; Franco, S.; Bertão, A.R.; Neves, I.C.; Tavares, T. Recycling of natural and waste materials as supports for green silver nanoparticles as efficient catalysts in photodegradation of organic pollutants. *Environ. Technol. Innov.* **2024**, *34*, 103576. [CrossRef]
279. Choudhary, S.; Rani, M.; Keshu; Shanker, U. Green biosynthesized N-doped Bi_2O_3@SnO_2 nanocomposite for efficient remediation of endocrine disrupting pesticides. *Environ. Nanotechnol. Monit. Manag.* **2022**, *18*, 100746. [CrossRef]
280. Kamarudin, N.S.; Jusoh, R.; Jalil, A.A.; Setiabudi, H.D.; Sukor, N.F. Synthesis of silver nanoparticles in green binary solvent for degradation of 2,4-D herbicide: Optimization and kinetic studies. *Chem. Eng. Res. Des.* **2020**, *159*, 300–314. [CrossRef]
281. Vinayagam, R.; Sharma, G.; Murugesan, G.; Pai, S.; Gupta, D.; Narasimhan, M.K.; Kaviyarasu, K.; Varadavenkatesan, T.; Selvaraj, R. Rapid photocatalytic degradation of 2, 4-dichlorophenoxy acetic acid by ZnO nanoparticles synthesized using the leaf extract of *Muntingia calabura*. *J. Mol. Struct.* **2022**, *1263*, 133127. [CrossRef]
282. Punyasamudram, S.; Puthalapattu, R.P.; Bathinapatla, A.; Kanchi, S.; Jyothi, S.; Kumar, P.V.N. Biosynthesis of $ZnFe_2O_4$@Ag hybrid nanocomposites for degradation of 2,4-Dichlorophenoxyacetic acid herbicide. *Chem. Phys. Impact* **2023**, *7*, 100282. [CrossRef]

283. Chawla, H.; Garg, S.; Rohilla, J.; Szamosvölgyi, Á.; Efremova, A.; Szenti, I.; Ingole, P.P.; Sápi, A.; Kónya, Z.; Chandra, A. Visible LED-light driven photocatalytic degradation of organochlorine pesticides (2,4-D & 2,4-DP) by Curcuma longa mediated bismuth vanadate. *J. Clean. Prod.* **2022**, *367*, 132923. [CrossRef]
284. Attri, P.; Garg, S.; Ratan, J.K.; Giri, A.S. Silver nanoparticles from *Tabernaemontana divaricate* leaf extract: Mechanism of action and bio-application for photo degradation of 4-aminopyridine. *Environ. Sci. Pollut. Res.* **2022**, *30*, 24856–24875. [CrossRef] [PubMed]
285. Abdallah, S.S.; Maridevaru, M.C.; Marzouqi, F.A.; Selvaraj, R. Green synthesis of TiO_2@g-C_3N_4 nanocomposites for the photocatalytic degradation of pesticides and toxic organics present in water and wastewater. *J. Photochem. Photobiol. Chem.* **2025**, *459*, 116015. [CrossRef]
286. Maijan, P.; Waen-ngoen, T.; Suwanboon, S.; Chantarak, S.; Voravuthikunchai, S.P. Sustainable environmental-based synthesis of zinc oxide nanoparticles using para rubber leaf extract for photocatalytic degradation of organic pollutants and microbial control in wastewater treatment. *Inorg. Chem. Commun.* **2024**, *162*, 112086. [CrossRef]
287. Pathania, D.; Sharma, A.; Kumar, S.; Srivastava, A.K.; Kumar, A.; Singh, L. Bio-synthesized Cu–ZnO hetro-nanostructure for catalytic degradation of organophosphate chlorpyrifos under solar illumination. *Chemosphere* **2021**, *277*, 130315. [CrossRef]
288. Mandvi; Singh, P.P.; Ballal, S.; Chahar, M.; Bansal, J.; Kumar, R.; Kumar, S.; Kaushal, S. Construction of a 3D flower-like NiO/Mn_3O_4 heterojunction using Tulsi leaf extract for enhanced photodegradation of thiamethoxam pesticide and organic dyes under direct sunlight. *Mater. Adv.* **2024**, *5*, 8097–8110. [CrossRef]
289. Ahmad, T.; Iqbal, J.; Bustam, M.A.; Zulfiqar, M.; Muhammad, N.; Al Hajeri, B.M.; Irfan, M.; Asghar, H.M.A.; Ullah, S. Phytosynthesis of cerium oxide nanoparticles and investigation of their photocatalytic potential for degradation of phenol under visible light. *J. Mol. Struct.* **2020**, *1217*, 128292. [CrossRef]
290. Ahmad, W.; Ahmed, S.; Shameem, M.; Kumar, S.; Ansari, S.A. Nanophotocatalytic degradation of phenolic contaminants by ZnS nanoparticles synthesized from banana peel extract: A greener approach. *Environ. Monit. Assess.* **2025**, *197*, 401. [CrossRef]
291. Rajabi, H.R.; Sajadiasl, F.; Karimi, H.; Alvand, Z.M. Green synthesis of zinc sulfide nanophotocatalysts using aqueous extract of Ficus Johannis plant for efficient photodegradation of some pollutants. *J. Mater. Res. Technol.* **2020**, *9*, 15638–15647. [CrossRef]
292. Rani, M.; Keshu; Shanker, U. Sunlight-induced photocatalytic degradation of organic pollutants by biosynthesized hetrometallic oxides nanoparticles. *Environ. Sci. Pollut. Res.* **2021**, *28*, 61760–61780. [CrossRef]
293. Hidayat, R.; Fadillah, G.; Ohira, S.-I.; Fajarwati, F.I.; Setyorini, D.A.; Saputra, A. Facile green synthesis of Ag doped TiO_2 nanoparticles using maple leaf for bisphenol-A degradation and its antibacterial properties. *Mater. Today Sustain.* **2024**, *26*, 100752. [CrossRef]
294. Zhang, X.; Saravanakumar, K.; Sathiyaseelan, A.; Wang, M.-H. Biosynthesis, characterization, antibacterial activities of manganese nanoparticles using *Arcopilus globulus* and their efficiency in degradation of bisphenol A. *Inorg. Chem. Commun.* **2022**, *141*, 109521. [CrossRef]
295. Rani, M.; Meenu; Shanker, U. Highly efficient photocatalytic degradation of endocrine disruptor phenols by green synthesized Z-scheme type CuS doped Bi_2O_3 nanocomposite: Optimization factors, kinetics, and mechanism insights. *J. Water Process Eng.* **2025**, *69*, 106900. [CrossRef]
296. AlGarni, T.S.; Ali, M.H.H.; Al-Mohaimeed, A.M. Green biosynthesis of Fe_3O_4 nanoparticles using *Chlorella vulgaris* extract for enhancing degradation of 2,4 dinitrophenol. *J. King Saud Univ. Sci.* **2023**, *35*, 102426. [CrossRef]

Disclaimer/Publisher's Note: The statements, opinions and data contained in all publications are solely those of the individual author(s) and contributor(s) and not of MDPI and/or the editor(s). MDPI and/or the editor(s) disclaim responsibility for any injury to people or property resulting from any ideas, methods, instructions or products referred to in the content.